XUV spectroscopy of highly excited states in H2, HD en D2

Ivanov, T.I.

2010

XUV spectroscopy of highly excited states in H_2, HD and D_2

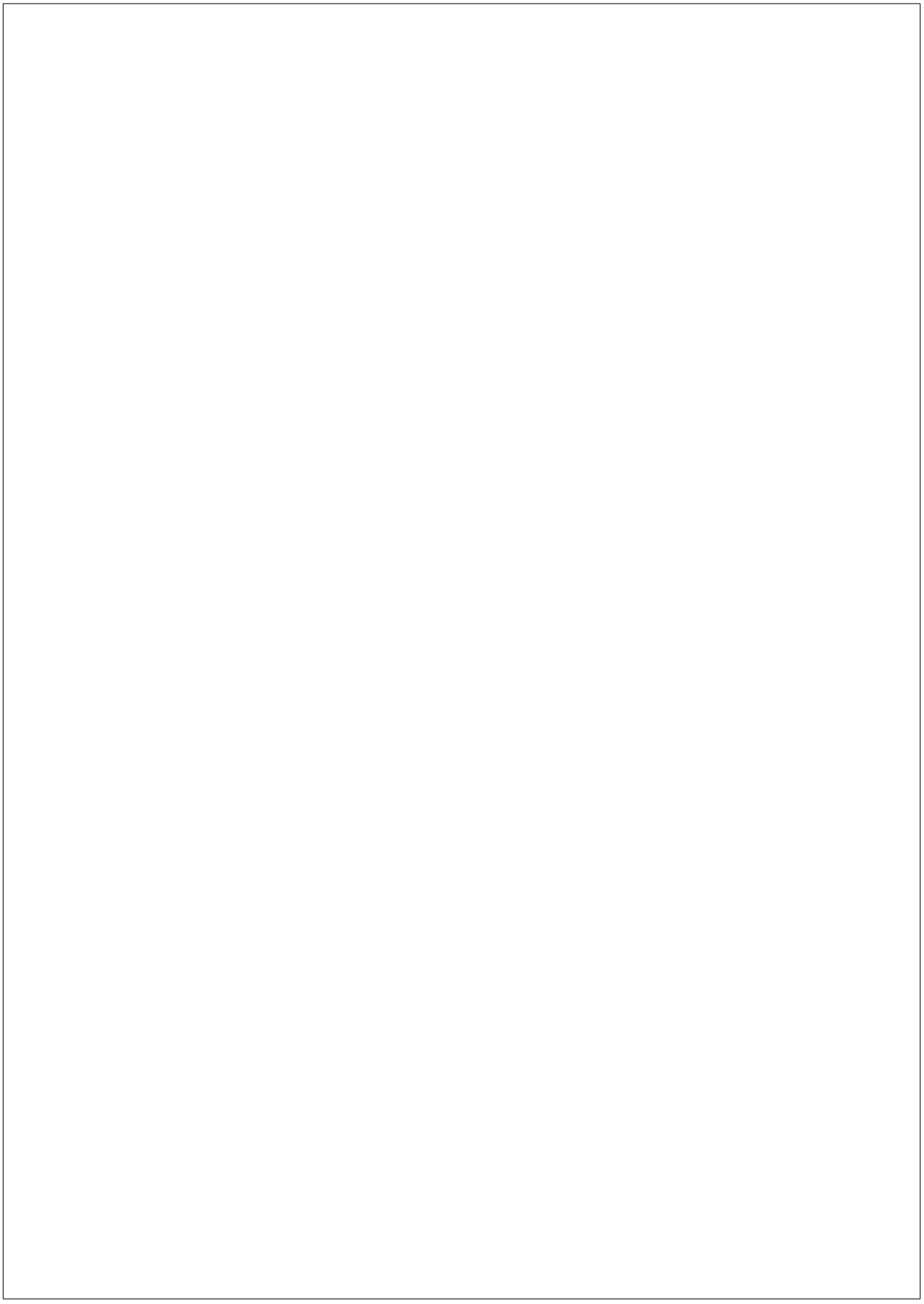

VRIJE UNIVERSITEIT

XUV spectroscopy of highly excited states in H_2, HD and D_2

ACADEMISCH PROEFSCHRIFT

ter verkrijging van de graad Doctor aan
de Vrije Universiteit Amsterdam,
op gezag van de rector magnificus
prof.dr. L.M. Bouter,
in het openbaar te verdedigen
ten overstaan van de promotiecommissie
van de faculteit der Exacte Wetenschappen
op dinsdag 7 december 2010 om 15.45 uur
in de aula van de universiteit,
De Boelelaan 1105

door

Toncho Ivanov Ivanov
geboren te Kazanlak, Bulgarije

promotoren: prof.dr. W.M.G. Ubachs
prof.dr. C.A. de Lange

leescommissie:

prof.dr. M.H.M. Janssen, VU University, Amsterdam

prof.dr. C. Jungen, Laboratoire Aimé Cotton, Orsay, France

dr. L. Nahon, SOLEIL Synchrotron, St. Aubin, France

prof.dr. D.H. Parker, Radboud University, Nijmegen

dr. L. Willmann, University of Groningen, Groningen

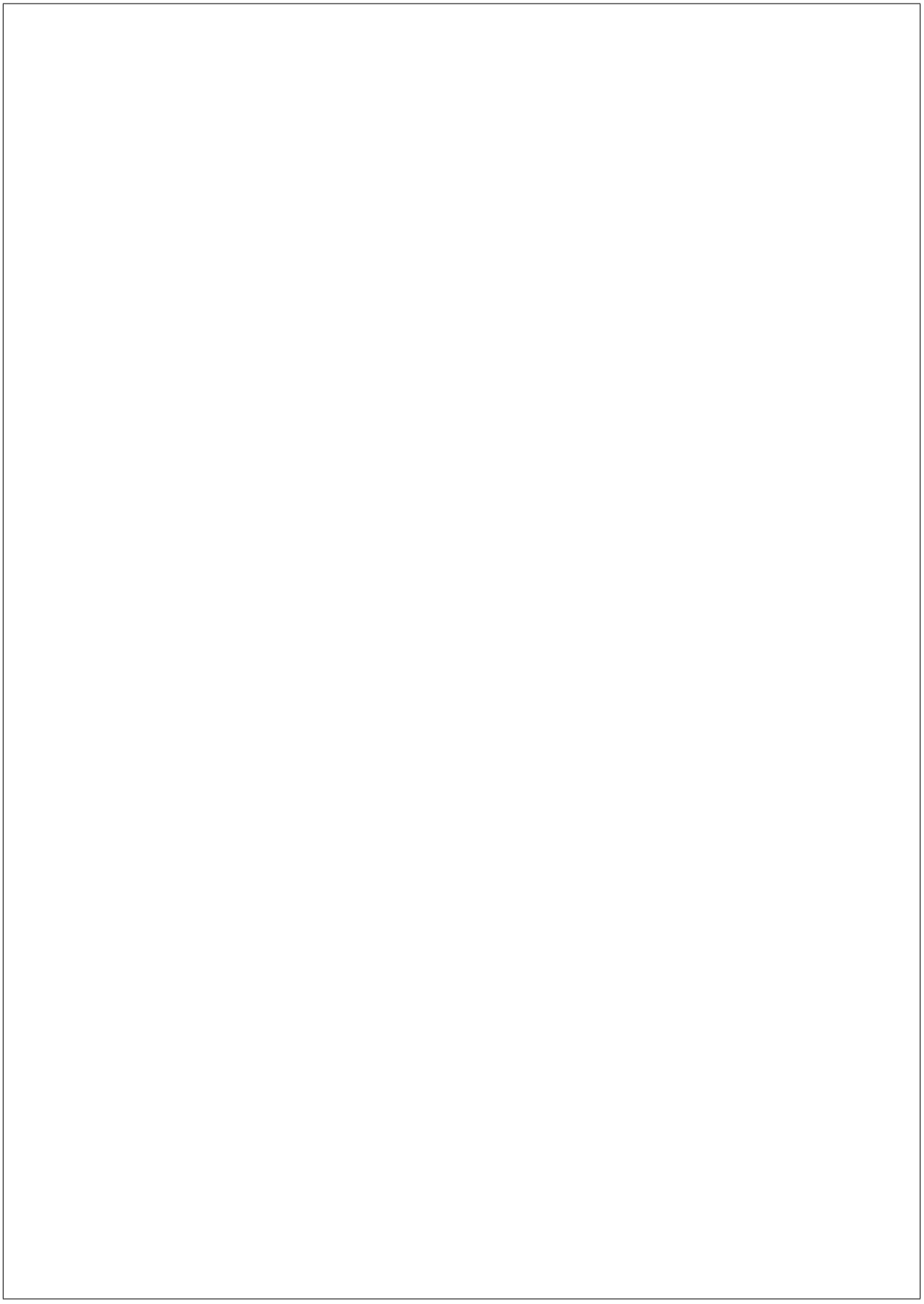

Contents

Chapter 1

Introduction and Summary

The discovery of hydrogen as an element, and as a molecular species consisting of two atoms, is connected to the names of the scientific pioneers Cavendish, Lavoisier, Gay-Lussac and Avogadro. In the 19-th century hydrogen was studied with spectroscopes. Besides the lines of atomic hydrogen in the visible range, that later became known as Balmer lines, already at an early stage some additional lines were observed. These were referred to as a "second spectrum" of hydrogen. The first spectroscopic observations to be unambiguously assigned to molecular hydrogen were made by Lyman [1], now over a century ago. This discovery could only be made through the development of vacuum-ultraviolet spectroscopic techniques. In our studies on the spectrum of the hydrogen molecule we still rely on such techniques. We use the narrowband and tunable Amsterdam eXtreme Ultra-Violet (XUV) laser system in a variety of spectroscopic studies. The setup can be used in high-resolution scanning spectroscopic studies, but its pulsed nature can also be employed in double-resonance studies of the hydrogen molecule and its isotopologues. Through the use of multiple overlapping laser pulses the excited-state level structure of the molecule can be probed, even for quantum states that are inaccessible from the ground state (for various reasons: unfavourable dipole selection rules, poor wave function overlap). The combination of lasers with time-of-flight mass separation and velocity-map-imaging techniques, the implementation of which is also discussed in this thesis, allows for further detailed studies, in particular on the dissociation dynamics of some highly excited states of the molecule. In addition to lasers we have also employed a novel and unique instrument: the vacuum ultraviolet Fourier-Transform spectrometer at the Soleil synchrotron facility.

Our studies are motivated by various perspectives, ranging from astrophysics, via molecular physics to fundamental physics. Molecular hydrogen is by far the most abundant molecule in the Universe. However, H_2 remained unobserved in the interstellar medium for a long time, for the very reason that its dipole-allowed absorption spectrum lies in the vacuum ultraviolet and is

therefore blocked by the Earth's atmosphere. It took a rocket-borne ultraviolet spectrometer for its detection. The observation of molecular hydrogen in faint high-redshifted objects from ground-based telescopes gave impetus to the field and promoted the idea of studying the spectrum of H_2 at the highest resolution possible to search for a variation in the fundamental dimensionless constant of nature μ (the proton-electron mass ratio) on a cosmological time scale [2]. Spectra of HD are also included in such an analysis [3].

Apart from this motivation from astrophysics and fundamental physics, the study of the quantum structure of the smallest neutral molecular entity remains of importance for its own sake. Despite a century of spectroscopic studies still many aspects of the H_2 level structure are not understood. This can be exemplified by the fact that the majority of the spectral lines contained in the *Dieke Atlas* [4] still remain unassigned. In addition, the manifold of dissociative resonances, in particular those of singlet *gerade* symmetry, is a still uncharted area; our study of dissociative resonances just above the n=2 dissociation limit is an attempt to improve this situation.

Even when a subject has been investigated for over a century, surprises are still possible. Our finding and identification of frequency-resolved Rydberg series in the heavy H^+H^- Rydberg system constitutes one of these surprises. In our view the observation of heavy Rydberg series in H^+H^- may open up a novel field of research, since such quantum states should exist in any molecular system.

Outline

This thesis describes an experimental investigation of molecular hydrogen and its isotopologues. It can be subdivided thematically into three parts: the first dealing with high-resolution spectroscopy, the second with ion-pair or heavy Rydberg states, and the third on velocity-map-imaging and dissociation of the molecule. Here we give an overview of the following Chapters contained in this thesis.

In Chapter 2 Hydrogen Deuteride (HD) has been proposed as a test system in a search for a possible variation in the proton-to-electron mass ratio. Spectroscopic features of the second most abundant hydrogen isotopologue have already been observed in several quasar spectra at high redshift [3]. At the moment detection of HD has been reported along the line-of-sight of the following quasar systems: Q1232+082, Q0528-250, FJ0812+320, J2123-050, J1237+064 and Q1439+113. A high resolution laboratory determination of the most prominent HD lines is performed at a relative accuracy of 5×10^{-8} with the aid of the narrowband and tunable XUV-laser system. Also, sensitivity coefficients are determined from *ab initio* quantum chemical calculations as a function of the proton-electron mass ratio. These results are of sufficient quality to include them in a full statistical analysis together with the extensive data on H_2. An important characteristic of HD is the presence of a neutron in the

nucleus. Strategies to deduce possible effects beyond first order baryon/lepton mass-ratio deviations are discussed.

Chapter 3 extends the HD database started in Chapter 2. A novel wavefront-division Fourier-Transform spectrometer, which is a permanent end station of the undulator-based beamline DESIRS on the synchrotron SOLEIL facility, is employed for the first time for the spectroscopy of HD in the XUV energetic region. The HD spectral lines in the Lyman and Werner bands were recorded in the 87-112 nm range from a quasi-static gas sample in a windowless configuration and with Doppler-limited resolution. Line positions of some 268 transitions in the $B^1\Sigma_u^+ (v' = 0 - 30) \leftarrow X^1\Sigma_g^+ (v'' = 0)$ Lyman bands and 141 transitions in the $C^1\Pi_u(v' = 0 - 10) \leftarrow X^1\Sigma_g^+(v'' = 0)$ Werner bands were deduced with uncertainties of 0.04 cm^{-1} (1σ), which corresponds to $\Delta\lambda/\lambda \sim 4 \times 10^{-7}$. The results from the previous chapter were used to test and improve the internal calibration of this unique setup.

In Chapter 4 a missing gap in the H_2 database is filled. Due to problems encountered previously in generating the appropriate wavelengths using a narrow-band extreme ultraviolet laser source, the $B^1\Sigma_u^+ - X^1\Sigma_g^+$ (6,0) Lyman band of H_2 was still missing in the set of laboratory data. These transitions were accessed by using an exotic dye mixture, which expanded the tuning range of the XUV system covering the problematic 615-620 nm range. This system was used also for calibrating $(^4S^o)$ 3d $^3D_J^o \leftarrow ^3P_J$ transitions in atomic oxygen [5].

Chapter 5 describes the calibration of 39 lines in the $B^1\Sigma_u^+$ - $X^1\Sigma_g^+(v', 0)$ Lyman bands for $v' = 9-11$, and in the $C^1\Pi_u$ - $X^1\Sigma_g^+(0, 0)$ Werner band of the D_2 molecule. Using a narrowband tunable extreme-ultraviolet laser source they were measured at a relative accuracy of $\Delta\lambda/\lambda = 6 \times 10^{-8}$. The results bear relevance for future use in the calibration of dense classical spectra obtained for the HD and D_2 isotopologues.

Chapter 6 describes the first observation of Rydberg states in the exotic H^+H^- system. This system is very interesting as at large internuclear distance it can be considered as two point-like charged particles bound by a Coulomb potential. This description is formally equivalent to the well-known Bohr atom, and therefore should possess the same characteristic energetic structure appropriately scaled by the reduced mass of the system. Unfortunately, Frank-Condon restrictions prevent accessing these states directly. Nevertheless, spectroscopic features predicted by the Rydberg formula for this "heavy Rydberg atom" are indeed observed. This remarkable result is achieved thanks to a complex interaction of broad molecular Rydberg states at small internuclear distance with the "heavy" Rydberg states at larger internuclear distance, which results in the population of H^+H^- levels. One of the possible decay channels of these ion pair states involves autoionization and creation of H_2^+ ions, which we detect as a series of broad resonances matching the heavy Rydberg formula.

Chapter 7 reports on the development of a velocity map imaging (VMI)

detection setup implemented in the existing extreme-ultraviolet (XUV) laser system at the Laser Center VU Amsterdam. Although still in the process of development, its performance and some preliminary results are discussed. Best focusing conditions obtained so far show a spatial resolution of 400 μm, indicating that the system has not yet reached its optimal performance. This is due to some inherent limitations in the present setup. The technique for producing XUV light by non-linear frequency upconversion in a gas jet creates divergent XUV radiation, which determines a relatively large interaction region. This is a crucial element in VMI performance. Other limitations are described in detail and future improvements are proposed. An XUV laser system that combines narrowband state-selective excitation with VMI detection of the ionized fragments would open up great possibilities for studying the dissociation dynamics of small molecules with spectroscopic features in the XUV domain.

In Chapter 8 the *gerade* electronic structure of molecular hydrogen above its n=2 dissociation limit is studied by 1 XUV + 1 VIS two-step laser excitation. Spectral features exhibiting widths between one and several hundred cm^{-1} in the excitation range of 118500-120500 cm^{-1} were probed by laser-ionization of the H(n=2) products produced in the dissociation process. The controlled two-step process combined with mass-selective detection imposes constraints on the possible allowed quantum states to be reached. Through the application of angular momentum selection rules and using the ortho-para distinction the predissociation resonances of *gerade* inversion symmetry of H_2 could be identified in terms of electronic symmetry and ro-vibrational quantum numbers. In this way most of the broad dissociative resonances in the energy region can be assigned.

Chapter 2

HD as a probe for detecting mass variation on a cosmological time scale

Abstract

The strong electronic absorption systems of the $B^1\Sigma_u^+ - X^1\Sigma_g^+$ Lyman and the $C^1\Pi_u - X^1\Sigma_g^+$ Werner bands can be used to probe possible mass-variation effects on a cosmological time scale from spectra observed at high redshift, not only in H_2, but also in the second most abundant hydrogen isotopologue HD. High resolution laboratory determination of the most prominent HD lines at extreme ultraviolet wavelengths is performed at an accuracy of $\Delta\lambda/\lambda \sim 5 \times 10^{-8}$, forming a database for comparison with astrophysical data. Sensitivity coefficients $K_i = d\ln\lambda_i/d\ln\mu$ are determined for HD from quantum *ab initio* calculations as a function of the proton-electron mass ratio μ. Strategies to deduce possible effects beyond first-order baryon/lepton mass ratio deviations are discussed.

The observation of spectral features at high redshift ($z \sim 2-3$) provides an opportunity to probe minute variations of some fundamental constants over time intervals of 10^{10} years, corresponding to 80% of the lifetime of the Universe. For the fine structure constant α evidence has been reported for a temporal drift at 5σ significance [6]. Variation of another fundamental constant, the dimensionless proton-electron mass ratio $\mu = m_p/m_e$, may be probed through spectra of molecules. Recently, an indication for a possible decrease of μ was reported at $\Delta\mu/\mu = (2.45 \pm 0.59) \times 10^{-5}$ over a time interval of 12×10^9 years [7,8]. This result is derived from a set of 76 H_2 spectral lines in two absorption systems at $z = 2.59$ and $z = 3.02$ in the line of sight towards quasars $Q0405-443$ and $Q0347-383$ [9]. From observations of the NH_3 inversion splitting in the astrophysical object $B0218+357$ at $z = 0.68$, a tight constraint upon μ variation at $\Delta\mu/\mu = (0.6 \pm 1.9) \times 10^{-6}$ was deduced [10]. These seemingly contradictory results might be reconciled by invoking the concept of a

phase transition having occurred at $z \sim 1$, transiting from a matter-dominated to a dark-energy-dominated Universe; variation of constants is hypothesized to occur only before the phase transition, hence for $z > 1$ [11,12].

The comparison of spectral lines over cosmological time scales depends on the availability of spectral transitions that can be observed at high accuracy and at high redshift. Molecular hydrogen is the most abundant molecule in the Universe by orders of magnitude. The abundance of the deuterated HD species competes with other abundant molecules such as CO and CH and HCO^+, such that it is worthwhile to consider the opportunity of using HD absorption for probing mass-variation effects. HD lines in the Lyman bands have indeed been observed in the object $Q1232+082$ at $z = 2.34$ [3].

To facilitate this opportunity, a set of highly accurate zero-redshift (laboratory) transition wavelengths of HD electronic absorption lines is required. Here we report on the spectral calibration of zero-redshift HD lines in the $B^1\Sigma_u^+ - X^1\Sigma_g^+$ Lyman and the $C^1\Pi_u - X^1\Sigma_g^+$ Werner bands, referred to as Lv and Wv bands with v the vibrational quantum number, in the extreme ultraviolet range 100-110 nm at an accuracy of $\Delta\lambda/\lambda \sim 5 \times 10^{-8}$. At present-day large telescopes high-redshift spectra can be obtained at accuracies in the range $(0.2 - 1.0) \times 10^{-6}$ [9]; hence, these new HD laboratory results, which constitute a two-orders-of-magnitude improvement over existing data [13], will then contribute only slightly in a comparison with astrophysical data. A second ingredient required for a comparison between laboratory and high-redshift data is a theory that relates possible changes in μ to observable shifts in spectra. For H_2, sensitivity coefficients K_i were previously deduced both in a semiempirical fashion [8] and through quantum-chemical calculations [14]. Here we report on such *ab initio* calculations for K_i coefficients of HD spectral lines.

Laboratory measurements were performed to determine the zero-redshift wavelengths of the most prominent HD spectral absorption lines in the Lyman and Werner bands. The methods employed here for the HD molecule are similar to those described previously for the H_2 spectroscopic studies [15]. A narrow band extreme ultraviolet laser beam, wavelength tunable in the range 100-110 nm, perpendicularly intersects a collimated molecular hydrogen beam (enriched for 90% in HD). Upon resonant excitation a UV beam further ionizes the excited molecules to form HD^+ ions that are detected. The bandwidth of the laser system is better than 250 MHz, corresponding to $\Delta\lambda < 10^{-5}$ nm. The Doppler contribution to the linewidth is small in the perpendicular geometry, while it is further reduced (compared to previous measurements [15]) by selecting the lowest velocity components in the molecular beam. At observed linewidths of ~ 450 MHz the natural line broadening corresponding to an upper state lifetime of 0.5 ns is approached. A typical recording is shown in Fig. 2.1. The absolute calibration of the HD resonances relies on saturation spectroscopy in I_2 of the visible laser radiation that is pulse amplified and subsequently harmonically converted to extreme ultraviolet for the spectroscopy. The uncertainty budget

for the determination of the resonance wavelengths is similar to that in the H_2 studies, resulting in a relative uncertainty of $\Delta\lambda/\lambda = 5 \times 10^{-8}$ or in absolute terms $\Delta\lambda = 0.000\,005$ nm. The obtained HD line positions are collected in Table 2.1, where a listing is given in units of wavelength (nm), for the purpose of comparison with astrophysical data. Values represent *vacuum* wavelengths. Values presented for the Lyman bands L0, L1 and L2 are taken from Ref. [16], while L16 values are from Ref. [17], after a correction for misassignment. The present data set in the range 100-110 nm will not cover the entire range of astrophysical observations of HD, which may well extend to 93 nm. For the moment the laser calibration data of Hinnen *et al.* [18], at an accuracy of 5×10^{-7}, can be included in comparisons with quasar data until more accurate data become available.

Combination differences between $P(J''+2)$ and $R(J'')$ lines can be compared with ground state splittings from far-infrared spectroscopy [19]; the average difference of -0.0004 cm^{-1} is well below the accuracy claimed in Table 2.1. When comparing the present values with the classical data of Dabrowski and Herzberg [13], we find that these are on average higher by 0.29 cm^{-1} with respect to our values. The lines that present the larger discrepancies are marked as "blended" in Ref. [13].

Level energies in the HD molecule were calculated, applying the same method as previously applied for the D_2 molecule [20], using highly accurate *ab initio* data [21–23]. The four nearby-lying excited electronic states of *ungerade* symmetry, $B^1\Sigma_u^+$, $C^1\Pi_u$, $B'^1\Sigma_u^+$, and $D^1\Pi_u$, are strongly coupled; hence, a system of four radially coupled Schrödinger equations was solved [24]. Given in matrix form, the system is written as

$$\{-\frac{1}{2\mu_{HD}}\,[\mathbf{I}\,\frac{d^2}{dR^2} - \mathbf{I}\,\frac{J'(J'+1)}{R^2} + \mathbf{A}(R) + 2\mathbf{B}(R)\frac{d}{dR}] + \mathbf{U}(R)\}\,\boldsymbol{\varphi}(R) = E\boldsymbol{\varphi}(R) \tag{2.1}$$

with μ_{HD} the reduced mass of HD and $\mu_{HD}\prime$ its dimensionless form

$$\mu_{HD} = \frac{m_p m_d}{m_d + m_p}\,;\; \mu_{HD}\prime = \mu_{HD}/m_e \tag{2.2}$$

and m_p and m_d the mass of the proton and deuteron. $\mathbf{I}$ is the identity matrix and $\mathbf{U}(R)$ is the diagonal matrix of adiabatic potential curves. The diagonal elements of the $\mathbf{A}(R)$ matrix are the adiabatic corrections obtained from Ref. [21] for the $^1\Sigma_u^+$ states and from Ref. [22] for the $^1\Pi_u$ states. The off-diagonal elements in $\mathbf{A}$ involve both nonadiabatic couplings between states of the same symmetry ($\Sigma-\Sigma$ or $\Pi-\Pi$) and rotational couplings between $\Sigma-\Pi$ states, and finally $\mathbf{B}(R)$ is the radial coupling matrix. The non-adiabatic corrections are obtained from Ref. [23].

The Fourier Grid Hamiltonian method [24] was used to solve the coupled equations, where all the energy values and the coupled-channel wave functions are obtained in one single diagonalization of the Hamiltonian matrix expressed

Table 2.1: Measured wavelengths of lines, where P(J''), Q(J'') and R(J'') have the usual meaning of a rotational transition, in the $B^1\Sigma_u^+$–$X^1\Sigma_g^+$ Lyman bands (indicated as Lv) and $C^1\Pi_u$–$X^1\Sigma_g^+$ Werner bands (indicated as Wv) for HD with the Amsterdam narrow band extreme ultraviolet laser facility and the K_i coefficients as calculated. The typical uncertainty in the measured wavelengths is $\Delta\lambda = 0.000\,005$ nm, while that in the sensitivity coefficients is $\Delta K_i = 0.00015$.

Line	λ_0 (nm)	K_i	Line	λ_0 (nm)	K_i
L0P1	110.729 245	−0.00789	L6R3	103.536 700	0.02064
L0P2	110.911 618*	−0.00950	L6R4	103.790 376	0.01831
L0P3	111.166 568*		L7P1	102.262 976	0.02722
L0R0	110.584 055	−0.00654	L7P2	102.425 462	0.02551
L0R1	110.621 689	−0.00070	L7P3	102.656 725	0.02318
L0R2	110.732 767	−0.00811	L7R0	102.146 045	0.02831
L1P1	109.340 155	−0.00173	L7R1	102.191 899	0.02778
L1P2	109.519 532	−0.00347	L7R2	102.307 083	0.02644
L1P3	109.771 190	−0.00589	L7R3	102.491 165	0.02453
L1R0	109.200 126	−0.00038	L7R4	102.743 486	0.02216
L1R1	109.239 875	−0.00084	L8P1	101.260 079	0.03086
L1R2	109.352 696	−0.00203	L8P2	101.420 145	0.02915
L1R3	109.538 262	−0.00384	L8P3	101.648 369	0.02684
L2P2	108.194 838	0.00224	L8R0	101.146 180	0.03193
L2R0	107.883 104	0.00528	L8R1	101.192 611	0.03137
L2R1	107.924 459	0.00483	L8R2	101.307 728	0.03007
L3P1	106.758 691	0.00939	L8R3	101.491 089	0.02810
L3P2	106.932 076	0.00762	L8R4	101.742 011	0.02575
L3P3	107.176 737	0.00526	L9P1	100.300 544	0.03086
L3P4	107.491 936	0.00251	L9P2	100.458 215*	0.03257
L3R0	106.627 568	0.01061	L9P3	100.683 381	0.02684
L3R1	106.670 180*	0.01014	L9R0	100.189 413	0.03193
L3R2	106.784 752	0.00889	L9R1	100.236 220	0.03137
L3R3	106.970 884	0.00702	L9R2	100.351 037	0.03007
L3R4	107.227 954	0.00474	L9R4	100.782 338	0.02575
L4P1	105.556 544	0.01435	L16P1	94.583 158	0.05096
L4P2	105.727 058	0.01263	L16P2	94.696 040	0.04933
L4R0	105.429 354	0.01557	L16P3	94.872 485	0.04711
L4R2	105.587 950	0.01379	L16R0	94.534 329	0.05186
L5P1	104.408 545	0.01898	L16R1	94.629 663	0.05127
L5P2	104.576 264	0.01724	L16R2	94.773 610	0.04987
L5P3	104.814 022	0.01486	L16R3	94.981 204	0.04786
L5R0	104.285 005	0.02012	W0P2	101.000 728	−0.00676
L5R1	104.329 502	0.01959	W0P3	101.176 906	−0.00857
L5R2	104.444 653	0.01832	W0P4	101.394 793	−0.01050
L5R3	104.630 031	0.01644	W0Q1	100.820 291	−0.00486
L5R4	104.884 999	0.01411	W0Q2	100.908 028	−0.00590
L6P1	103.311 624	0.02325	W0Q4	101.212 698	−0.00880
L6P2	103.476 669	0.02154	W0R0	100.729 020	−0.00390
L6P3	103.711 120*	0.01923	W0R1	100.725 357	−0.00388
L6R0	103.191 493	0.02440	W0R2	100.765 326	−0.00441
L6R1	103.236 721	0.02389	W0R3	100.848 750	−0.00528
L6R2	103.351 929	0.02255			

* Obtained using the combination differences from Ref. [19]

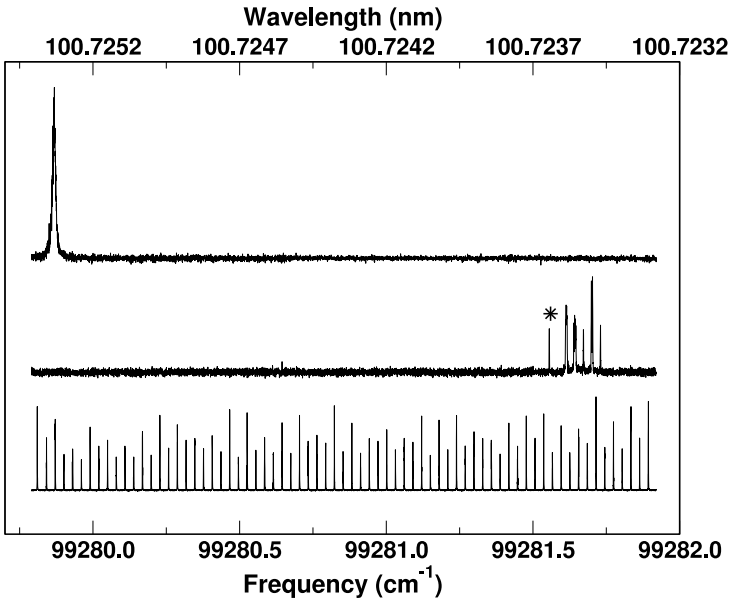

Figure 2.1: Recording of the W0R1 line of HD (upper) with étalon markers (lower) and an I_2-saturation spectrum (middle) for calibration. The line marked with an asterisk is the t-hyperfine component of the B-X(11,2) P(52) rotational line in I_2 at 16 546.926 62 cm^{-1} used as an absolute reference.

in a discrete variable representation. Solutions of nonadiabatic wave function are represented as a four-component vector:

$$\varphi_i(R) = \{\varphi_{n,i}(R), \varphi_{n',i}(R)...\}, \tag{2.3}$$

where the label n refers to the particular electronic state belonging to $\{B, B', C, D\}$.

The $X^1\Sigma_g^+$ ground state was treated separately. Its rovibrational energy levels were calculated by solving the single Schrödinger equation

$$\{-\frac{1}{2\mu_{HD}}\frac{d^2}{dR^2} + \frac{J''(J''+1)}{2\mu_{HD}R^2} + U_X(R)\}\varphi_X(R) = E_X\varphi_X(R) \tag{2.4}$$

for each rotational quantum number J'' in the adiabatic approximation, adding the corresponding centrifugal term to the *ab initio* potential $U_X(R)$, which includes the adiabatic correction into the Born-Oppenheimer potential, computed by Wolniewicz [25]. The relativistic and radiative corrections [26] were also taken into account in the present calculations.

The $X^1\Sigma_g^+$ state in hydrogen undergoes a weak perturbative shift caused by nonadiabatic interactions with excited states of symmetries Σ_g and Π_g, leading

to regular shifts ΔE_x. This was taken into account by means of semiempirical relations [27]

$$\Delta E_x = E_{\Sigma_g} + J''(J''+1)E_{\Pi_g}. \tag{2.5}$$

Furthermore, the HD molecule is subject to electronic inversion symmetry breaking ($g-u$), giving rise to interactions between states of opposite u and g symmetries [28]. This causes a supplementary downward shift of the $X^1\Sigma_g^+$ levels of HD by

$$\Delta E_x^{ug} = E_{\Sigma_u} + J''(J''+1)E_{\Pi_u} \tag{2.6}$$

The latter correction was included in the calculation of level energies of the $X^1\Sigma_g^+$ quantum states and the wavelengths of the P(J''), Q(J'') and R(J'') transitions in the corresponding Lyman and Werner bands. The effects of symmetry-breaking interactions between $EF^1\Sigma_g^+$ levels and B and C levels [13, 18] are not included here, because only incomplete *ab initio* coupling operators are available [29]. Tentative calculations including these data showed that for the lines reported in Table 2.1, the corresponding excited levels are almost unperturbed, resulting in wavelength shifts less than 10^{-4} nm and negligible changes in K_i coefficients.

The procedure to solve the coupled Schrödinger equations, derive the level energies for ground and excited states, and determine the transition wavelengths λ_i of the HD lines, was performed for various values of the relevant mass for the problem, *i.e.*, the dimensionless $\mu_{HD'}$ as defined in Eq. (2.2). As

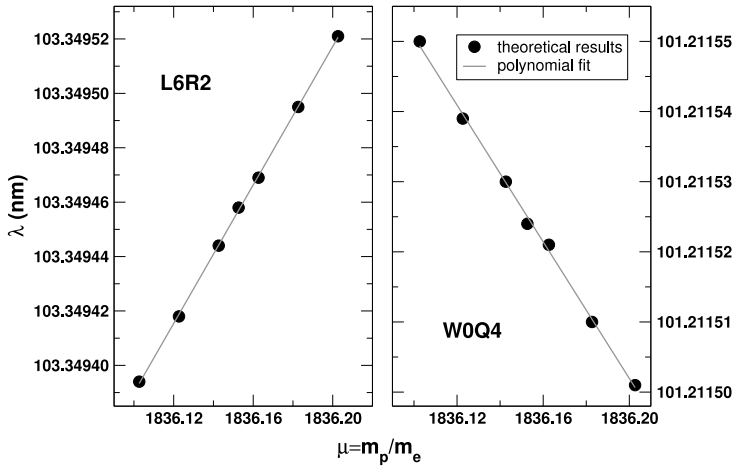

Figure 2.2: Calculation of transition wavelengths as a function of μ for two lines in HD. It illustrates that some lines undergo an upward shift and others a downward shift upon a variation of μ.

a first, intuitive, and obvious approximation, the reduced mass of HD is considered to scale as the proton mass m_p, hence $\mu_{HD\prime} = a\mu$, with a a proportionality constant of no influence on the analysis ($a = 0.667$ for HD, while $a = 0.5$ for H_2). The physical background of this assumption is that baryonic mass is considered independent of quark composition. Then the sensitivity coefficient can be expressed in the usual form as

$$K_i = \frac{d \ln \lambda_i}{d \ln \mu_{HD\prime}} = \frac{d \ln \lambda_i}{d \ln \mu}. \tag{2.7}$$

The HD transition wavelengths were calculated for a range of values of the proton-electron mass ratio μ around the experimental value of μ_0 (according to Ref. [30] $\mu_0 = 1836.152\,672\,61$). Since an indication for a possible variation was found at a level of $\Delta\mu/\mu \sim 2.4 \times 10^{-5}$ the values were taken on a grid covering $[1836.10 - 1836.21]$. In Fig. 2.2 results for transition wavelengths as a function of μ are displayed for some HD lines. For each spectral line seven calculations were performed (at μ_0 and other points as represented in Fig. 2.2). Values for K_i for each individual spectral line i were then computed by performing a polynomial fit to the slopes, a procedure also yielding an uncertainty estimate on the results. The resulting values for the K_i are included in Table 2.1 with the experimental wavelengths.

The package of present observations of accurate wavelength positions λ_i and the calculation of sensitivity factors K_i for the HD molecule can be utilized in estimating constraints on possible variations of the proton-electron mass ratio μ, or in obtaining proof of a variation of this fundamental constant. HD and H_2 lines can be included in a comprehensive analysis of $\Delta\mu/\mu$ through fitting of all molecular lines to

$$\frac{\lambda_i}{\lambda_0} = (1 + z_{abs})(1 + \frac{\Delta\mu}{\mu} K_i) \tag{2.8}$$

with z_{abs} the overall redshift of the absorbing cloud.

As discussed in Ref. [10], the proton mass m_p is proportional to a fundamental parameter, the quantum chromodynamic scale Λ_{QCD}. A fundamental dimensionless parameter Λ_{QCD}/m_e can be defined in the standard model that is directly probed in the studies comparing molecular lines in the laboratory and at at high redshift via

$$\frac{\Delta(\Lambda_{QCD}/m_e)}{\Lambda_{QCD}/m_e} = \frac{\Delta\mu}{\mu}. \tag{2.9}$$

Hence, through $\Delta\mu/\mu$ effectively the evolution of the strong force with respect to that of the electroweak scale is probed.

It is conceivable to go one step beyond this first-order evaluation; hypothetically, in second order masses of quark constituents may undergo a different time evolution. Such composition-dependent scenarios have been predicted in the framework of string theorie(s) [31] and they could be assessed by analyzing

H_2 and HD spectra simultaneously. Under such conditions Eq. (2.7) would no longer hold and HD sensitivity coefficients could be calculated, adapted to the scenario of choice by invoking different effects on m_p/m_e and m_d/m_e. Probing of such second-order effects would require astrophysical spectra of extreme quality in terms of resolution and signal-to-noise ratio, beyond that of Ref. [3], that may be considered as first observations. A future generation of planned telescopes with 30-40 m dishes may provide such data.

This study was supported by the EC Integrated Infrastructure Initiative action (No. RI3-CT-2003-506350). M.R. thanks the LCVU group for the hospitality during his stay in Amsterdam.

Chapter 3

Fourier-Transform spectroscopy of HD in the Vacuum Ultraviolet at $\lambda = 87 - 112$ nm

Abstract

Absorption spectroscopy in the vacuum ultraviolet (VUV) domain was performed on the hydrogen-deuteride molecule with a novel Fourier-Transform spectrometer based upon wavefront division interferometry. This unique instrument, which is a permanent endstation of the undulator-based beamline DESIRS on the synchrotron SOLEIL facility, opens the way to Fourier-Transform spectroscopy in the VUV range. The HD spectral lines in the Lyman and Werner bands were recorded in the 87-112 nm range from a quasi-static gas sample in a windowless configuration and with a Doppler-limited resolution. Line positions of some 268 transitions in the $B^1\Sigma_u^+\,(v' = 0 - 30) \leftarrow X^1\Sigma_g^+\,(v'' = 0)$ Lyman bands and 141 transitions in the $C^1\Pi_u(v' = 0 - 10) \leftarrow X^1\Sigma_g^+(v'' = 0)$ Werner bands were deduced with uncertainties of 0.04 $\mathrm{cm}^{-1}(1\sigma)$ which correspond to $\Delta\lambda/\lambda \sim 4 \times 10^{-7}$. This extensive laboratory database is of relevance for comparison with astronomical observations of H_2 and HD spectra from highly redshifted objects, with the goal of extracting a possible variation of the proton-to-electron mass ratio ($\mu = m_p/m_e$) on a cosmological time scale. For this reason also calculations of the so-called sensitivity coefficients K_i were performed in order to allow for deducing constraints on $\Delta\mu/\mu$. The K_i coefficients, associated with the line shift that each spectral line undergoes as a result of a varying value for μ, were derived from calculations as a function of μ solving the Schrödinger equation using *ab initio* potentials.

3.1 Introduction

The $B^1\Sigma_u^+$ - $X^1\Sigma_g^+$ Lyman bands and the $C^1\Pi_u$ - $X^1\Sigma_g^+$ Werner bands are the strongest electronic absorption systems in the hydrogen molecule. The electronic transition relates to the $1s - 2p$ transition in the hydrogen atom, also known as the Lyman-α line. In the molecular case the $2p$-orbital is either aligned along the molecular axis, the $2p\sigma_u$-orbital giving rise to the $B^1\Sigma_u^+$ state, or perpendicular to the molecular axis, the $2p\pi_u$ orbital, giving rise to the doubly degenerate $C^1\Pi_u$ state; the latter degeneracy is lifted by non-Born-Oppenheimer effects (Λ-doubling) giving rise to non-degenerate $C^1\Pi_u^+$ and $C^1\Pi_u^-$ states. Band structure is imposed due to the rotational and vibrational substructure of the excited states, while in most absorption studies only a few rotational states are populated in the lowest $X^1\Sigma_g^+\,(v = 0)$ rovibronic ground state. The absorption spectrum of the Lyman and Werner bands in the hydrogen molecule are blue-shifted from the atomic Lyman-α transition at $\lambda = 121$ nm. This is understood from the fact that the binding energies in the $B^1\Sigma_u^+$ and $C^1\Pi_u$ states are less than in the $X^1\Sigma_g^+$ ground electronic state. Hence, the molecular absorption spectrum falls in the VUV domain starting at $\lambda = 112$ nm and progressing towards shorter wavelengths.

Because hydrogen is the most abundant molecular species in the Universe, the strong Lyman and Werner band systems are ubiquitously observed in outer space. Nevertheless it took until 1970 for the first observation of molecular hydrogen in space was reported by Carruthers [32] using a rocket borne spectrometer observing from high altitudes, thereby evading atmospheric absorption of the vacuum ultraviolet radiation. Soon thereafter molecular hydrogen was also observed in the line of sight of highly redshifted quasars [33, 34]. More recently in addition to the main H_2 isotopologue also the hydrogen deuteride molecule has been detected in quasars [3, 35, 36]. A special feature of the HD isotopologue is the phenomenon of breaking of the inversion symmetry, or the mixing between states of *gerade* and *ungerade* symmetry [28]. One effect of this phenomenon is the interaction between $B^1\Sigma_u^+$ and $C^1\Pi_u$ states with $EF^1\Sigma_g^+$ states, lending intensity for absorption in the $EF - X$ system in HD.

A seminal study on the absorption and emission spectra of the Lyman and Werner systems in HD has been performed by Dabrowski and Herzberg using a classical grating spectrograph [13]. The resolution obtained in this Doppler-limited study was 1.0 cm^{-1}, while the accuracy of the line positions was several 0.1 cm^{-1}. Some twenty years later the spectroscopy of some of the Lyman and Werner bands was re-investigated using a tunable laser system in the vacuum ultraviolet and excitation in a molecular beam [18], thus lowering the resolution to 0.25 cm^{-1} and the absolute accuracy to below 0.1 cm^{-1}. Recently the spectra in the range $\lambda = 100 - 112$ nm were re-investigated with the use of an improved VUV-laser system, yielding spectral linewidths of 0.02 cm^{-1} and absolute accuracies of 0.005 cm^{-1} [37]. Previously the $B - X(v', 0)$ Lyman

bands had been investigated for $v' = 0-2$ [16] and for $v' = 15$ [17] at this high accuracy. The region near the ionization threshold in HD had been investigated at high resolution employing a narrowband VUV laser [38].

Motivated by the need for accurate wavelength positions and in order to extract tight constraints on the variation of the proton-to-electron mass ratio from quasar absorption data [7, 15, 39], now that also spectral lines of HD have been observed and may be included in the analysis [3, 35, 36], we set out to reinvestigate the VUV absorption spectrum of HD. The broadly covering investigation of Dabrowski and Herzberg [13] does not have sufficient accuracy, *i.e.* is less accurate than the high redshift lines obtained from astronomical observation. At the same time the laser investigations [16–18, 37] lack the broad coverage and still some gaps exist in the knowledge of the laboratory data of HD.

The availability of the novel Fourier-Transform (FT) spectrometer in the vacuum ultraviolet range allowed us to remeasure in HD the Lyman absorption bands up to $v' = 30$ and the Werner bands up to $v' = 10$. Wavelength positions of over 400 lines in the HD absorption spectrum were determined with an uncertainty of 0.04 cm^{-1}, or $\Delta\lambda/\lambda = 4 \times 10^{-7}$. The internal calibration of the FT instrument was improved during the course of the investigation through the use of the previously laser-calibrated lines of HD(at the 5×10^{-8} level) in the ranges where they are available. As such the present investigation is also a test of the accuracy and the capabilities of the unique FT instrument in the VUV domain.

Methods to determine constraints on a variation of the proton-to-electron mass ratio from spectral lines in molecules require three ingredients. Besides the spectral line positions observed at high redshift, and an accurate laboratory data set of wavelengths, also knowledge is required on the value of the sensitivity coefficients that determine how far lines will shift as a result of a change in mass ratio. For the case of H_2 such sensitivity coefficients were calculated by semi-empirical methods [7, 8], and alternatively by *ab initio* calculations [14]. In a previous study on the laser calibration of part of the HD spectrum calculations of some sensitivity coefficients were reported [37]. In the present paper such calculations are further detailed and extended to the broad coverage of the spectrum.

3.2 Experimental setup

Absorption spectra of the hydrogen deuteride molecule HD have been recorded in the $\lambda = 87 - 112$ nm range using a FT spectrometer, which is installed as a permanent endstation on the VUV undulator-based DESIRS beamline on the French synchrotron facility SOLEIL [40]. The FT instrument is the first of its kind to achieve high resolution transmission spectra in this short-wavelength windowless regime. Previously, with the aid of optical beam-splitters to per-

form amplitude-division interferometry for dividing paths in the Michelson configuration, a FT spectrometer had been operated at wavelengths as short as λ=140 nm [41]. With the here described unique instrument the advantageous properties of FT spectroscopy, the capability to reach high spectral resolving power $\lambda/\Delta\lambda$ as well as the multiplex capability, are extended to wavelengths beyond the MgF_2 cutoff. This can be accomplished by replacing the amplitude-division concept by a wavefront-division method in obtaining interferograms. The present recordings of high resolution spectra of HD serve also as a demonstration of the obtainable accuracies on wavelengths positions of spectral lines with the novel instrument, owing to the availability of a multitude of accurately calibrated lines from laser experiments.

The FT spectrometer can achieve an ultimate theoretical resolving power of around one million over the entire VUV spectral range covered by the instrument (40-180 nm), which is between 5 and 10 times better than the capabilities of state-of-the-art VUV grating-based spectrometers. A first version of the VUV FT spectrometer, operating in the mid-UV range, has been described in detail [42]. Although the underlying physical principles are similar, the DESIRS instrument has been improved and can now be operated in the 40-180 nm range (6-30 eV). Here we give a brief description on the main features of operation of the instrument, relevant to the current study, while a more complete report is in preparation [43].

The interferometer is based upon a modified design of the traditional Fresnel bi-mirror interferometer. Two roof reflectors, separated by a 100 μm gap

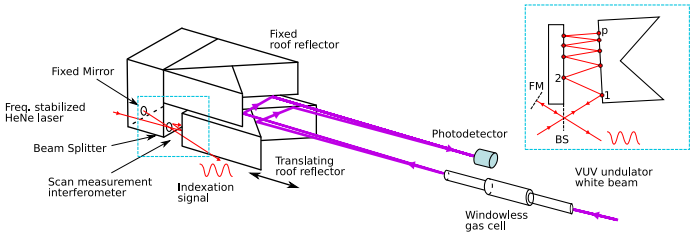

Figure 3.1: Experimental layout of the VUV FT spectrometer setup. The VUV wavefront division interferometer is facing the VUV synchrotron beam. The two roof-shape reflectors are slightly tilted in order to make the two reflected beams overlap and interfere on a photodiode. A part of the scanning measurement setup is shown on the back side. The incident frequency-stabilized HeNe laser beam is splitted by a beam splitter (BS), the reference beam is reflected at normal incidence by a plane fixed mirror (FM), the transmitted beam is reflected p times between the back of the moving VUV reflector and a plane mirror part of the reference optical block that includes the fixed VUV reflector. All the fixed optical elements are part of the same optical block in order to minimize possible differential errors. The multireflection setup ensures the required high sensitivity for the movement indexation.

and having an angle of 0.35 mrad between each other are illuminated in the vicinity of the gap by the coherent synchrotron radiation beam encoded with information on the HD absorption features. The reflected beams from both reflectors then overlap and interfere at the plane of the detector located at a distance of 1.3 m. The inteferometric signal is recorded continuously at equal path difference intervals by translating one of the reflectors. The source spectral distribution is then recovered by performing a Fourier transformation onto the recorded interferogram. Working in the VUV range requires special care, since optical and mechanical tolerances are directly related to the operation wavelength. Therefore the motion of the reflector is controlled by a sophisticated system which has been especially developed for the VUV FT spectrometer. Briefly, it consists of a highly sensitive multireflection deflectometer and a multipass Michelson interferometer, both employed to ensure that the required precision is achieved.

As it is important for the recalibration and the error estimation procedures, the multireflection Michelson interferometer is briefly described hereafter (a more detailed description can be found elsewhere [40, 44]). The still reflector has its back side fixed to a stable solid optical block while the back surface of the moving reflector creates a small angle with respect to the surface of the optical block, thus creating a small angle air wedge (fig. 1). When inserting a HeNe laser beam probe in this wedge with an appropriate entrance angle, the laser beam can be exactly retro-reflected and overlapping the entrance path (after p reflections between the two planes of the wedge as shown in the inset of Fig. 1). This multireflection set-up is the moving arm of a traditional Michelson interferometer used here as a control system. The sinusoidal interferometric signal period given by the interferometer is then directly related to the p parameter. Owing to the multireflection amplification, the period of the signal is roughly inversely proportional to the number of reflections p, namely, period $\approx \lambda_{laser}/2p$ (note that this is the period in terms of the displacement of the moving reflector). The VUV interferometric signal is then triggered at regular path difference steps following a sampling comb generated from the HeNe interferometric signal (twice per signal period). The p parameter can be set *in-situ* in the 7 to 16 range. This allows one to adapt the sampling interval of the interferogram as a function of the smallest wavelength in the spectrum in order to have at least two points per fringe (Nyquist condition). This is a powerful way to keep the relative spectral resolution close to the maximum value, determined by the number of recorded samples, over a large spectral range.

Ideally, the geometry of the control system is perfectly known, and therewith the value of the sampling interval for a given p as well. Hence, the spectral scale is also perfectly determined for each value of p. In practice, some geometrical parameters are not well known, and are difficult to measure. The consequence is that the spectral calibration deviates from the ideal values, the

deviation being p-dependent and in the order of a few 10^{-7}. Most of the measurements in the present study were done at $p = 8$ and a minor part at $p = 7$.

OPHELIE2, the undulator feeding the DESIRS beamline provides a VUV pseudo-white radiation with a broadband Gaussian-like spectrum with a $\delta E/E$ relative spectral bandwidth of 7%. The position of the spectral window can be easily tuned over the whole VUV range, by tuning the magnetic field of the undulator, operated in the linear vertical polarization mode [45]. Only the fundamental radiation of the undulator is used. The higher harmonics are being cut-off by a free flow gas filter acting as a low-energy pass filter [46]. The undulator white beam is only reflected by three mirrors at a 20^o grazing incidence angle before entering the FT spectrometer, ensuring a high spectral brightness. This is the relevant photometric parameter for wavefront-division interferometry as this technique requires a high density spatially coherent photon flux. The broad bandwidth synchrotron beam is then sent towards a differentially-pumped multipurpose gas sample chamber, containing the sample. The measured HD gas is introduced into a free flow windowless T-shaped gas cell, which consists of a cylindrical steel tube 100 mm long and 30 mm inside diameter. This configuration leads to an inhomogeneous density distribution along the direction of the synchrotron radiation beam. By regulating the pressure at the gas cell input an integrated column density up to a few times 10^{18} particles per cm^2 can be achieved. Beyond the interaction with the gas the synchrotron light is used as an input source for the FT spectrometer.

Interferograms are recorded "on the fly", *i.e.* sampling is performed during the continuous translation of the moving arm of the interferometer yielding a typical scan time of 3 min, during which 512 K samples are acquired. Each final spectrum at a certain column density represents a summation over 100 individual spectra. The total time to acquire such a spectrum spanning over 5000 cm^{-1} is approximately two hours. Fig. 2 shows an example of such an averaged spectrum.

All measurements were done at room temperature, where the Doppler width for HD is $0.7 - 0.8$ cm^{-1}. Therefore the ultimate instrumental resolution is not needed. Instead, it was optimized to gather a sufficient amount of points per spectral line and keep the collection time for an interferogram as low as possible so it can be used for improving the signal-to-noise ratio (S/N is proportional to the square root of the number of averaging individual spectra). For the present study an optimized measurement time/resolution conditions with an acceptable S/N ratio were achieved by setting the instrumental line width between 0.3 and 0.4 cm^{-1} corresponding to a resolving power of about 350 000.

It is worth mentioning that the capabilities of the FT spectrometer were not fully exploited due to a relatively poor signal-to-noise ratio in some of the spectral regions covered by the instrument. FT spectroscopy is a photon noise-limited technique and the S/N ratio obtained is proportional to the square root of the photon flux. The latter was sub-optimal due to slight misalignment

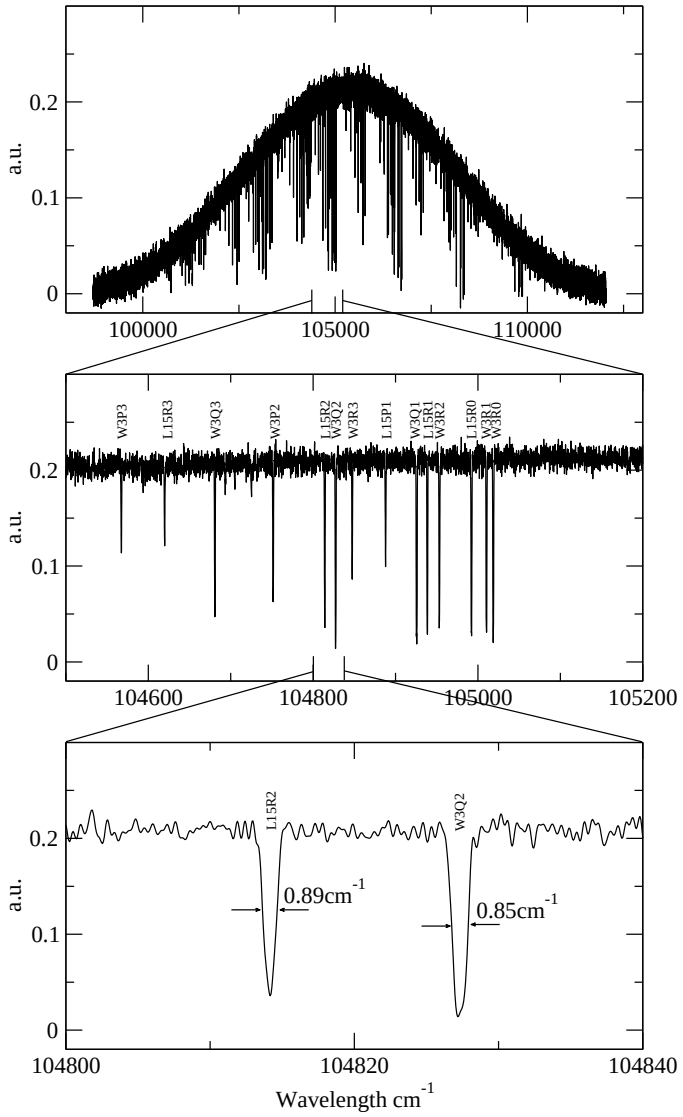

Figure 3.2: This spectrum represents one of the five windows covering the entire investigated spectral range - 90 000-115 000 cm^{-1}. It is a product of averaging 100 individual spectra. The Gaussian-like envelope represents the synchrotron radiation spectrum in which the absorption features of HD are encoded. The measurements were taken at room temperature and pressure at the input of the gas cell of 5.6×10^{-3} mbar. The bottom part of the figure focuses on a zoom on $B^1\Sigma_u^+ (v = 15) \leftarrow X^1\Sigma_g^+ (v = 0)$ R(2) and $C^1\Pi^- (v = 3) \leftarrow X^1\Sigma_g^+ (v = 0)$ Q(2) transitions from Lyman and Werner band which are shortly labeled as L15R2 and W3Q2. It can be seen that the linewidths are determined by Doppler broadening. It should be noted also that for better visibility the spectrum has been interpolated.

and especially due to small amounts of carbon contamination on some of the FT spectrometer and beamline optics giving rise to absorption in the spectral region of interest.

3.3 Experimental results and discussion

Some 400 absorption lines of the Lyman and Werner bands of HD have been measured with absolute accuracies of 0.04 cm^{-1} (*i.e.* 4×10^{-7} relative accuracies). The transition frequencies are presented in Table 3.1 for the Lyman bands and Table 3.2 for Werner bands, respectively. Some of the line positions have previously been calibrated at better accuracies - 5×10^{-8} [16,17,37], while Hinnen *et al.* [18] performed a lower resolution laser-based study with a claimed accuracy of 3.5×10^{-7}. For the remainder the best results known are those from Dabrowski and Herzberg [13] with accuracies of a few $\times 10^{-6}$. The present results therefore yield an order of magnitude improvement in accuracy for the majority of the lines.

The spectral range 90 000-115 000 cm^{-1} was divided into five different measurements regions, each covering around 5 000 cm^{-1}. In order to have sufficiently strong but saturated absorption features for each transition with rotational number up to $J = 5$, scans at several column densities for each spectral region are necessary. We have performed measurements at four different column densities for each spectral window, taking into account that the bands tend to become stronger towards shorter wavelength.

A Fourier-Transform spectrum is characterized by a constant noise level determined ideally by the photon flux reaching the detector and the number of averaged individual spectra. Each spectral line therefore exhibits its own signal-to-noise ratio determined by the amount of absorption. All lines with $S/N < 6$ were discarded to ensure that the fitting procedure was accurate. Since measurements were performed at four different column densities, at least two of the four spectra will contain a specific line unsaturated. The final line position is then averaged over these two measurements.

Assuming proper sampling Fourier-Transform spectroscopy provides an intrinsically linear frequency scale. Initially, calibrations were performed using as a reference the Ar $(3p)^5(^2P_{\frac{3}{2}})9d[\frac{3}{2}] \leftarrow (3p)^6\,{}^1S_0$ transition, known with an accuracy of 0.03 cm^{-1} [47]. However, during the analysis it was found that setting the FT spectrometer at different p parameters introduces small variations in the calibration branch geometry (see inset Fig.1). Because this effect introduces systematic errors of $\sim$ few $\times 10^{-7}$ a recalibration procedure was implemented, relying on the many HD lines in the spectrum that are known to an accuracy of 5×10^{-8} from laser based studies [16,17,37]. The recalibration led to a linear correction of the spectrum and an improvement on the accuracy of the frequency axis.

The statistical uncertainty of a line position in a FT spectrum with noise

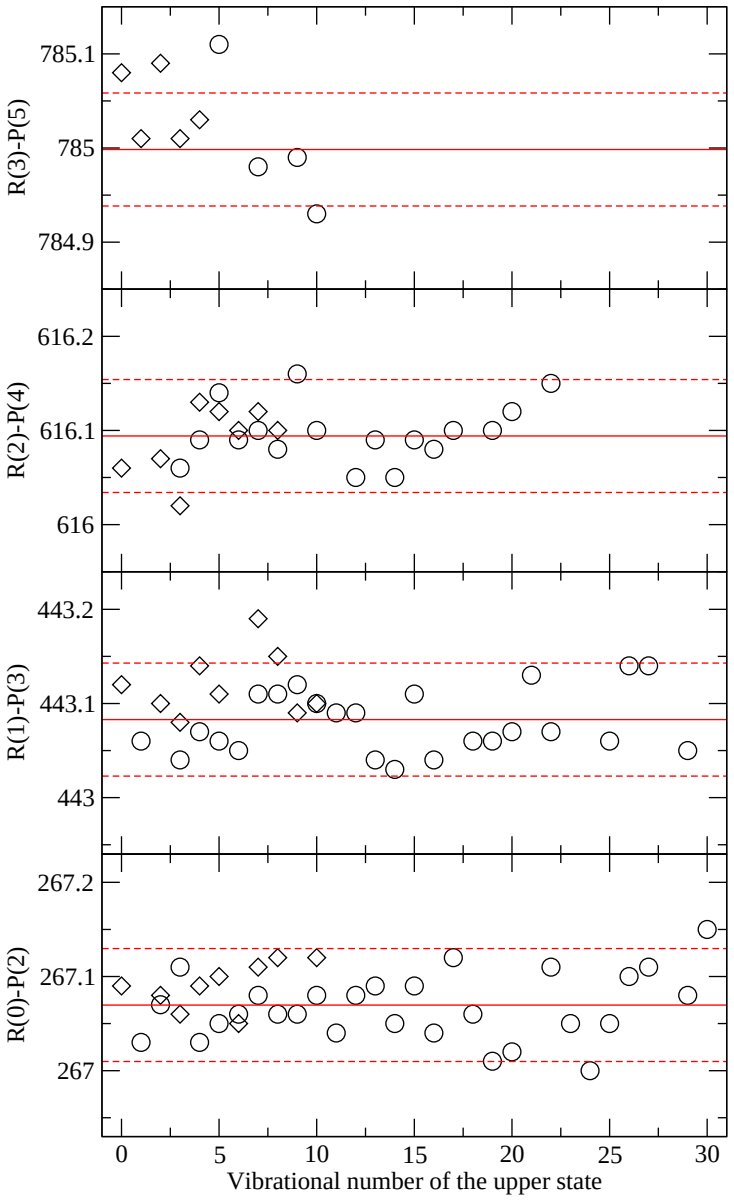

Figure 3.3: Combination differences, *i.e.* differences between R(J) and P(J+2) transition frequencies, as constructed from the results of Table 3.1 and Table 3.2. Values are compared to the $\Delta J = 2$ splittings as accurately known from far-infrared FT spectroscopy [19]; this is represented by the central line. The dashed lines indicate the estimated 1σ error bars of 0.06 cm^{-1}. The X axis represents the vibrational number of the upper state. Combination differences calculated from transitions belonging to the Lyman band are shown with circles, while the ones belonging to the Werner band are shown with diamonds.

is governed by the formula [48]:

$$\Delta\sigma \sim \frac{W}{\sqrt{N_w}} \frac{f}{S/N} \tag{3.1}$$

where W is the FWHM of the line, N_w represents the number of the experimental points determining the line (defined as number of points above the half maximum level), S/N is the signal to noise ratio for the specific line and f is a geometrical factor relating to how well the kernel function matches the line shape. In the case of room-temperature gas-cell spectrum of HD for the Lyman and Werner bands the Doppler effect completely determines the lineshape of the non-saturated lines. Then using typical values of $W \sim 0.8$ cm^{-1} , $N_w = 4$, $f \sim 1$ and $S/N > 6$ a statistical value of 0.07 cm^{-1} is estimated. However, this is a worst case estimation when the line is determined in only one scan with the worst S/N ratio. In practice we have at least two spectra measured at different column densities ensuring that at least one of them has a much higher S/N ratio. Another estimation of the statistical uncertainty can be derived from estimating the spread of the transitions of the Fourier spectrum with respect to the laser calibrated lines [16,17,37] (Δ^{L} in the tables). Such a comparison between data sets yields a standard deviation of 0.03 cm^{-1} for the deviations. As a conservative estimate we put 0.04 cm^{-1} as the standard deviation.

The R(J) and P($J+2$) transitions of a certain vibrational band probe the same rotational level of the upper state. These combination differences can be compared with the high-precision far-infrared data from the quadrupole spectrum [19] and used for verification. Based on the 0.04 cm^{-1} uncertainties for single lines the estimated uncertainties for the combination differences amount to 0.06 cm^{-1}. Fig. 3.3 shows that the present results are consistent and fall well within these error margins. It can be seen that combination differences constructed from weaker lines (R(3) - P(5)) result in larger scatterring around the true value.

In Tables 3.1 and 3.2 the fourth column Δ^{D} represents the deviations between the present data with those of Dabrowski and Herzberg. For lower energies up to $B-X(17,0)$ the difference of the present results with respect to the previous is negative with an average value of -0.23 cm^{-1}, while for higher energies it is positive with an average value of 0.17 cm^{-1}. The sudden change at $B-X(17,0)$ can also be observed in [18]. The linearity of the FT spectroscopy and the independent observations by Hinnen with laser spectroscopy suggest that this change may be the result of the calibration procedure in the classical studies.

The present results were compared with the data of Hinnen *et al.* [18]. On average a systematic offset of 0.06 cm^{-1} is found, while in a few cases the difference reaches 0.12 cm^{-1} which is outside the estimated error margin. The error estimation of 0.035 cm^{-1} in [18] was overly optimistic; later it was found that the I_2-reference calibration was offset by 0.06 cm^{-1} due to the fact that only a single spatial mode of the multimode laser beam was used in

the calibration procedure in our laboratory. The $B - X(17,0)$ R(3) line was excluded in the analysis due to an unrealistically large difference of 1 cm^{-1}, possibly due to a typo in [18]. Calibration problems also led to a reassignment of $B-X(13,0)$ R(2) to the $EF-X(6,0)$ band in [18]; in the present study it is shown that the initial assignment by Dabrowski and Herzberg [13] was correct. With the present results the combination difference involving this line lies well within the estimated value (see Figure 3.3).

Table 3.1: Transition energies (in cm^{-1}) for lines in the Lyman bands of HD. The estimated uncertainty is 0.04 $cm^{-1}(1\sigma)$ except for some very weak or blended lines. Δ^{L} and Δ^{D} represent differences of the present values with the previously reported by laser [16, 17, 37] and classical [13] spectroscopy respectively. The last column contains the sensitivity coefficient for each transition to a possible variation of the proton-to-electron mass ratio. Lines marked with *b* were blended in the spectrum.

This work		Δ^{L}	Δ^{D}	K_i	This work		Δ^{L}	Δ^{D}	K_i
$B - X(0,0)$									
R(0)	90 428.96	0.01		-0.00654					
R(1)	90 398.19	0.00		-0.00695	P(1)	90 310.38	0.00		-0.00790
R(2)	90 307.55	0.05		-0.00811	P(2)	90 161.86			-0.00969
R(3)	90 157.53			-0.00987					
$B - X(1,0)$									
R(0)	91 574.94	-0.04		-0.00038					
R(1)	91 541.65	-0.01		-0.00084	P(1)	91 457.69	-0.02		-0.00173
R(2)	91 447.22	0.00		-0.00203	P(2)	91 307.91	0.00		-0.00347
R(3)	91 292.31	0.01		-0.00384	P(3)	91 098.59	0.01		-0.00590
R(4)	91 078.00			-0.00609	P(4)	90 831.11			-0.00864
$B - X(2,0)$									
R(0)	92 692.90	-0.02		0.00528					
R(1)	92 657.39	-0.02		0.00483	P(1)	92 576.74			0.00407
R(2)	92 559.69			0.00359	P(2)	92 425.83	-0.02		0.00224
R(3)	92 400.55			0.00175	P(3)	92 214.30			-0.00014
R(4)	92 181.08			-0.00050	P(4)	91 943.60			-0.00290
$B - X(3,0)$									
R(0)	93 784.41	0.03	-0.39	0.01061					
R(1)	93 746.89		0.59	0.01014	P(1)	93 669.17	-0.02		0.00940
R(2)	93 646.31	-0.02	-0.49	0.00888	P(2)	93 517.30	-0.01	-0.13	0.00763
R(3)	93 483.39	0.00	-0.13	0.00703	P(3)	93 303.85	0.02	-0.11	0.00525
R(4)	93 259.26	0.00	-0.18	0.00474	P(4)	93 030.25	0.01	-0.13	0.00251
R(5)	92 975.56		-0.11	0.00177					
$B - X(4,0)$									
R(0)	94 850.22	-0.02	-0.54	0.01557					
R(1)	94 811.00			0.01505	P(1)	94 735.92	-0.03	-0.28	0.01435
R(2)	94 707.77		-0.23	0.01379	P(2)	94 583.19	0.01	-0.38	0.01263
R(3)	94 541.37		-0.22	0.01188	P(3)	94 367.92		-0.14	0.01024
R(4)	94 312.99		-0.57	0.00958	P(4)	94 091.68		0.01	0.00751
R(5)	94 024.26		-0.04	0.00665					

continue on the next page

This work		Δ^{L}	Δ^{D}	K_i	This work		Δ^{L}	Δ^{D}	K_i
$B-X(5,0)$									
R(0)	95 891.06	-0.01	-0.24	0.02013					
R(1)	95 850.19[b]	0.02	-0.61	0.01959	P(1)	95 777.59	-0.01	-0.31	0.01898
R(2)	95 744.52	0.03	-0.38	0.01832	P(2)	95 624.01	0.01	-0.29	0.01724
R(3)	95 574.84	-0.01	-0.16	0.01644	P(3)	95 407.13	0.05	-0.07	0.01486
R(4)	95 342.49	-0.03	0.49	0.01411	P(4)	95 128.38		-0.22	0.01214
R(5)	95 049.15		0.15	0.01113	P(5)	94 789.74		0.14	0.00880
$B-X(6,0)$									
R(0)	96 907.23	0.01	-0.27	0.02439					
R(1)	96 864.77[b]	0.01	-0.53	0.02389	P(1)	96 794.54	0.01	-0.23	0.02325
R(2)	96 756.80	0.02	-0.50	0.02255	P(2)	96 640.17	0.03	-0.23	0.02154
R(3)	96 584.11	0.00	-0.34	0.02065	P(3)	96 421.72			0.01922
R(4)	96 348.08	0.03		0.01831	P(4)	96 140.71		-0.09	0.01647
R(5)	96 050.31		0.01	0.02231	P(5)	95 799.01		-0.19	0.01313
$B-X(7,0)$									
R(0)	97 899.04	0.00	-0.47	0.02831					
R(1)	97 855.13	0.01	-0.31	0.02778	P(1)	97 787.10	0.00	-0.40	0.02722
R(2)	97 744.94[b]	0.00	-0.67	0.02644	P(2)	97 631.96	-0.01	-0.53	0.02550
R(3)	97 569.39	0.01	-0.11	0.02452	P(3)	97 412.01	-0.02	-0.39	0.02318
R(4)	97 329.80	0.03		0.02217	P(4)	97 128.84		-0.17	0.02045
R(5)	97 027.90		-0.17	0.02298	P(5)	96 784.41		-0.10	0.01711
$B-X(8,0)$									
R(0)	98 866.80	-0.01		0.03193					
R(1)	98 821.46	0.02	-0.21	0.03138	P(1)	98 755.59[b]	-0.01		0.03087
R(2)	98 709.15	0.00	-0.33	0.03007	P(2)	98 599.73	-0.01	-0.31	0.02915
R(3)	98 530.80	-0.02	-0.30	0.02809	P(3)	98 378.35	-0.01		0.02684
R(4)	98 287.77[b]	-0.05		0.02575	P(4)	98 093.07			0.02416
R(5)	97 981.89		-0.20	0.02854					
$B-X(9,0)$									
R(0)	99 810.94	0.00	-0.25	0.03530					
R(1)	99 764.34	0.00	-0.20	0.03472	P(1)	99 700.36	0.00	-0.24	0.03425
R(2)	99 650.20	0.01	-0.32	0.03337	P(2)	99 543.88		-0.18	0.03256
R(3)	99 469.46		-0.44	0.03140	P(3)	99 321.22	-0.03	-0.33	0.03024
R(4)	99 223.72	-0.01	-0.15	0.02895	P(4)	99 034.04[b]			0.02753
R(5)	98 917.88[b]			0.03040	P(5)	98 684.47		-0.04	0.02418
$B-X(10,0)$									
R(0)	100 731.64[b]		-0.46	0.03836					
R(1)	100 683.60		-0.40	0.03779	P(1)	100 621.74		-0.20	0.03734
R(2)	100 567.38		-0.22	0.03647	P(2)	100 464.56		-0.04	0.03565
R(3)	100 383.88		-0.26	0.03449	P(3)	100 240.49		-0.23	0.03337
R(4)	100 134.54		-0.36	0.03206	P(4)	99 951.28		-0.19	0.03070
R(5)	99 820.95[b]		-0.31	0.03378	P(5)	99 598.95		-0.04	0.02736
$B-X(11,0)$									
R(0)	101 624.40		-0.29	0.04119					
R(1)	101 581.01		0.82	0.04055	P(1)	101 518.29		0.76	0.04018
R(2)	101 463.13		-0.55	0.03913	P(2)	101 357.37		0.01	0.03852
R(3)	101 278.70		-0.34	0.03678	P(3)	101 137.92			0.03618

continue on the next page

This work		Δ^{L}	Δ^{D}	K_i	This work		Δ^{L}	Δ^{D}	K_i
R(4)					P(4)				
R(5)	100 703.29		0.08	0.03580	P(5)	100 493.71			0.02973
$B-X(12,0)$									
R(0)	102 503.53			0.04376					
R(1)	102 453.02[b]		-0.45	0.04316	P(1)	102 394.91		-0.43	0.04261
R(2)	102 332.80		-0.36	0.04179	P(2)	102 236.45		-0.35	0.04112
R(3)	102 147.32		-0.18	0.03982	P(3)	102 009.93		-0.22	0.03883
R(4)	101 890.90[b]			0.03744	P(4)	101 716.76		-0.17	0.03616
R(5)	101 570.43		-0.12	0.03812					
$B-X(13,0)$									
R(0)	103 356.32		0.14	0.04606					
R(1)	103 305.85		-0.41	0.04519	P(1)	103 247.83		-0.47	0.04512
R(2)	103 191.57		-0.05	0.04035	P(2)	103 089.23		-0.63	0.04345
R(3)	102 985.10		-0.04	0.03877	P(3)	102 862.81		-0.33	0.04091
R(4)	102 725.62		-0.33	0.03902	P(4)	102 575.48		-0.08	0.03475
R(5)	102 409.26			0.03986					
$B-X(14,0)$									
R(0)	104 186.14		-0.34	0.04821					
R(1)	104 133.52		-0.13	0.04762	P(1)	104 078.65[b]			0.04725
R(2)	104 010.40		-0.32	0.04623	P(2)	103 919.09		-0.52	0.04562
R(3)	103 817.85		-0.24	0.04422	P(3)	103 690.49		-0.34	0.04338
R(4)	103 557.02		-0.26	0.04182	P(4)	103 394.35		-0.18	0.04072
$B-X(15,0)$									
R(0)	104 992.05		-0.85	0.04653					
R(1)	104 938.50		-0.81	0.04828	P(1)	104 887.83			0.04919
R(2)	104 814.05		-0.35	0.04753	P(2)	104 724.97		-0.30	0.04396
R(3)	104 619.74[b]			0.04576	P(3)	104 495.39		-0.05	0.04408
R(4)	104 357.09[b]			0.04350	P(4)	104 197.97[b]			0.04207
R(5)	104 027.40		-0.07	0.04314					
$B-X(16,0)$									
R(0)	105 781.66	-0.02	0.12	0.05186					
R(1)	105 727.07	0.00		0.05128	P(1)	105 675.13[b]	0.02	0.16	0.05095
R(2)	105 601.02	-0.02	0.49	0.04987	P(2)	105 514.62	0.01	-0.08	0.04932
R(3)	105 404.63	-0.01	-0.17	0.04786	P(3)	105 284.03	0.04		0.04712
R(4)	105 139.53[b]		-0.30	0.04536	P(4)	104 984.94		-0.22	0.04447
$B-X(17,0)$									
R(0)	106 546.11		0.43	0.05333					
R(1)	106 490.13[b]			0.05269	P(1)	106 440.31		0.15	0.05252
R(2)	106 362.16		0.15	0.05124	P(2)	106 278.99		0.45	0.05081
R(3)	106 163.30[b]		0.37	0.04924	P(3)	106 047.04			0.04856
R(4)	105 895.13[b]			0.04682	P(4)	105 746.06		0.31	0.04588
$B-X(18,0)$									
R(0)	107 292.96		0.15	0.05477					
R(1)	107 236.54		0.20	0.05416	P(1)	107 187.30		0.14	0.05389
R(2)	107 107.80		0.14	0.05273	P(2)	107 025.90		0.13	0.05227
R(3)	106 908.03		0.18	0.05067	P(3)	106 793.48		0.26	0.05007
R(4)					P(4)	106 491.81			0.04741

continue on the next page

This work		Δ^{L}	Δ^{D}	K_i	This work		Δ^{L}	Δ^{D}	K_i
$B-X(19,0)$									
R(0)	108 017.12		0.47	0.05596					
R(1)	107 959.24		0.35	0.05529	P(1)	107 912.30		0.47	0.05510
R(2)	107 828.45		0.40	0.05387	P(2)	107 750.11		0.42	0.05349
R(3)	107 625.82		0.42	0.05181	P(3)	107 516.17		0.37	0.05123
R(4)	107 352.90		0.38	0.04939	P(4)	107 212.34		0.34	0.04860
$B-X(20,0)$									
R(0)	108 721.84[b]		0.12	0.05698					
R(1)	108 663.84		0.26	0.05634	P(1)	108 617.08		0.26	0.05611
R(2)	108 532.89			0.05484	P(2)	108 454.82		0.41	0.05452
R(3)	108 330.69[b]		0.51	0.05256	P(3)	108 220.76[b]			0.05231
					P(4)	107 916.77		0.66	0.04961
$B-X(21,0)$									
R(0)	109 406.64[b]		-0.04	0.05786					
R(1)	109 346.46		0.24	0.05721	P(1)	109 302.00[b]		0.24	0.05700
R(2)	109 213.09		0.28	0.05579	P(2)	109 139.02		0.36	0.05542
R(3)	109 007.01			0.05374	P(3)	108 903.33[b]		0.35	0.05321
R(4)	108 729.80		0.35	0.05127	P(4)	108 596.69[b]			0.05059
$B-X(22,0)$									
R(0)	110 071.36		0.36	0.05855					
R(1)	110 012.15		0.31	0.05778	P(1)	109 967.22		0.34	0.05775
R(2)	109 880.65		0.32	0.05570	P(2)	109 804.25		0.24	0.05613
R(3)					P(3)	109 569.08[b]			0.05381
R(4)	109 376.84		0.36	0.04924	P(4)	109 264.50		0.33	0.05053
$B-X(23,0)$									
R(0)	110 715.06		0.00	0.05915					
R(1)	110 654.10			0.05849	P(1)	110 611.67		-0.19	0.05831
R(2)	110 518.46[b]		0.85	0.05707	P(2)	110 448.01		0.57	0.05674
R(3)	110 309.35		0.53	0.05502					
R(4)	110 028.28		0.40	0.05250					
$B-X(24,0)$									
R(0)	111 347.02		-0.10	0.05895					
R(1)					P(1)	111 242.51			0.05877
R(2)	111 138.09		0.05	0.05439	P(2)	111 080.02		0.29	0.05656
R(3)	110 930.39		0.30	0.05442	P(3)	110 851.28		0.36	0.04838
R(4)	110 649.65		0.50	0.05246					
$B-X(25,0)$									
R(0)	111 955.75		-0.13	0.05989					
R(1)	111 893.57[b]		-0.10	0.05919	P(1)	111 853.85[b]		0.36	0.05905
R(2)	111 757.99		-0.11	0.05777	P(2)	111 688.70		-0.02	0.05751
R(3)	111 541.22		-0.06	0.05568	P(3)	111 450.51		-0.05	0.05530
$B-X(26,0)$									
R(0)	112 541.15		-0.06	0.05975					
R(1)	112 476.57		-0.21	0.05898	P(1)	112 440.10		-0.22	0.05922
R(2)	112 336.43		-0.21	0.05758	P(2)	112 274.05		-0.24	0.05738
R(3)	112 121.84		-0.15	0.05556	P(3)	112 033.43		-0.23	0.05510
R(4)	111 834.16		-0.21	0.05314					

continue on the next page

This work		Δ^{L}	Δ^{D}	K_i	This work		Δ^{L}	Δ^{D}	K_i
$B-X(27,0)$									
R(0)	113 112.48		0.27	0.06004					
R(1)	113 048.26		0.16	0.05933	P(1)	113 010.15		0.04	0.05921
R(2)	112 907.91[b]		-0.13	0.05785	P(2)	112 845.38		0.22	0.05768
R(3)	112 692.66		0.06	0.05571	P(3)	112 605.12		-0.06	0.05548
$B-X(28,0)$									
R(0)									
R(1)	113 598.48		-0.01	0.05907	P(1)				
R(2)	113 456.06		0.30	0.05759	P(2)	113 397.16		0.28	0.05747
R(3)	113 238.14		0.38	0.05549					
$B-X(29,0)$									
R(0)	114 198.02		-0.04	0.05951					
R(1)	114 132.33		-0.08	0.05882	P(1)	114 097.04		-0.12	0.05871
R(2)	113 989.70		-0.54	0.05728	P(2)	113 930.94		-0.07	0.05717
					P(3)	113 689.27		0.12	0.05500
$B-X(30,0)$									
R(0)	114 711.98		0.09	0.05898					
R(1)	114 644.87		0.15	0.05825	P(1)	114 611.72		-0.03	0.05823
R(2)	114 500.52			0.05673	P(2)	114 444.83		-0.06	0.05665

3.4 Calculation of the sensitivity coefficients

The present experimental investigation on the spectroscopy of HD is motivated by the possibility to include these lines in a search for a variation of the proton-electron mass ratio on a cosmological time scale [37]. In recent years HD lines have been observed in quasar absorption spectra at high redshift [3, 35], and in the most recent study on the J2123 system at redshift $z = 2.05$ HD lines are included in addition to H_2 lines to derive a constraint on $\Delta\mu/\mu$, where $\Delta\mu$ is the difference between proton-to-electron mass ratio in the present epoch $\mu_0 = m_p/m_e$ (at zero redshift) and the mass ratio μ_z for the absorbing cloud (at high redshift z) [36]. An important ingredient for such an analysis is the knowledge of the so-called sensitivity coefficients, defined as [7, 8]:

$$K_i = \frac{d(ln\lambda_i)}{d(ln\mu)} = \frac{\mu}{\lambda_i}\frac{d\lambda_i}{d\mu} = -\frac{\mu}{\sigma_i}\frac{d\sigma_i}{d\mu} \tag{3.2}$$

where $\lambda_i = 1/\sigma_i$ and $\sigma_i = E_i^{up}(v', J') - E_i^{low}(v'', J'')$ is the transition frequency. These K_i coefficients determine how much each spectral line shifts as a result of a possible variation in μ corresponding to:

$$\frac{\lambda_i^z}{\lambda_i^0} = (1 + z_{abs})(1 + \frac{\Delta\mu}{\mu}K_i) \tag{3.3}$$

Table 3.2: Transition energies (in cm^{-1}) for lines in the Werner bands of HD. The estimated uncertainty of all transitions is 0.04 $cm^{-1}(1\sigma)$. Δ^L and Δ^D represent differences of the present values with the previously reported by laser [16, 17, 37] and classical [13] spectroscopy respectively. The last column contains the sensitivity coefficient for each transition to a possible variation of the proton-to-electron mass ratio.

This work		Δ^L	Δ^D	K_i	This work		Δ^L	Δ^D	K_i	This work		Δ^L	Δ^D	K_i
C(v=0)														
R(0)	99 276.28	0.02	-0.68	-0.00391										
R(1)	99 279.88	0.02	-0.25	-0.00389	Q(1)	99 186.39	0.01	-0.33	-0.00486					
R(2)	99 240.47	-0.02	-0.29	-0.00441	Q(2)	99 100.14	0.00	0.00	-0.00589	P(2)	99 009.18	0.00	-0.23	-0.00677
R(3)	99 158.41	0.01		-0.00529	Q(3)	98 971.63		-0.14	-0.00726	P(3)	98 836.76	-0.03		-0.00857
R(4)	99 032.36			-0.00627	Q(4)	98 801.81	-0.02		-0.00880	P(4)	98 624.40	0.01	-0.25	-0.01051
R(5)					Q(5)	98 592.04		-0.16	-0.01078	P(5)	98 373.33		-0.15	-0.01282
C(v=1)														
R(0)	101 289.54[b]			0.00562										
R(1)	101 289.54[b]			0.00559	Q(1)	101 199.80			0.00467					
R(2)	101 243.53		-0.52	0.00507	Q(2)	101 109.49		-0.58	0.00359	P(2)	101 022.66			0.00284
R(3)	101 152.28		-0.17	0.00450	Q(3)	100 974.85			0.00219	P(3)	100 846.23			0.00105
R(4)	101 002.18		0.14	0.01675	Q(4)	100 796.90		-0.34	0.00056	P(4)	100 627.41			-0.00085
R(5)					Q(5)	100 576.98		-0.06	-0.00152	P(5)	100 367.27		-0.10	-0.00280
C(v=2)														
R(0)	103 201.94		-0.19	0.01381										
R(1)	103 196.68		0.73	0.01402	Q(1)	103 112.24		0.50	0.01286					
R(2)	103 140.20		-0.40	0.01685	Q(2)	103 017.84		-0.88	0.01177	P(2)	102 934.86		0.18	0.01111
R(3)	103 056.65		-0.04	0.01532	Q(3)	102 877.20		-0.12	0.01030	P(3)	102 753.58			0.00960
R(4)	102 909.43		-0.65	0.01139	Q(4)	102 691.29		-0.21	0.00859	P(4)	102 524.13		-0.09	0.01111
R(5)	102 719.69		-0.12	0.00928	Q(5)	102 461.51			0.00645	P(5)	102 271.56			0.00823

continue on the next page

This work		Δ^{L}	Δ^{D}	K_i	This work		Δ^{L}	Δ^{D}	K_i	This work		Δ^{L}	Δ^{D}	K_i
C(v=3)														
R(0)	105 018.45		-0.58	0.02434										
R(1)	105 010.26		-0.36	0.02186	Q(1)	104 925.58		-1.13	0.01987					
R(2)	104 953.13		-0.50	0.02055	Q(2)	104 827.24			0.01875	P(2)	104 751.40			0.02171
R(3)	104 847.31		-0.38	0.01914	Q(3)	104 680.69		-0.01	0.01722	P(3)	104 567.18		-0.27	0.01755
R(4)	104 693.38		-0.32	0.01765	Q(4)	104 487.03		-0.23	0.01544	P(4)	104 337.10		-0.06	0.01493
R(5)	104 492.03		-0.05	0.01585	Q(5)	104 247.40		-0.13	0.01320	P(5)	104 062.30		-0.10	0.01221
C(v=4)														
R(0)	106 731.61		0.02	0.02667										
R(1)	106 719.94		0.10	0.02656	Q(1)	106 641.22		0.17	0.02573					
R(2)	106 657.23		0.05	0.02582	Q(2)	106 539.02		0.14	0.02459	P(2)	106 464.53		0.38	0.02408
R(3)	106 543.53		0.10	0.02462	Q(3)	106 386.60		0.08	0.02299	P(3)	106 276.79		0.04	0.02234
R(4)	106 379.16		0.24	0.02331	Q(4)	106 185.13		0.44	0.02119	P(4)	106 041.10			0.02032
R(5)					Q(5)	105 935.89		0.36	0.01886	P(5)	105 758.51		0.29	0.01784
C(v=5)														
R(0)	108 349.85		0.26	0.03148										
R(1)	108 333.86		0.33	0.03126	Q(1)	108 259.75		0.29	0.03056					
R(2)	108 264.59		0.41	0.03053	Q(2)	108 153.69		0.37	0.02940	P(2)	108 082.75		0.49	0.02895
R(3)	108 141.72			0.02948	Q(3)	107 995.45		0.44	0.02775	P(3)	107 890.75		0.49	0.02712
R(4)	107 961.79		0.68	0.02978	Q(4)	107 786.23		0.40	0.02586	P(4)	107 648.46		0.43	0.02514
R(5)	107 686.60		0.60	0.03137	Q(5)	107 527.48		0.47	0.02346					
C(v=6)														
R(0)	109 871.21		0.15	0.03528										
R(1)	109 850.40		0.11	0.03512	Q(1)	109 781.47		0.11	0.03441					
R(2)	109 772.96		0.11	0.03488	Q(2)	109 671.44		0.10	0.03319	P(2)	109 604.16		0.29	0.03280
R(3)	109 629.39		0.25	0.03933	Q(3)	109 507.41		0.23	0.03153	P(3)				
R(4)	109 477.83		0.35	0.03378	Q(4)	109 290.46		0.22	0.02956	P(4)	109 156.85		0.36	0.02959
					Q(5)	109 021.84			0.02706					

continue on the next page

This work		Δ^{L}	Δ^{D}	K_i	This work		Δ^{L}	Δ^{D}	K_i	This work		Δ^{L}	Δ^{D}	K_i
C(v=7)														
R(0)	111 294.07			0.03868										
R(1)	111 261.05			0.04435	Q(1)	111 205.51			0.03725					
R(2)	111 199.89		0.50	0.03991	Q(2)	111 091.55		0.17	0.03602	P(2)	111 026.96		0.05	0.03623
R(3)	111 060.02		0.13	0.03637	Q(3)	110 921.59		0.50	0.03431	P(3)	110 817.86		-0.08	0.04037
R(4)	110 865.93		-0.12	0.03409	Q(4)	110 696.84		-0.03	0.03221	P(4)	110 583.77		-0.13	0.03472
					Q(5)	110 418.59		0.39	0.02964					
C(v=8)														
R(0)	112 621.21		-0.45	0.04019										
R(1)	112 594.09		0.12	0.03992	Q(1)	112 530.27		0.14	0.03911					
R(2)	112 507.62		0.16	0.03887	Q(2)	112 412.34		0.36	0.03782	P(2)	112 354.08		-0.07	0.03777
R(3)	112 362.23			0.03723	Q(3)	112 236.35		-0.06	0.03601	P(3)	112 150.94		0.02	0.03597
R(4)	112 158.17		-0.27	0.03541	Q(4)	112 003.52		-0.15	0.03388	P(4)	111 891.52		-0.19	0.03373
C(v=9)														
R(0)														
R(1)	113 811.18		0.01	0.04040	Q(1)	113 753.07		0.11	0.03993					
R(2)					Q(2)	113 630.93		-0.14	0.03860	P(2)				
R(3)	113 563.36			0.03782	Q(3)	113 448.76		0.52	0.03674	P(3)	113 368.09		0.18	0.03650
R(4)	113 346.81		0.34	0.03632	Q(4)	113 207.64		0.25	0.03451	P(4)				
C(v=10)														
R(0)	114 959.56		-0.25	0.04045										
R(1)	114 922.83		0.15	0.04001	Q(1)	114 869.71		0.32	0.03966					
R(2)	114 822.46			0.03896	Q(2)	114 743.22		0.30	0.03829	P(2)	114 692.45		-0.01	0.03809
R(3)	114 657.07		0.08	0.03760	Q(3)	114 554.48		0.11	0.03634	P(3)	114 479.73		0.07	0.03614
R(4)					Q(4)	114 304.66		0.04	0.03397	P(4)				

with z_{abs} the overall redshift of the absorbing hydrogen cloud, λ_i^z the transition wavelength at high redshift and λ_i^0 the wavelength in the laboratory frame (zero redshift).

The K_i coefficients have previously been calculated for H_2 through semi-empirical methods [7, 8] and via first principles calculations [14]. Here we adopt the method of calculating the coefficients, by solving the Schrödinger equation for ground and excited states using *ab initio* potentials to derive level energies and transition wavelengths. The sensitivity coefficient for a given line is calculated as the derivative of its wavelength or of its wavenumber with respect to the mass ratio μ. Thus, the first step is to calculate energies of the upper levels of transitions belonging to excited electronic states and energies of lower levels belonging to the ground electronic state. These energy levels are obtained by solving the Schrödinger equation of the ro-vibrational motion in a given electronic state. The second step is to calculate wavenumbers as differences between level energies, then to derive wavelengths of transitions. These steps in the calculations are repeated for several values of the mass ratio μ chosen to be close to the mass ratio of the present epoch. The results allow the determination of the derivative of the wavelength of a given line with respect to μ. At present the proton-to-electron mass ratio measured by Mohr *et al.* [49] with a relative accuracy of 2×10^{-9} is equal to $\mu_0 = 1836.15267247(80)$. This value was taken as the central value for determining the K_i.

Calculation of level energies

In the present case, the wavelengths of interest are those of electronic transitions between ro-vibrational levels of the $B^1\Sigma_u^+$, $C^1\Pi_u$, $B'^1\Sigma_u^+$, $D^1\Pi_u$ excited states and of the ground electronic state $X^1\Sigma_g^+$. The four excited states B, B', C and D states are well known to be strongly coupled and it is necessary to go beyond the adiabatic approximation. The principle of the present level calculations is similar to the one described in the study of the D_2 VUV emission spectrum [20]. Using high accuracy *ab initio* adiabatic potentials and taking into account the radial couplings between the B and $B'^1\Sigma_u^+$ states and between the C and $D^1\Pi_u$ states, as well as the $(\Sigma^+ - \Pi^+)$ rotational couplings, we performed calculations of energies of the upper bound levels belonging to these states, by solving a system of four radial coupled equations, given in matrix form as :

$$\{-\frac{1}{2\mu_n}[\mathbf{I}\frac{d^2}{dR^2} - \mathbf{I}\frac{J'(J'+1)}{R^2} + \mathbf{A}(R) + 2\mathbf{B}(R)\frac{d}{dR}] + \mathbf{U}(R) - E\}\,\boldsymbol{\varphi}(R) = 0 \quad (3.4)$$

where μ_n is the reduced mass of the HD nuclei given by:

$$\mu_{HD} = \frac{m_p \times m_D}{m_D + m_p} \quad (3.5)$$

and m_D is the deuterium nucleus mass. In atomic units, the mass unit is m_e, then the proton-to-electron mass ratio μ is numerically equal to m_p in atomic

units used in our calculations. $\mathbf{I}$ is the identity matrix and $\mathbf{U}(R)$ is the diagonal matrix of adiabatic potential curves. The diagonal elements of the $A(R)$ matrix are the adiabatic corrections, whereas the off-diagonal elements involve both nonadiabatic couplings between states of the same symmetry ($\Sigma-\Sigma$ or $\Pi-\Pi$) and the rotational couplings between $\Sigma-\Pi$ states, and finally $B(R)$ is the radial coupling matrix. More details for the formalism are described by Senn *et al.* [24]. The potential energy curves and relevant parameters for the excited states were taken from the work of Wolniewicz and co-workers [21–23].

$\boldsymbol{\varphi}(R)$ is the eigenvector matrix containing the expansion coefficients $\varphi_i(R)$ of the total ro-vibrational wave function of the molecule in the adiabatic basis of the electron-rotational wave functions. In the present case, the nonadiabatic wave function $\varphi_i(R)$ is a four-component vector :

$$\varphi_i(R) = \{\varphi_{n,i}(R), \varphi_{n',i}(R)...\}. \tag{3.6}$$

The label n refers to the particular electronic state belonging to $\{B, B^{'}, C, D\}$, and the label i is an ordering index according to increasing energies.

It is convenient to transform the coupled equations by a unitary transformation which makes the first derivative radial coupling vanish. In the transformed equations, written in the so-called diabatic representation, the matrix of the Hamiltonian has diagonal elements given by diabatic potentials, which may cross even between states of same symmetry, and off-diagonal elements given by electronic couplings between the diabatic states with no radial derivatives. We used, in the present study, the Fourier Grid Hamiltonian (FGH) method [24], an efficient and accurate method for bound state problems, to solve the coupled equations, as well as the one-state Schrödinger equation (see below eq.3.9). The advantage of this method is to provide all the energy values and the coupled-channel wave functions in one single diagonalisation of the Hamiltonian matrix expressed in a discrete variable representation (DVR). As the rotational interaction only affects the Σ^+ and Π^+ states, a system of coupled equations without rotational coupling has to be solved for the Π^- component. After solving the diabatic coupled equations, the solutions were transformed back to the adiabatic representation for the four-component $\varphi_i(R)$. The percentage of the electronic character n is obtained by :

$$\rho_i(n) = \int [\varphi_{n,i}(R)]^2 \mathrm{d}R \tag{3.7}$$

with the normalization : $\rho_i(B) + \rho_i(C) + \rho_i(B') + \rho_i(D) = 1$.
The electronic component $\varphi_{n,i}(R)$ takes into account not only the bound vibrational states but also the vibrational continuum. The percentage corresponding to a particular vibrational state v_n of the electronic state n can be obtained by expanding over a set of vibrational functions $\varphi_{n,v}(R)$, solutions of the uncoupled equation for adiabatic state n :

$$\rho_i(n,v) = \left| \int \varphi_{n,v}(R)\varphi_{n,i}(R)\mathrm{d}R \right|^2. \tag{3.8}$$

The $X^1\Sigma_g^+$ ground state [26] is isolated from the other excited states, therefore its vibrational energy levels were calculated by solving one Schrödinger equation (eq 3.9) for each rotational quantum number J'' in the adiabatic approximation adding the corresponding centrifugal term to the *ab initio* potential $U_x(R)$, which includes the adiabatic correction into the Born-Oppenheimer potential, computed by Wolniewicz [26]. The relativistic and the radiative corrections [25] were also taken into account in the present calculations.

$$\{-\frac{1}{2\mu_n}\frac{d^2}{dR^2} + \frac{J''(J''+1)}{2\mu_n R^2} + U_x(R) - E_x\}\,\varphi_x(R) = 0. \tag{3.9}$$

The weak effect of excited states of the symmetries $\Sigma_{g(u)}$ and $\Pi_{g(u)}$, which leads to the regular nonadiabatic shifts ΔE_x of the levels of the ground state $X^1\Sigma_g^+$, was taken into account by means of the semi-empirical relations [27]:

$$\Delta E_x = E_{\Sigma_g} + E_{\Sigma_u} + J''(J''+1)(E_{\Pi_g} + E_{\Pi_u}) \tag{3.10}$$

where:

$$E_{\Sigma_{g(u)}} = \frac{\langle\varphi_x|E_x^{ad} - V_x(R)|\varphi_x\rangle}{\mu_n}\sum_i a_i(\Pi_{g(u)})\eta^i \tag{3.11}$$

$$E_{\Pi_g} = \frac{1}{\mu_n^2}\sum_i b_i(\Pi_g)\eta^i \tag{3.12}$$

$$E_{\Pi_g} = \frac{1}{\mu_\alpha^2}\sum_i b_i(\Pi_u)\eta^i \tag{3.13}$$

where μ_α is the difference of mass of the deuterium nucleus and the hydrogen nucleus given by: $\mu_\alpha = (m_D + m_p)/(m_D - m_p)$. η is the mass-dependent quantum number given by: $\eta = (v_x + \frac{1}{2})/\sqrt{\mu_n}$. The energies $E_{\Sigma_{g(u)}}$ and $E_{\Pi_{g(u)}}$ belong, respectively, to the electronic states $\Sigma_{g(u)}$ and $\Pi_{g(u)}$. φ_x represents the ro-vibrational wave function associated to the energy E_x. $V_x(R)$ is the adiabatic energy potential of the ground state X including the centrifugal barrier. Here, the mass-independent coefficients a_i and b_i of the polynomial expansions were determined from the experimental energy levels for homonuclear isotopologues H_2, D_2, and T_2.

Similar calculations of the level energies were reported by Abgrall and Roueff [50] using the same *ab initio* data but different method to solve the Schrödinger equation. As previously mentioned we used the the Fourier Grid Hamiltonian method, based on a Discrete Variable Representation (DVR) of the wavefunctions and of the Hamiltonian, while Abgrall and Roueff used the Numerov method. Our four-state calculations led to the same energies as

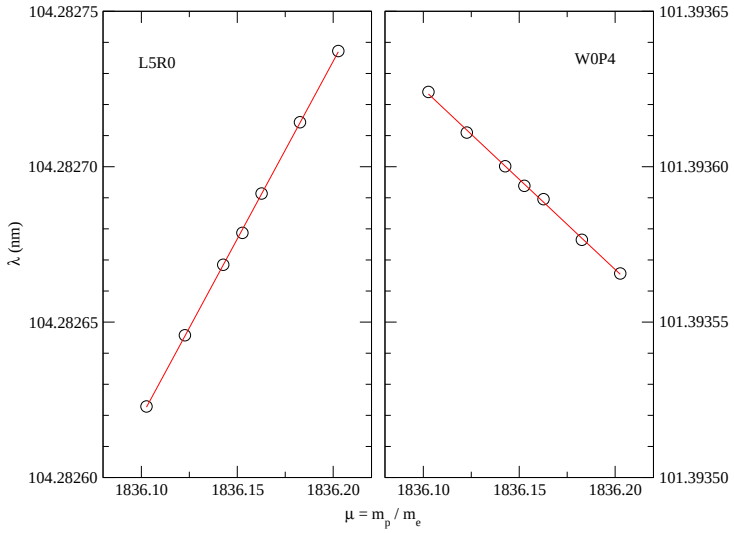

Figure 3.4: The wavelengths of the $B^1\Sigma_u^+\,(v=5) \leftarrow X^1\Sigma_g^+\,(v=0)$ R0 and $C^1\Pi^+\,(v=0) \leftarrow X^1\Sigma_g^+(v=0)$ P4 transitions were deduced using calculations based on *ab initio* adiabatic potentials for seven different values of the proton-to-electron mass ratio around the presently known value. The sensitivity coefficients K_i are deduced from the slope of the linear regression of these points.

reported in [50] for all levels involved in the current study, with largest discrepancy being ± 0.01 cm^{-1} for some high vibrational levels.

It must be noted that the full effect of *ungerade - gerade* symmetry breaking in HD is not accounted for. There exist specific levels that undergo a *u-g* interaction between $B^1\Sigma_u^+$ and $C^1\Pi_u$ states on the one hand and $EF^1\Sigma_g^+$ states on the other hand (with a selection rule $\Delta J = 0$) giving rise to perturbations and level mixings. These effects are not included in our close coupling calculations because only incomplete *ab initio* coupling operators are available [29]. In order to estimate this effect a tentative calculation was performed for the example of the $B-X(25,0)$ R(3), one of the most strongly affected lines. This yields a shift of 5.11 cm^{-1} and an increase in the sensitivity coefficient by approximately 7% induced by the EF coupling. An extended analysis of this *u-g* symmetry-breaking effect will be the subject of a future study.

Determination of $d\lambda_i/d\mu$

From the level energies calculated above, the wavelengths of transitions can be deduced. The entire procedure described has to be performed for several values of the reduced mass of nuclei μ_n, involving several values of the proton-to-electron mass ratio μ chosen to be close to μ_0. In these conditions, the

variation of a given wavelength λ_i versus μ is close to linear and its slope represents the derivative $d\lambda_i/d\mu$.

In the previous investigations [8] on a possible variation of μ, the statistical analysis of the recent observations of spectroscopic features in cold hydrogen clouds in the line of sight of two quasar light sources (Q 0405-443 and Q 0347-383), based on highly accurate laboratory wavelength measurements of H_2 lines, led to an order of magnitude of 2×10^{-5} for $\Delta\mu/\mu$ over 12 Gyears. This sets the scale to deduce a value of the derivative $d\lambda_i/d\mu$; the variation step of μ should be chosen to obtain a few points within this interval. In our case the calculations have been performed for the present value of $\mu_0 = 1836.15267261$ and another six values of μ separated by 0.02 and spanning from $\mu = 1836.10267261$ to $\mu = 1836.20267261$.

$R(J)$, $P(J)$ and $Q(J)$ transitions were calculated for each of the values of μ mentioned above. Then for each transition, the variation of wavelength versus μ was plotted and its slope was calculated by a linear fit. The fit provides, together with the slope, the uncertainty of its determination, the standard deviation of the fit and finally the χ^2 value. In Fig.4 we show two examples of the variation in wavelength of $B^1\Sigma_u^+(v = 5) \leftarrow X^1\Sigma_g^+(v = 0)$ R(0) and $C^1\Pi_u(v = 0) \leftarrow X^1\Sigma_g^+(v = 0)$ P(4) transitions due to variation in μ , as well as their linear fits.

The values of the K_i coefficients and their uncertainties were then deduced from the calculated values of the slopes and their uncertainties using Eq. 3.2. For completeness sensitivity coefficients were calculated for all experimentally observed lines, even for those beyond the Lyman-cutoff at $\lambda < 91$ nm in which domain the molecular hydrogen lines cannot be observed under the usual astrophysical conditions of a high density of H I. The values for the resulting K_i coefficients are listed in Tables 3.1 and 3.2 with the molecular transition frequencies.

The range of values for the K_i-coefficients for the HD lines observable in high-redshifted objects lie in the range -0.01 to 0.05, similarly as in H_2. These values are small, *i.e.* much smaller than for the proposed experiments involving detection schemes of μ variation on a laboratory time scale [51,52]. This is due to the fact that the Lyman and Werner lines are electronic transitions, while the electronic energy in molecules is nearly mass-independent (in so far as the Born-Oppenheimer approximation holds). In the comparison with high-redshift H_2 and HD lines the sensitivity for detection of μ variation comes from the extremely large intervals of $\sim 10^{10}$ years. The here presented K_i coefficients for HD were in fact already used in the treatment of data in the J2123 quasar object at redshift $z = 2.05$ [36].

3.5 Conclusions

We report on a Fourier transform spectroscopic study of HD in the VUV spectral domain at $\lambda = 87 - 112$ nm. Some 268 transitions in the $B^1\Sigma_u^+ (v' = 0 - 30) \leftarrow X^1\Sigma_g^+ (v'' = 0)$ Lyman bands and 141 transitions in the $C^1\Pi_u (v' = 0 - 10) \leftarrow X^1\Sigma_g^+ (v'' = 0)$ Werner bands were deduced from a quasi static gas sample using a novel VUV Fourier transform spectrometer at the Soleil Synchrotron facility. The estimated accuracies of the wavelength calibration is 0.04 cm^{-1}, which is verified by ground state combination differences. Accuracies of $\Delta\lambda/\lambda \sim 4 \times 10^{-7}$ match the accuracies as typically obtained in high redshift observations of the same molecular lines. The calculated sensitivity coefficients make the data relevant for the investigations of possible variation of the fundamental constants on a cosmological time scale.

3.6 Acknowledgments

The authors acknowledge fruitful discussions with Dr. M. Vervloet and Dr. D. Bailly. The staff of SOLEIL is thanked for the support and for providing the opportunity to conduct measurements in campaigns in 2008 and 2009. The work was supported by the Netherlands Foundation for Fundamental Research of Matter (FOM). We are indebted to EU for its financial support via the Transnational Access funding scheme.

Chapter 4

Frequency calibration of B $^1\Sigma_u^+$ - X $^1\Sigma_g^+$ (6,0) Lyman transitions in H_2 for comparison with quasar data

Abstract

The Lyman and Werner spectroscopic transitions of molecular hydrogen, the most ubiquitous molecular spectral lines observed in the Universe, provide a tool to probe a possible variation of the proton-to-electron mass ratio μ on a cosmological time scale. Such procedures require a database of zero-redshift, or laboratory-based wavelengths at the highest possible level of accuracy. Accurate transitions in the B $^1\Sigma_u^+$ - X $^1\Sigma_g^+$ (6,0) Lyman band of H_2 are still missing in the set of laboratory data, due to previously encountered problems in generating the appropriate wavelengths using a narrow-band extreme ultraviolet laser source. Here frequency calibrations of the missing transitions are presented from a laser-based study at a $(5-8)\times10^{-8}$ accuracy level.

4.1 Introduction

The issue of a possible variation of fundamental constants on a cosmological time scale has become a key query in modern physics. Besides detection of a variation of the fine structure constant α [53], the focus is now also on a possible variation of another dimensionless quantity, the proton-to-electron mass ratio $\mu = m_p/m_e$, in particular because it is hypothesized that the variation of μ should be larger than that of α [54]. Deductions on μ-variation relate to the absorption spectrum of the ubiquitous Lyman and Werner bands of the hydrogen molecule, the most abundant molecular species in the Universe. Since the underlying concept was put forward by Thompson [2], and Varshalovich

and Levshakov reported a first constraint on a variation of μ from H_2 spectroscopic comparisons over a range of redshifts [55], this subject has attracted much attention, especially after accurate laboratory frequencies of the prominent Lyman and Werner transitions have become available [15, 16, 56]. Ubachs and coworkers reported an indicative decrease of μ by 0.002% over a timespan of the past 12 Gyrs [7], based on a comparison between accurate laboratory data and 76 quasar H_2 spectral absorption features occurring in Q 0405-443 and Q 0347-383 at high redshift. However, in the database of accurately calibrated rest-frame frequencies a number of transitions were missing, in particular in the B $^1\Sigma_u^+$ - X $^1\Sigma_g^+$ (6,0) Lyman band. In previous measurement campaigns difficulties were encountered in the narrow-band pulsed dye amplification system to generate wavelengths in the range 616 - 621 nm, the fundamental wavelengths required to generate the XUV-radiation at 102.5 - 103.5 nm for excitation of the B $^1\Sigma_u^+$ ($v' = 6$) state in H_2. The experimental difficulties have been resolved through the use of special solvent mixtures for the dyes used in the laser amplifier chain. This made it possible to measure accurate transition frequencies in the (6,0) band, which now complement the database of accurate laboratory frequencies of molecular hydrogen, which may be used in future comparisons with highly-redshifted H_2 transitions to extract information on possible variations of μ.

4.2 Experiment

The experimental setup is described in previous publications [56–58] and is only summarized briefly here. The tunable narrow bandwidth continuous wave output of a Spectra Physics 380 D Ring Dye Laser is used to seed a three-stage Pulsed Dye Amplifier (PDA) producing nearly Fourier-transform limited laser pulses of 5 ns duration. The alignment procedures for the ring dye laser and the PDA are decoupled through the use of an optical fiber, allowing for high spatial stability of the seed beam. The ring laser was routinely operated in the range 616 - 621 nm by using Rhodamine B dye dissolved in glycol. As discussed in the comprehensive study by Philip *et al.* [56], problems were encountered in the production of powerful laser pulses at wavelengths upward of 615 nm. This prohibited the production of corresponding wavelengths near 103 nm required for the excitation of B $^1\Sigma_u^+$ ($v' = 6$) levels in molecular hydrogen. Only three transitions originating from $J'' = 0$ and $J'' = 1$ could be observed previously at a low signal-to-noise ratio.

For the purpose of the present study we have carefully examined the operation of the PDA, while using several dyes and solvents. Optimum operation in the desired range was accomplished by using Sulforhodamine 101 dye in a solvent mixture of 60%-40% (volume) methanol and water. This way pulse energies of approximately 140 mJ could be obtained in the range 616 - 621 nm. The procedures to convert the Fourier-transform limited laser pulses from

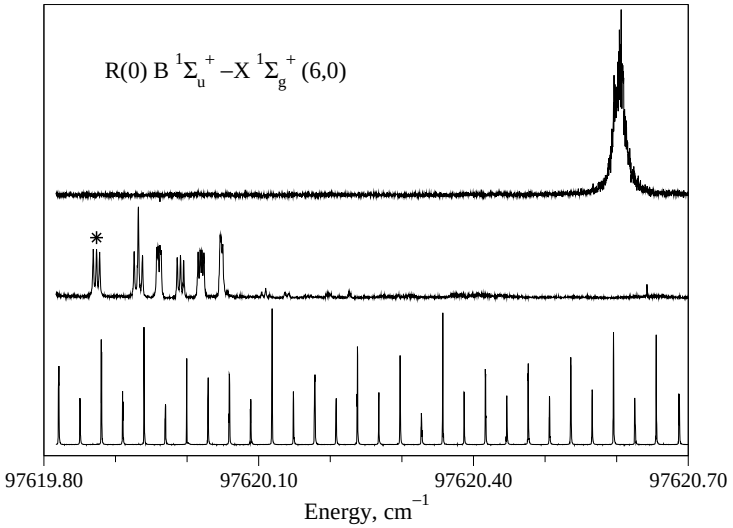

Figure 4.1: Spectrum of the B $^1\Sigma_u^+$ ($v' = 6$) ← X $^1\Sigma_g^+$ ($v'' = 0$) R(0) Lyman transition in H_2 (upper trace). The line width of the measured transition is 450(25) MHz. The middle trace represents a simultaneously recorded Doppler-free calibration spectrum in molecular iodine; the R(101) (11-3) transition with the "t"-component at 16 269.978 92 cm^{-1} is marked with (*). The lower trace represents a transmission spectrum of a frequency-stabilized étalon.

the PDA to UV pulses (using a KD*P crystal) and then to XUV pulses (via harmonic generation in a gas jet of xenon) are similar to those discussed previously [56–58].

The overlapping XUV and UV beams are crossed perpendicularly with a pulsed and skimmed beam of molecular hydrogen released from a pulsed nozzle (General Valve Series 9) with a stagnation pressure of approximately 2 bar. The nozzle is positioned 8 cm from the skimmer and 18 cm from the interaction region. The ions created by 1+1′ Resonance Enhanced Multiphoton Ionization (REMPI) are extracted by a pulsed electric field in a direction perpendicular to the plane formed by the laser and the molecular beams and detected with an electron multiplier. This time-of-flight (TOF) technique allows for mass identification of the ions and distinction against those arising from to the background oil in the vacuum system. Moreover, the extraction field is switched on 0.2 μs after the laser pulse, ensuring field-free excitation. Absolute frequency calibration of the seeding light is derived by performing saturation spectroscopy of I_2 and recording the transmission fringes of an actively stabilized étalon (FSR ≈ 150 MHz). The integrated ion signal and the calibration signals are simultaneously read out by a computer. A typical spectrum recorded in this manner is shown in Figure 4.1. The upper trace shows the spectrum of the the B $^1\Sigma^+$

($v' = 6$, $J' = 1$) $\leftarrow$ X $^1\Sigma^+$ ($v'' = 0$, $J'' = 0$) transition in H_2. The lower two traces represent the calibration spectra consisting of a Doppler-free absorption spectrum of molecular iodine (B-X system) and a transmission spectrum of the étalon.

Special attention is paid to Doppler shift effects as they contribute significantly to the experimental error budget. The velocity distribution in the molecular beam expansion can be monitored by varying the time delay of the gas pulse with respect to the laser pulse. By iterative comparison of the spectra arising from the early and late arrival parts of the molecular pulse, the angular position of the nozzle can be precisely adjusted: the position of near-zero Doppler shift is at the location where the transition frequency does not depend on the velocity in the beam. Also a separate experiment is performed to determine and further minimize the residual Doppler shift. The measured spectra of the H_2 are compared to the spectra obtained for a seeded H_2 in Kr. Since the Kr is much heavier the velocity of the mixture is substantially lower. The observed transition frequency difference in the two cases was insignificant proving a Doppler-free alignment. Translated into frequency, we claim these two methods give a maximum uncertainty due to the Doppler effect of 100 MHz in the error budget estimation. The actual spectroscopic measurements are carried out by probing the slower molecules at the rear end of the pulse, thus allowing for a smaller remaining Doppler shift. Under these condition the linewidths are also the narrowest.

The largest contribution to the uncertainty budget arises from the effect of frequency chirp in the dye amplifiers, which may result in a net shift between the center frequency of the XUV beam used for exciting the H_2 transitions, and the fundamental frequency in the CW seed beam (multiplied by a factor of 6 for harmonic conversion), which is, in fact, calibrated. This chirp phenomenon was quantitatively and experimentally addressed by Eikema *et al.* [57] in a

Table 4.1: Effects contributing to the error and their estimated values.

source	σ [a] (MHz)
Doppler uncertainty	60−100
AC Stark shift	30−50
chirp shift	100−150
I_2 calibration	10
étalon drift	2
statistics	50
resulting uncertainty[b]	130−195

[a] σ stands for standard deviation.
[b] Calculated from the quadrative sum of all contributions.

detailed study of a single spectral line. In the work of Philip *et al.* [56] on a vast number of spectral lines in H_2 resulting uncertainties from the chirp effect were estimated, based on the general findings in Ref. [57] and included in the uncertainty budget. We have adopted this procedure as well, but we note that in cases where spectral measurements are performed at the short and long wavelength ends of the gain curve of a specific dye solution, the chirp-induced offsets may increase [62]. This is the case for the lines at the long wavelength side of the studied region, in particular for the R(4) and P(4) lines in the (6,0) band. Whereas in Ref. [56] the chirp-induced shifts were estimated to be limited to 100 MHz, we conservatively estimate here an upper bound of 150 MHz in some cases. The comprehensive uncertainty budget is presented in Table 4.1.

4.3 Results

The spectroscopic results for nine rotational transitions in the B $^1\Sigma_u^+$ ($v' = 6$) $\leftarrow$ X $^1\Sigma_g^+$ ($v'' = 0$) Lyman band in H_2 are summarized in Table 4.2. These transitions were measured and calibrated to accuracies in the range $0.005 - 0.008$ cm^{-1}. Three of them were previously calibrated by Philip *et al.* [56], and in comparison the present values are lower by 0.007 on average, which represents a systematic shift at the level of 1σ in terms of the present uncertainties. The present results are also compared to the values given in the table of the

Table 4.2: Transition energies(in cm^{-1}) of the Lyman bands in H_2 for $v' = 6$ with uncertainties given in parentheses ($1\,\sigma$). For convenience of use in astrophysical comparisons the wavelengths of the spectral lines are also listed (in nm). The values in the last three columns represent previously reported results.

Line	this work (nm)	this work (cm^{-1})	Ref. [56] (cm^{-1})	Ref. [59][a] (cm^{-1})	Ref. [60][b] (cm^{-1})
P(1)	102.593534(6)	97 472.029(6)	97 472.046(8)	97 472.12	97 472.13(10)
P(2)	102.810598(6)	97 266.237(6)	-	97 266.27	97 266.28(10)
P(3)	103.119284(7)	96 975.073(7)	-	96 975.14	96 975.18(10)
P(4)	103.518295(9)	96 601.282(8)	-	96 601.42	96 601.32(10)
R(0)	102.437386(5)	97 620.609(5)	97 620.600(8)	97 620.29	97 620.65(10)
R(1)	102.498804(6)	97 562.114(6)	97 562.127(8)	97 562.25	97 562.21(10)
R(2)	102.652844(5)	97 415.713(5)	-	97 415.90	97 415.75(10)
R(3)	102.898676(6)	97 182.980(6)	-	97 183.32	97 183.09(10)
R(4)	103.235111(7)	96 866.268(7)	-	96 865.97	96 866.28(10)

[a] Transitions of B $^1\Sigma_u^+$ - X $^1\Sigma_g^+$ (6,0) Lyman band as reported by Abgrall *et al.* in the atlas of Ref. [59]

[b] Calculated using combinations of level energies for the excited states as given in Ref. [60] (table VI) and ground state level energies reported in Ref. [61]. The specified uncertainties are less than 0.1 cm^{-1}.

Table 4.3: Comparison of the difference frequencies of $R(J'') - P(J''+2)$ for $J'' = 0, 1, 2$ of the Lyman transitions in H_2 for $v' = 6$ (see Table 4.2) and the $S(J'')$ transitions in the X $^1\Sigma_g^+$ ground state of H_2 (see Ref. [61] table I).

J''	$R(J'') - P(J''+2)$ (cm^{-1}) this work	$S(J'')$ (cm^{-1}) Ref. [61]
0	354.372(8)	354.3733(2)
1	587.041(10)	587.0324(2)
2	814.431(10)	814.4246(3)

Lyman band system of molecular hydrogen [59]. However, by making use of the B $^1\Sigma_u^+$ level energies determined from the comprehensive classical spectroscopy carried out in the Meudon Observatory [60], combined with the accurate level energies in the X $^1\Sigma_g^+$ ($v'' = 0$) ground state [61], an improved accuracy is established. The transition frequencies of the Lyman lines in the resulting classical database are considered to be accurate to 0.1 cm^{-1}. The present results are on average shifted by -0.06 cm^{-1} from these values, which is within the estimated uncertainty of the Meudon data set.

In Table 4.3, the combination differences $R(J'') - P(J''+2)$ for $J'' = 0, 1, 2$ of the B $^1\Sigma_u^+$ ($v' = 6$) $\leftarrow$ X $^1\Sigma_g^+$ ($v'' = 0$) Lyman transitions are compared with the corresponding $S(J'')$ transitions in the X $^1\Sigma_g^+$ ground state of H_2. The values are consistent with the literature values of Jennings *et al.* [61]. This result provides an independent validation of the calibration procedures followed in the present study.

The presently obtained highly accurate transition frequencies were included in the database of zero-redshift Lyman transitions, thereby replacing some older and less accurate values. In particular, no previous laser-based calibrations were available for the R(2) and R(3) transition, which were observed in quasar spectra at high redshift. The fit comparing the 76 high-redshift H_2 lines in the Q 0405-443 and Q 0347-383 quasar systems was reevaluated and produces a value for the variation of the proton-to-electron mass ratio of $\Delta\mu/\mu = (2.40 \pm 0.60) \times 10^{-5}$, fully consistent with the previously reported value [8].

4.4 Conclusions

We present new accurate frequency calibrations of nine rotational lines in the B-X (6,0) Lyman band in H_2 at accuracies in the range $0.005 - 0.008$ cm^{-1}. These measurements fill an important gap in the recently published data set on the hydrogen Lyman and Werner bands for comparison with quasar data and for extracting possible variations of the proton-to-electron mass ratio on a cosmological time scale. It is particularly in this realm where the relevance of

these measurements lies.

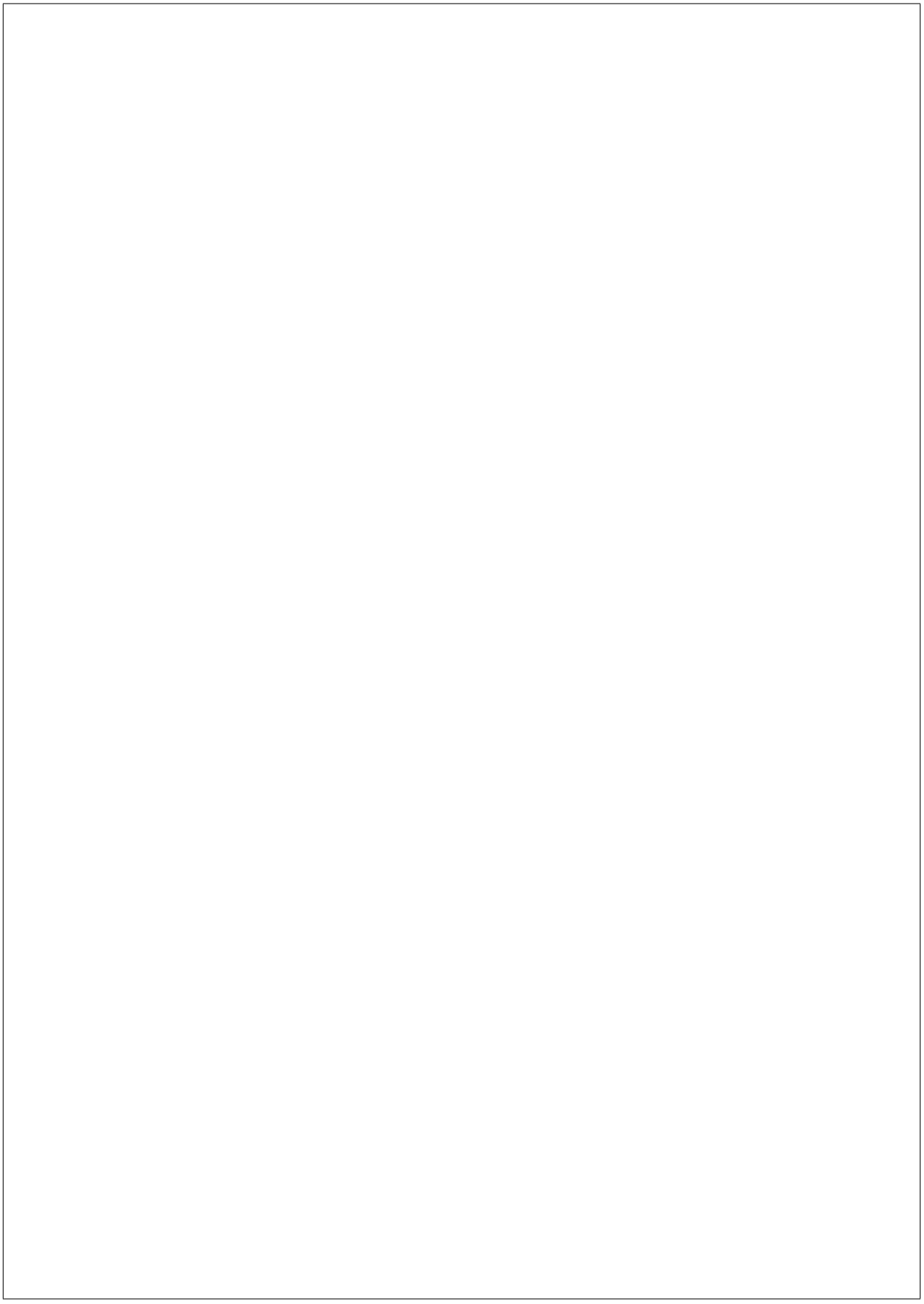

Chapter 5

Extreme ultraviolet laser calibration of D_2 Lyman and Werner transitions

Abstract

Some 39 lines in the $B^1\Sigma_u^+ \leftarrow X^1\Sigma_g^+(v',0)$ Lyman bands for $v' = 9-11$, and in the $C^1\Pi_u \leftarrow X^1\Sigma_g^+(0,0)$ Werner band of the D_2 molecule were measured using a narrowband tunable extreme-ultraviolet laser source, at an unprecedented accuracy of $\Delta\lambda/\lambda = 6 \times 10^{-8}$. The results bear relevance for future use in the calibration of dense classical spectra obtained for the HD and D_2 hydrogen isotopologues.

5.1 Introduction

The hydrogen molecule is a benchmark system for the investigation of molecular structure. Notwithstanding the fact that it is the smallest neutral molecule, its spectrum is complex: H_2 and its natural isotopologues HD and D_2 do not exhibit band structures normally associated with molecules in the gas phase, but rather atomic-like spectra without obvious regularities. Moreover, due to the low nuclear masses application of the Born-Oppenheimer approximation become somewhat questionable. Hence, adiabatic and non-adiabatic effects on the level structure are most pronounced in hydrogen, thus making the hydrogen molecule an ideal testing ground for assessing mass-dependent effects in spectra of diatomic molecules. Finally, due to the large energetic separation between $1s$ and $2p$ levels in the H-atom, and the large binding energy of the singly-bonded ground state of the hydrogen molecule, the electronic absorption and emission spectra of H_2 and its isotopologues are in the vacuum ultraviolet (VUV) domain, which for many years has been difficult to access with high-resolution methods. A detailed understanding of the hydrogen VUV-spectra is important in astrophysics due to the large abundance of hydrogen, with the

strongest absorption features formed by the Lyman and Werner band systems of H_2 and HD. D_2 is of relevance for plasma science, most notably in Tokamak environments aiming at deuterium nuclear fusion.

Over the years the VUV spectrum of D_2 has been investigated by a number of spectroscopists, namely, Bredohl and Herzberg [63], Dabrowski and Herzberg [64], Takezawa and Tanaka [65], and Larzilliere *et al.* [66], all in connecting wavelength regions. Hinnen *et al.* [67] thereupon performed a study of a limited part of the D_2 spectrum using a tunable laser source in the vacuum ultraviolet at a somewhat better resolution than in the classical spectroscopic studies.

At the Meudon Observatoire in the last decade techniques of high-resolution grating spectroscopy have been applied to produce a comprehensive database on the VUV emission spectrum of hydrogen, culminating in an atlas for H_2 [68]. Work is in progress to extend these studies to HD and D_2. Before the HD lines can be assigned, the D_2 spectrum has to be investigated, because an HD emission discharge spectrum will always be contaminated by H_2 and D_2 transitions. Recently investigations on the $D^1\Pi_u \rightarrow X^1\Sigma_g^+$, $D'^1\Pi_u \rightarrow X^1\Sigma_g^+$ [20] and the $B'^1\Sigma_u^+ \rightarrow X^1\Sigma_g^+$ systems [69] have been published. In such studies several thousand spectral lines are recorded. An internal calibration standard for such comprehensive spectra may be provided by accurately calibrated wavelength positions for a limited subset. This is precisely the purpose of the present laser-based investigation of D_2; some 39 D_2 lines in the wavelength range $99.98 - 102.07$ nm have been calibrated with an accuracy of $\Delta\lambda/\lambda = 6 \times 10^{-8}$. These transitions may serve as a calibration standard in the ongoing emission studies on the $B^1\Sigma_u^+ \rightarrow X^1\Sigma_g^+$ Lyman and $C^1\Pi_u \rightarrow X^1\Sigma_g^+$ Werner band systems in D_2.

5.2 Experiments

The methods of performing high-resolution spectroscopy with a narrowband tunable extreme-ultraviolet (XUV) laser source on diatomic molecules in a pulsed and skimmed molecular beam have been developed at the Laser Center (Vrije Universiteit, Amsterdam) and described previously [58]. Coherent XUV-radiation is produced by harmonic upconversion of the output of a pulsed dye amplifier, which is injection seeded by a stabilized ring-dye laser. The visible output in pulses of 5 ns duration is frequency-doubled in a KD*P-crystal and thereupon tripled in a xenon gas jet. The pulsed XUV-radiation of nearly Fourier-transform limited bandwidth ($\Delta\nu \sim 250$ MHz) then perpendicularly intersects a molecular beam of D_2. It should be noted that the XUV-radiation produced with the present laser system possesses a resolution and accuracy more than an order of magnitude better than with the system used in Ref. [67]. Possible Doppler shifts on the central resonance wavelengths are carefully addressed through probing of different velocity clusters in the beam by delaying the laser pulses with respect to the molecular beam pulses. The absolute fre-

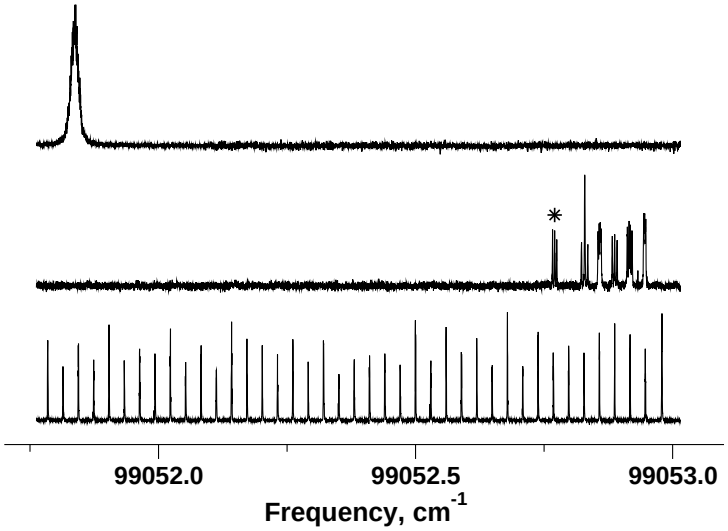

Figure 5.1: Recording of the R(3) line in the B←X (10,0) Lyman band in D_2 via 1 XUV + 1' UV ionization spectroscopy, using a narrowband laser system tunable in the XUV domain. The absolute calibration of this line is performed by comparing the visible laser radiation before harmonic conversion to the t-hyperfine component in the I_2 B←X(11,2) R(85) line, marked with (*) and corresponding to 16 508.79510 cm^{-1}.

quency calibration is derived from a reference standard in the visible range, based on saturation spectroscopy of molecular iodine [70]; interpolation is performed with the use of a stabilized étalon and the calibration in the XUV-domain is then derived from multiplication by the harmonic order. The full analysis of the uncertainty budget of the XUV-spectroscopic measurements has been discussed in recent studies performed by the group of the Laser Center, for limited sets of rotational lines of Lyman and Werner bands in H_2 and HD [15,16,56] and for the recently published work on frequency calibration of Lyman transitions in H_2 [71]. In Fig. 5.1 a typical recording of a D_2 spectral line is displayed, with the I_2 and étalon traces used for the calibration.

5.3 Results and discussion

The wavelengths of the 39 accurately determined line positions and the corresponding frequencies in wavenumber units are listed in Table 5.1. From the error budget, the uncertainty in the line positions is estimated to be $\pm 0.000\,006$ nm or ± 0.006 cm^{-1} in wavenumbers. Note that all wavelength values pertain to vacuum. Combination differences Δ_{20} between $P(J''+2)$ and $R(J'')$ lines can further be verified with ground-state rotational splittings from far-infrared

Table 5.1: Measured wavelengths and the corresponding frequencies of rotational lines belonging to the $B^1\Sigma_u^+ \leftarrow X^1\Sigma_g^+$ Lyman bands (Lv for B-X($v'-0$)) and $C^1\Pi_u \leftarrow X^1\Sigma_g^+$ Werner bands (Wv for C-X($v'-0$)) for D_2. The figures in parentheses represent the uncertainty in the last digit. Δ_{o-h} refers to the difference between the present laser-based results and the previously obtained classical values for the transition frequencies [64]. Δ_{o-c} lists the difference between the observed and calculated frequencies obtained in the present work.

Line	λ (nm)	σ (cm^{-1})	Δ_{o-h} (cm^{-1})	Δ_{o-c} (cm^{-1})
L11R0	99.950 845 (6)	100049.179 (6)	0.389*	−1.091
L11R1	99.981 898 (6)	100018.106 (6)	0.076	−1.094
L11P1	100.024 982 (7)	99975.024 (7)	0.044	−1.086
L11R2	100.058 279 (6)	99941.755 (6)	0.035	−1.095
L11P2	100.130 055 (6)	99870.114 (6)	0.004	−1.086
L11R3	100.179 786 (6)	99820.536 (6)	0.056	−1.094
L11P3	100.280 205 (6)	99720.578 (6)	0.098	−1.092
L11R4	100.346 139 (6)	99655.055 (6)	0.145	−1.105
L11P4	100.475 135 (6)	99527.112 (6)	0.002	−1.088
W0R1	100.576 139 (6)	99427.161 (6)	−0.119	−0.209
W0R0	100.578 369 (6)	99424.957 (6)	−0.023	−0.203
W0R2	100.603 099 (6)	99400.517 (6)	0.017	−0.213
W0Q1	100.639 168 (6)	99364.891 (6)	0.111	−0.199
W0R3	100.659 135 (6)	99345.181 (6)	0.101	−0.219
W0Q2	100.697 795 (7)	99307.041 (7)	−0.069	−0.199
L10R0	100.727 943 (6)	99277.318 (6)	0.250	−1.040
W0R4	100.744 037 (7)	99261.458 (7)	0.118	−0.232
L10R1	100.758 767 (7)	99246.947 (7)	0.877	−1.043
W0P2	100.759 840 (6)	99245.890 (6)	−0.190*	−0.200
W0Q3	100.785 478 (6)	99220.644 (6)	0.184	−0.206
L10P1	100.803 590 (6)	99202.816 (6)	0.116	−1.044
L10R2	100.835 265 (7)	99171.654 (7)	0.104	−1.046
W0P3	100.878 015 (6)	99129.627 (6)	0.107	−0.203
W0Q4	100.901 911 (6)	99106.151 (6)	0.161	−0.209
L10P2	100.909 950 (6)	99098.255 (6)	0.055	−1.045
L10R3	100.957 239 (6)	99051.837 (6)	0.057	−1.053
W0P4	101.024 522 (6)	98985.868 (6)	0.118	−0.212
L10P3	101.061 745 (7)	98949.409 (7)	0.189	−1.051
L10R4	101.124 405 (7)	98888.097 (7)	0.077	−1.063
L10P4	101.258 641 (6)	98757.004 (6)	0.324	−1.056
L9R0	101.533 513 (6)	98489.648 (6)	0.188	−0.992
L9R1	101.564 042 (6)	98460.044 (6)	0.124	−0.996
L9P1	101.610 783 (7)	98414.752 (7)	0.122	−0.998
L9R2	101.640 597 (6)	98385.884 (6)	0.034	−1.006
L9P2	101.718 451 (6)	98310.581 (6)	0.231	−0.999
L9R3	101.762 986 (7)	98267.557 (7)	0.157	−1.013
L9P3	101.871 885 (6)	98162.511 (6)	0.171	−0.999
L9R4	101.930 917 (6)	98105.661 (6)	0.191	−1.009
L9P4	102.070 772 (6)	97971.239 (6)	0.229	−1.001

* Blended line in Ref. [64]

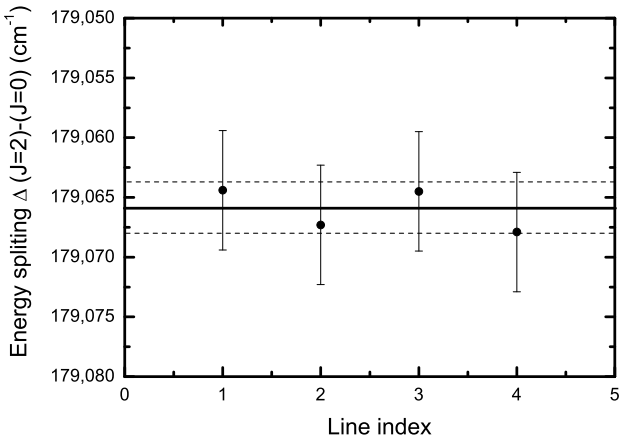

Figure 5.2: Energy splitting Δ_{20} between the $J'' = 2$ and $J'' = 0$ ground-state levels derived from combination differences between four pairs of R(0) and P(2) transitions measured in the Lyman and Werner bands. Indicated are the (weighted) average value of Δ_{20} from the four pairs and the resulting uncertainty: 179.066 (1) cm^{-1}.

FT-Raman spectroscopy [72] to test the accuracy and the internal consistency of our results. The present set of Lyman and Werner band transitions contains measurements of four pairs of R(0) and P(2) lines whose combination differences are plotted in Fig. 5.2. This shows the consistency of the set of results involving these eight spectral lines. The deviation of the combination differences from their average value is 0.002 cm^{-1}. This suggests that the determination of transition frequencies is more accurate than would follow from our estimated error budget for these pairs of transitions. A statistical analysis yields a value for the combination difference of 179.066 (1) cm^{-1}, in agreement with the IR data [72] given by 179.068 (2) cm^{-1} for the Δ_{20} energy splitting. A similar procedure can be performed for the R(1)-P(3) combination differences, where an average value of 297.533 (2) cm^{-1} is derived from a set of four pairs of transitions, in agreement with 297.533 (3) cm^{-1} given for the Δ_{31} energy splitting [72]. This result provides an independent validation of the calibration procedures followed in the present study. Note also that the present XUV results yield improved values for the ground-state combination differences.

In the spectral range $99.98 - 102.07$ nm the most accurate VUV wavelength measurements of D_2 were performed by Dabrowski and Herzberg [64], using a spectrograph with concave grating. They claimed an uncertainty of 0.15 cm^{-1} on transition energies of unblended lines. The differences between the presently observed transitions with these previously reported data, Δ_{o-h}, are

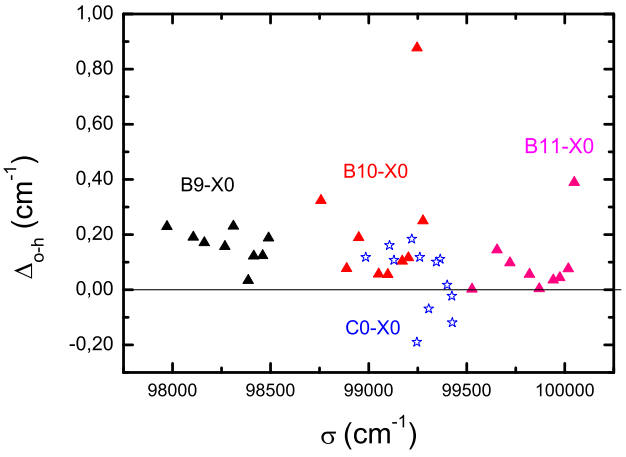

Figure 5.3: Comparison between transition frequencies obtained in the present laser-based study and those obtained from the classical work of Ref. [64].

listed in Table 5.1 and are plotted in Fig. 5.3. From this comparison, we find that the transition energies of the B($v'' = 9 - 11$) ← X(0) Lyman bands from Ref. [64] are on average lower by 0.14 cm^{-1} compared to the present laser-based results, with a standard deviation of $\sigma = 0.10$ cm^{-1}. The transition energies of C(0)←X(0) Werner band lines from Ref. [64] are on average smaller by 0.04 cm^{-1} than the laser-based results, with a standard deviation of $\sigma = 0.12$ cm^{-1}. In the work on the H_2 molecule by Philip *et al.* [56], the authors pointed out a systematic shift of + 0.06 cm^{-1} with respect to previous data from the Meudon Observatory group [68], also using a concave grating spectrograph. This shift was attributed to the calibration procedure where reference lines emitted by an auxiliary discharge, probably with a different illumination of the grating, were superimposed on the experimental spectrum. Since a similar procedure was also used by Dabrowski and Herzberg [64] for calibration of their D_2 spectrum, a systematic shift of their data with respect to the present laser-based results may have the same origin.

A second comparison is made between the observed transition frequencies and calculations based on the theoretical framework as presented in Refs. [20, 69]. The upper-level energies belonging to the excited states $B^1\Sigma_u^+$ and $C^1\Pi_u$ were calculated [20] by solving a set of coupled equations using the newest *ab initio* potentials by Wolniewicz *et al.* [22], taking into account the nonadiabatic coupling terms between $B^1\Sigma_u^+$, $C^1\Pi_u$, $B'^1\Sigma_u^+$ and $D^1\Pi_u$ states [23]. The differences between the observed and calculated transition energies, Δ_{o-c}, for the investigated lines belonging to the Lyman and Werner bands, are given in

Table 5.1. For most of the transitions satisfactory agreement was obtained. The remaining discrepancies, are probably due to nonadiabatic couplings with higher electronic states, that were neglected in the calculations.

5.4 Conclusion

We present highly accurate transition wavelengths ($\Delta\lambda/\lambda = 6 \times 10^{-8}$) and frequencies of some 39 spectral lines of D_2 in the $B^1\Sigma_u^+ \leftarrow X^1\Sigma_g^+, (v', 0)$ Lyman bands, for $v' = 9 - 11$, and in the $C^1\Pi_u \leftarrow X^1\Sigma_g^+(0, 0)$ Werner band. The present values of the transition wavelengths are substantially more accurate than the previously published data of Dabrowski and Herzberg [64], and will be used, together with the highly accurate XUV measurements on H_2 [8], as calibration lines for VUV emission studies, in particular for the D_2 and HD molecules.

5.5 Acknowledgments

This study was supported by the EC Integrated Infrastructure Initiative action (RI3-CT-2003-506350), including its Access to Research Infrastructures Program (Project-ID: lcvu001276).

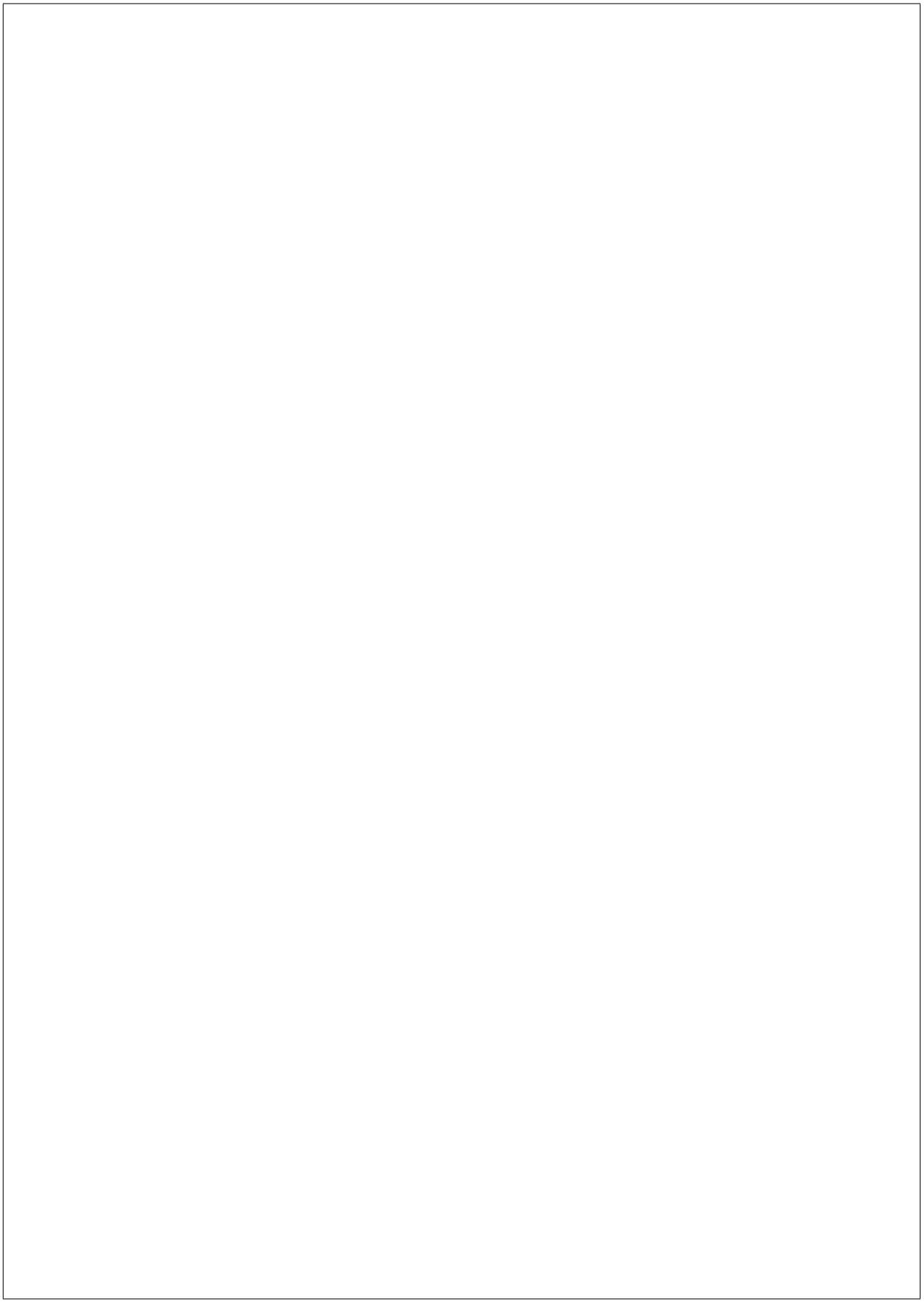

Chapter 6

Observation of a Rydberg Series in H^+H^-: A Heavy Bohr Atom

Abstract

We report on the realization of a *heavy* "Bohr atom", through the spectroscopic observation of a Rydberg series of bound quantum states at principal quantum numbers $n = 140$ to 230. The system is made heavy by replacing an electron inside a hydrogen atom by a composite H^- particle, thus forming a H^+H^- Coulombically bound system obeying the physical laws of a generalized atom with appropriate mass scaling.

Bohr developed the atomic model by imposing an *ad hoc* quantization condition on the angular momentum of an electron orbiting in the Coulombic potential of a positively charged nucleus [73]. The same solutions for the level energies are found by solving the Schrödinger equation for a quantum system bound by a $1/r$ potential; Rydberg states are represented by [74]

$$E_n = E_{\rm lim} - \frac{R_A}{(n-\delta)^2} \tag{6.1}$$

where R_A is the atomic Rydberg constant and n is the principal quantum number. For atoms with an extended core, *i.e.*, all atoms other than hydrogen, a quantum defect δ should be included. The wide variety of atomic and molecular realizations of Rydberg systems all have in common that the fundamental scale factor, the Rydberg constant, is essentially the same, because it is governed by the mass of the electron bound to a much heavier core: $R_A = (\mu/m_e)R_\infty$; for all these systems the reduced mass of the electron μ is close to m_e. Only few exotic systems like muonium (μ^+e^-) [75] or positronium (e^+e^-) [76] provide a different scale factor, the latter having exactly $R_\infty/2$.

Ion-pair systems bound by their Coulombic $1/r$ potential provide a realistic extension of the Rydberg concept to heavier systems. Initially the process of ion-pair formation above threshold was investigated by Chupka *et al.*, [77] measuring $H_2 + h\nu \rightarrow H^+ + H^-$. Hepburn and coworkers used the existence of long-lived bound states immediately below the ion-pair limit in their threshold ion-pair production spectroscopy (TIPPS) to determine accurate values of ion-pair dissociation thresholds, applied amongst others to the H^+H^- system [78]. Later Reinhold and Ubachs demonstrated the existence of bound heavy Rydberg states of the H^+H^- system through the probing of wave-packet dynamics in the densely structured quantum region several cm^{-1} below threshold [79]. These time-domain observations of heavy Rydberg states, conceptually analogous to observations of electronic wave packets [80,81], reveal the characteristic signatures of such states without resolving individual quantum states.

We report on the first experimental observation of a *frequency-resolved* quantum series of heavy Rydberg states in the H^+H^- system, here referred to as a heavy Bohr atom. Two-step laser-excitation is performed, starting in the ground state of the neutral H_2 molecule, using an extreme ultraviolet (XUV) pulsed laser source in the first step, populating an intermediate state in the molecule: the $C^1\Pi_u(v = 3, J = 1)$ state in *para*-hydrogen or the $B^1\Sigma_u^+(v = 12, J = 0)$ state in *ortho*-hydrogen. A second laser, tunable in the ultraviolet region then further excites the molecule towards the energetic region where the heavy Rydberg states are expected. A sketch of the experimental arrangement is presented in Fig. 6.1. The use of such a laser-based XUV source in a double-resonance excitation scheme, including the XUV spatial filtering method, were described by Reinhold *et al.* [82] (see also the inset of Fig. 6.1). Signal is detected by probing H_2^+-ions produced in the two-step excitation process. Alternatively, signals were detected (although weaker) by probing H^+-ions, which are produced via dissociation of the H_2 molecule. In the latter channel H atoms are formed, which are subsequently ionized to form H^+ by the UV-radiation from the second laser. The energetic region under investigation ($134\,000 - 138\,000$ cm^{-1}) is above the $n = 2$ and $n = 3$ dissociation limits in H_2 and both dissociative decay channels were experimentally observed. Level energies accessed in the two-step excitation process are derived from the well-determined intermediate levels [83] and from calibration of the second tunable laser.

Fig. 6.2 displays the fundamental discovery of the present study. A long series of regularly spaced resonances is observed in an energy window of some 2000 cm^{-1}. These resonances visibly follow the pattern of a Rydberg-like series indicated and numbered in the Figure. However, the Rydberg series is not as 'clean' as usually observed in atoms; the intensities, widths and line shapes vary across the series superimposed on a structured continuum, while some unassigned resonances are present as well. The series of quantum states with a Rydberg *electron* bound by an H_2^+ molecular core in quantum states $v^+ = 7$ and

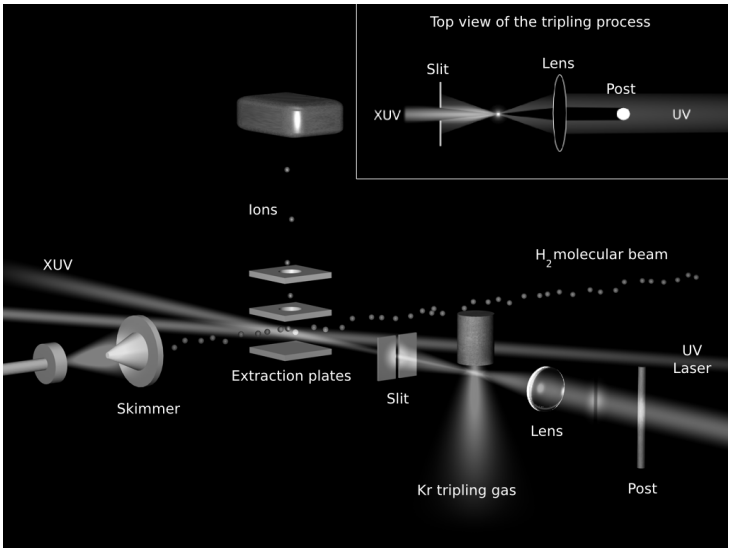

Figure 6.1: Experimental setup. An H_2 molecular beam is perpendicularly intersected with a beam of XUV radiation, obtained via third harmonic generation of a pulsed UV-laser beam underneath the orifice of a pulsed valve in krypton gas. The XUV radiation is geometrically filtered from the incident fundamental UV beam by selecting the phase-matched k_{XUV}-vector in a UV-dark region imposed by a post placed in the incident laser beam (see inset). H^+ and H_2^+ are extracted from the interaction region by a pulsed electric field for signal detection.

$N^+ = 0$, 2 or 4 (only *even* rotational quantum numbers for *para*-H_2), expected in this energy range, do not match the observed features. Alternatively, the series can be fitted to an equation for *heavy* Rydberg states:

$$E_n = E_{\mathrm{IP}} - \frac{R_h}{(n-\delta)^2} \tag{6.2}$$

where R_h denotes the Rydberg constant for the H^+H^- heavy Bohr atom. While in the experiment the $X^1\Sigma_g^+, v = 0, N = 0$ ground level of the neutral H_2 molecule is taken as the zero energy level, the H^+H^- (ion-pair) dissociation limit E_{IP} can be determined from a thermodynamic cycle [84], thus including the values for the ionization energy of the neutral H_2 molecule, the dissociation energy of the H_2^+ ion and the electron affinity of the H atom, yielding $E_{\mathrm{IP}} = \mathrm{IE}(H_2) + \mathrm{D}_0(H_2^+) - \mathrm{EA}(H)$ and resulting in $E_{\mathrm{IP}} = 139\,713.83$ cm^{-1}. The Rydberg constant for the heavy Bohr atom H^+H^- can be obtained by replacing the electron by an H^- particle, yielding the scaling factor $(\mu/m_e) = 918.5761$ [84]. Note that the Bohr radius for the heavy system is $a_0^h = 5.7 \times 10^{-14}$ m. Based on the numbers for E_{IP} and R_h the observed Rydberg series in *para*-hydrogen can be assigned to principal quantum numbers n

between 161 and 230 (with a gap between $n = 205 - 225$). A fit to Eq. (6.2) yields a value for the quantum defect of $\delta = 0.05$.

The observations displayed in Fig. 6.3 add to the findings. They show that the heavy Rydberg series can be observed at even lower energies, where states of $n = 140{-}150$ are located, that the $B^1\Sigma_u^+$ intermediate state of valence character can be used, as opposed to the $C^1\Pi_u$ state of molecular Rydberg character, and that the series can also be observed in *ortho*-H_2, as opposed to *para*-H_2 in Fig. 6.2. A remarkable observation features at excitation energies above 135 500 cm^{-1}, where the assignment in terms of Rydberg states in the heavy Bohr atom ceases to match. From the more detailed upper part of Fig. 6.3 it becomes clear that in this energy range the ordinary or electronic Rydberg states converging to the $v^+ = 6, N^+ = 1, 3$ limits in the *ortho*-H_2^+ core are excited. Also, some effects of mutual interaction between these Rydberg series, a well-known feature in molecular Rydberg series [85], seem to be present.

From the perspective of *electronic* Rydberg spectroscopy, an intermediate state with a $2p$ electron, $2p\sigma$ in case of the $B^1\Sigma_u^+$ state and $2p\pi$ in case of the $C^1\Pi_u$ state, should give rise to ns and nd series, as are indeed observed [86] in such excitation schemes in H_2. Considering the angular momenta in a Hund's case (d) framework, mutually interacting ns and nd Rydberg series converging to several allowed N^+ series limits are expected. This is indeed observed in

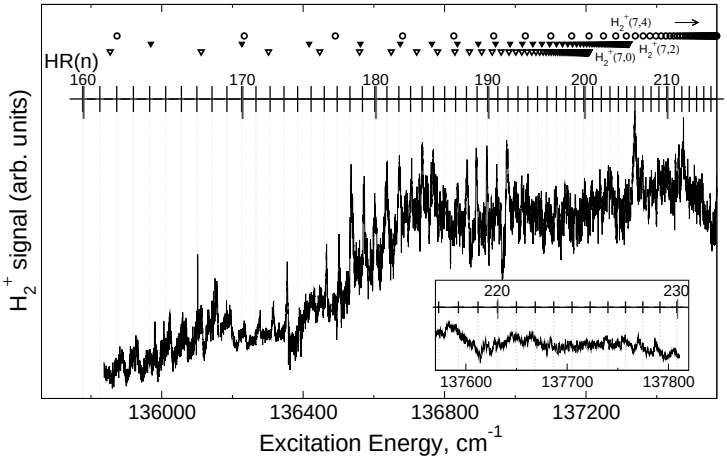

Figure 6.2: Characteristic spectrum after two-step laser excitation via C-X (3,0) R(0) in the *para*-H_2 molecule. The markers and dotted lines show the predicted positions in the heavy Bohr atom between $n = 161$ and $n = 230$ in the H^+H^- system. In the range between $n = 205{-}225$ the series is interrupted and overlaid by resonant structures, but appears again for $n = 225$. The Rydberg series converging to the $H_2^+(v^+ = 7, N^+ = 0, 2$ and $4)$ states of the ion are denoted with open triangles, full triangles and open circles, respectively.

Fig. 6.3 with series converging to $N^+ = 1$ and 3, for $v^+ = 6$ in the *ortho*-ion core. We observed the same phenomenon in *para*-hydrogen, when exciting via the $B^1\Sigma_u^+, v = 12, J = 1$ intermediate state in the energetic region near 135 600 cm^{-1} (not shown here), where Rydberg series converging to $N^+ = 0$, 2 and 4, for $v^+ = 6$ in the *para*-ion core are observed. However, the observed spectral lines, indicated by HR(n) in Figs. 6.2 and 6.3, are not associated with *electronic* states, but with excitations in the heavy H^+H^- system.

An elucidating connection can be made between the quantum numbers that characterize the heavy Bohr atom, principal quantum number n and angular momentum quantum numbers ℓ or J, and the usual molecular quantum numbers v and J associated with an intramolecular potential-energy curve (in this case $1/R$). This connection was established by Pan and Mies [87] to be $n \leftrightarrow v + J + 1$. It can be understood by considering the number of *radial nodes* in the wave function, v in the molecular system and $n - \ell - 1$, or $n - J - 1$ in the Rydberg system. In the present experiment for *ortho*-hydrogen only a $J = 1$ state is excited ($J = 0$ in the intermediate state); hence, a single n series in the heavy Bohr atom results through jumps in the v quantum number. In *para*-hydrogen (a $J = 1$ intermediate state) $J = 0$ and 2 states can be excited, when applying the $\Delta\ell = \Delta J = \pm 1$ (Laporte) selection rule in the heavy Bohr atom. Hence, *two* series might be expected, possibly with different quantum defects δ_J. Since this H^- particle is in a unique $^1S_0$ state, there exists only a *single* series limit (neglecting hyperfine structure).

In the potential-energy diagram (Fig. 6.4) a distinction is made between a short-range regime ($R < 12a_0$), where the covalent states in the H_2 molecule and the electronic Rydberg states are located, and a long range regime ($R > 12a_0$). At $\approx 10a_0$ the ion-pair potential undergoes a strong interaction (≈ 3000 cm^{-1}) with a dissociative state, thus giving rise to the characteristic double-well states in H_2, the $H\bar{H}^1\Sigma_g^+$ state in the g manifold [88] and the $B''\bar{B}^1\Sigma_u^+$ state in the u manifold [89]. Heavy Rydberg states with small principal quantum numbers, thus having bond lengths of the order of the scaled Bohr radius, are unphysical because the H^- ion itself is larger. Therefore, the principal quantum number n of the lowest essentially pure ion-pair state in H^+H^- is given by $R = n^2 a_0^h \approx 12a_0 \approx 6 \times 10^{-10}$ m, *i.e.*, $n \approx 100$.

All presently observed heavy Bohr atomic states fall in the energetic range between the H(1s)+H(3ℓ) and H(1s)+H(4ℓ) dissociation energies (see Fig. 6.4). Below $n = 130$ a perturbation in the heavy Rydberg series is expected, by about 60 cm^{-1} at $36a_0$, due to the avoided crossing with H(3ℓ) [21, 90, 91]. In this range and above $n = 250$, where another crossing with H(4ℓ) occurs (presumably with a strength of only a few cm^{-1}), the series in the heavy Bohr atom indeed dies out. Unresolved heavy Rydberg states were shown to exist above the $n = 4$ threshold by wave-packet experiments [84].

Photoexcitation of molecular states is governed by the Condon principle: Electronic orbitals are excited by the optical transition during which the nuclei

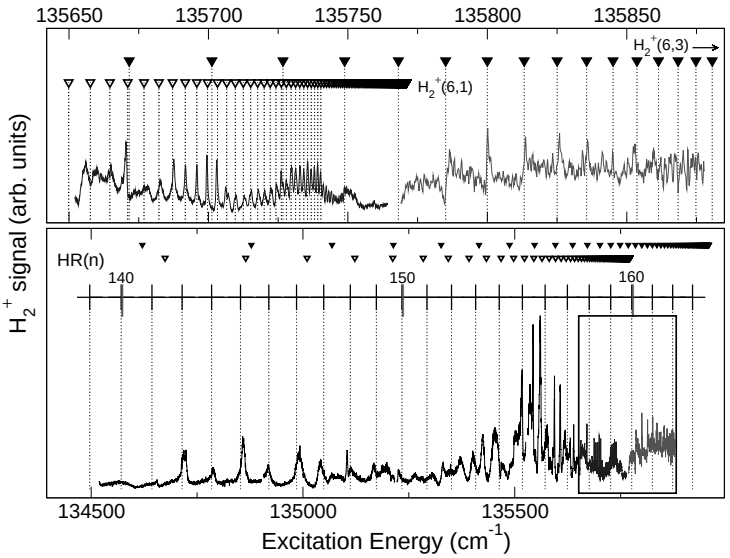

Figure 6.3: Lower panel: Characteristic spectrum after two-step laser excitation via B-X (12,0) P(1) in the *ortho*-H_2 molecule, showing $n = 140 - 162$ Rydberg states in the heavy Bohr atom. In the upper panel the part of the spectrum between 135 650 and 135 880 cm^{-1} is enlarged, showing the electronic Rydberg series converging to the $H_2^+(v^+ = 6, N^+ = 1, 3)$ states of the ion.

remain essentially fixed in space. As a result, the strengths of transitions are governed by the square of the overlap integral of the initial and final rovibrational wave functions of nuclear motion (the Franck-Condon factor):

$$I_n = |\int \Psi_n^*(R)\Psi_{B,C}(R)\, dR|^2 \tag{6.3}$$

By far the main part of the nuclear wave function of the heavy Rydberg states is at large internuclear distance (*e.g.*, the outer turning point for $n = 200$ is $R \approx 90a_0$), while the lower state is confined to $R < 6a_0$. The Franck-Condon factor of the transition should therefore be extremely small; further, excitation from the C state (which is confined to $R < 3a_0$) should be much weaker than from the B state, but this is not observed. From this we conclude that the heavy Rydberg states are not directly excited from the prepared intermediate B and C states via their Franck-Condon overlap.

We invoke the mechanism of a *complex resonance* [92] to resolve this issue. A superposition quantum state:

$$\Psi_c = \Psi_{hR}(n) + \sum_{v^+,J^+} \Psi(H_2^+, v^+, J^+; e^-) + \sum_{diss} \Psi(H, H^*) \tag{6.4}$$

with mixed character of electronic Rydberg channels (some 20 of those) associated with a $\Psi(H_2^+, v^+, J^+)$ core representing the ionization continua above

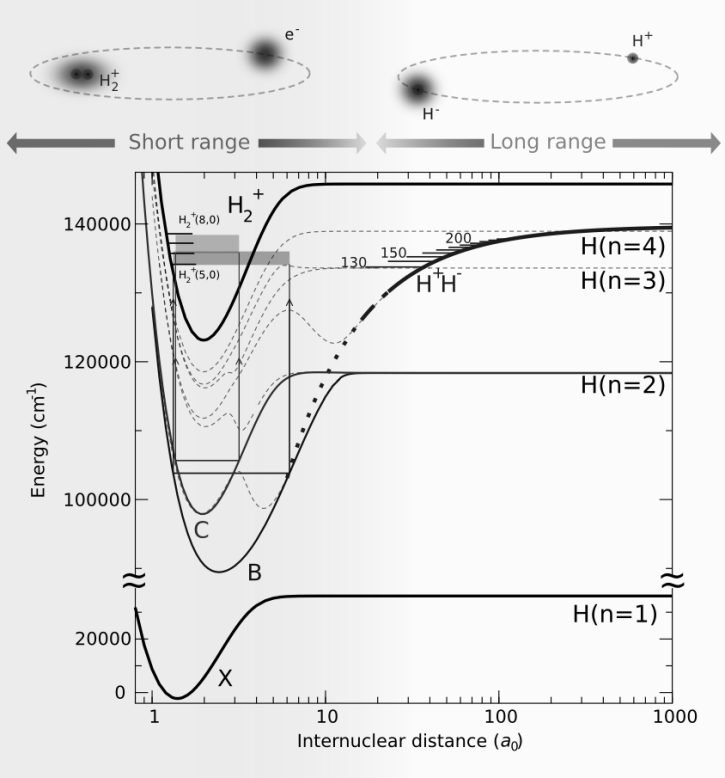

Figure 6.4: Potential-energy diagram of the H_2 molecule with distinction between two separated regimes: for $R < 12a_0$ the range of internuclear distances where covalently bound states and the electronic Rydberg states converging to $H_2^+(v^+, J^+)$ dominate (dashed lines representing the potential curves of *gerade* symmetry in this region [88]), and the range $R > 12a_0$ where H^+H^- heavy Rydberg states exist. The H^+H^- Coulomb potential is shown in dark (red) and extended to smaller R by dots. Intermediate energy levels in the B and C states (at $\sim$ 105 000 cm^{-1} excitation) are indicated and their accessible Franck-Condon ranges mapped (boxes).

each limit and a bound series below, dissociative continua (both $n = 2$ and $n = 3$ channels), and a series of Bohr atomic states $\Psi_{\mathrm{hR}}(n)$; in excitation the latter have a zero transition dipole moment. A crucial ingredient in the complex resonance model is a broad interloper state for which the transition dipole moment is large; a low n Rydberg state converging to a higher lying limit $H_2^+(v^+)$, hence a state in which v^+ is significantly larger than 6, takes on this role. As shown for another transition scheme in the H_2 molecule [92], under such conditions quantum interferences via different but indistinguishable pathways can lead to excitation of narrow series (in the example of [92] electronic Rydberg states), while excitation of the associated bound states may result in autoionizing decay. This closely matches the situation in the present experiment, although the number of channels is much larger than in an idealized example. The interpretation in terms of a complex resonance explains the occurrence of underlying (possibly structured) continua in the spectrum, the variation of widths over the bound series, and the variation of asymmetry in the line shapes exhibiting differing Fano parameters. At the same time it provides an explanation for the fact that H^+H^- heavy Bohr atomic states are *excited*, while signal is *detected* in another channel, such as H_2^+. A detailed quantitative analysis is beyond the scope of the present Letter.

It is interesting to note that the $p\overline{p}$ matter-antimatter protonium system [93] exhibits nearly the same Rydberg constant as the H^+H^- system. Hence both systems have a similar energy level structure. In H^+H^- the electrons have the positive effect to mediate a complex resonance, thus providing optical access to the series of heavy quantum states, a phenomenon which does not occur in $p\overline{p}$.

In conclusion, we have observed a frequency-resolved series of quantum resonances in a heavy Rydberg system by two-step excitation. In principle such series should be observable in any A^+B^- diatomic molecule, or in $A^+(BC)^-$ poly-atomic molecules [87], as long as the negative particle is bound (which would exclude *e.g.* N^-). In such systems a heavy Rydberg series is associated with each quantum state (rotational, vibrational, electronic and fine structure) in either of the two constituting particles. The presently studied H^+H^- system is the simplest, not only because H_2 is the simplest neutral molecule, but, in particular, since H^- in the $^1S_0$ state has no internal structure and therefore only a single Rydberg series limit exists, making the system truly a heavy *Bohr atom*.

Chapter 7

Construction of a Velocity Map Imaging Detection Setup

Abstract

This chapter reports on the development and preliminary characterization of a velocity map imaging (VMI) detection setup implemented in the existing extreme-ultraviolet (XUV) laser system at the Laser Center VU Amsterdam. The first part of the chapter focuses on the VMI technique and its capabilities. The modification of the detection scheme is explained in detail. Although still in the process of development, preliminary characterization and some results are discussed. Best focusing conditions of 400 μm obtained so far show that the system has not yet reached its optimal performance, mainly due to some inherent limitations. The technique for producing XUV light by non-linear frequency upconversion in a gas jet creates divergent XUV radiation, which determines a relatively large interaction region. This is a crucial element in VMI performance. Various effects and limitations are described in detail and future improvements are proposed. An XUV laser system that combines narrowband state-selective excitation with VMI detection of the ionized fragments would open up great possibilities for studying the dissociation dynamics of small molecules with spectroscopic features in the XUV domain.

7.1 Introduction

Photodissociation is one of the important elementary processes in molecular physics and chemistry. It results in breaking molecular bonds by the influence of light. The resulting fragments - atoms or molecules - can afterwards be involved in other chemical processes. Photodissociation plays a dominant role in atmospheric chemistry. A good example is the formation of the ozone layer in the Earth's stratosphere, where photodissociation of the oxygen molecule

into atoms takes place under the influence of the Sun's VUV radiation. These atoms are involved in ozone formation.

Photodissociation is a complex process, which keeps drawing the attention of scientists nowadays. In order for photodissociation to occur a molecule needs to be excited above a dissociation limit. In these energetic regions the molecular level structure tends to become complicated, with several bound and continuum states. This may lead to either direct or indirect dissociation, where one or more different dissociation pathways are involved. These phenomena are interesting as they provide fundamental information on the dynamics of photodissociation processes in terms of the underlying molecular quantum mechanics.

Velocity Map Imaging (VMI) is a powerful method for investigating photodissociation dynamics and involves the reconstruction of the spatial distribution and speed of the expanding fragments after breaking a chemical bond. During a dissociation process the fragments fly apart with strictly determined velocities defined by the photodissociating energy, the electronic structure of the parent molecule and the fragments produced. In this process expanding spheres of fragments called Newton spheres are created. When linearly polarized light is used in the dissociation step, these spheres show a characteristic three-dimensional angular distribution of the expanding fragments (Fig. 7.1). VMI takes a two-dimensional picture of the expanding fragments, which can be used afterwards to retrieve the corresponding three-dimensional form of the Newton spheres by inverse Abel transformation. The properties measured in

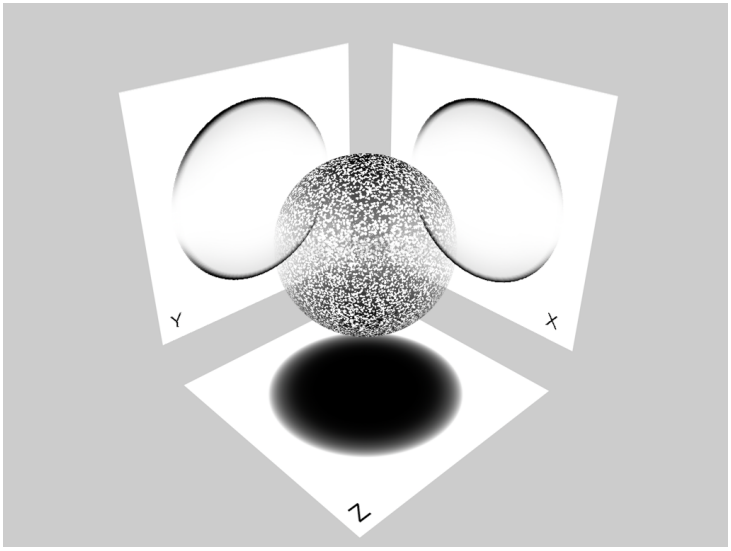

Figure 7.1: Two-dimensional projections of the Newton sphere produced by photodissociation.

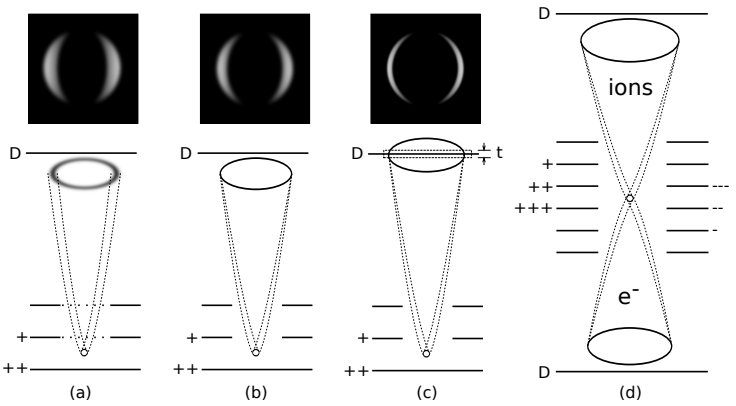

Figure 7.2: Schematic representation of the evolution of the imaging process as a tool for investigating photodissociation processes. (a) A Wiley - McLaren grid-based extraction system (note the grid - dashed lines) used by Chandler and Houston [94] provides spatial focusing. The size of the interaction area directly translates into blurring of the image. (b) Electrostatic lens based extraction system introduced by Eppink and Parker [95] allows for focusing particles with the same velocity at the same spot on the detector (D) regardless of the size of the interaction region. (c) Gebhardt *et al.* [96] used a method in which the ionized fragments are allowed to expand for a short period of time before switching on the extraction plates. Then, by time gating (t) of the MCP detector, a slice of the accelerated fragments can be obtained providing three-dimensional information on the accelerated fragments. (d) Hayden *et al.* [97] performed energy- and angle-resolved imaging, where both fragments and electrons are acquired in coincidence. The coincidence techniques so far provide the most complete information to study photodissociation processes.

these experiments include scalar quantities, such as photodissociation cross sections and branching ratios, and vectorial quantities such as angular distributions of the photofragments and their alignment or orientation. These parameters contain important information about the electronic structure of the parent molecule and its photodissociation dynamics.

The pioneering work of Chandler and Houston [94] has demonstrated the possibility of imaging the ionized photodissociation fragments onto a position-sensitive two-dimensional detector. They used a Wiley - McLaren grid-based time-of-flight (TOF) extraction scheme to image the dissociation products of methyl iodide (Fig. 7.2(a)). Eppink and Parker [95] extended the capabilities dramatically, in particular the kinetic energy resolution, by developing the VMI technique. Their modified electrostatic lens extraction system allowed for imaging of fragments originating from a different spatial position, but with similar velocities onto the same spot at the detector, thus mapping exactly the fragment velocity distribution (Fig. 7.2(b)). Further improvement based on

Eppink and Parker's work has been accomplished in the last decade, increasing the amount of information extracted by these experiments. Velocity map slice imaging [96] allows for improved resolution and three-dimensional information on the fragment's velocity by time gating the detection of the Newton sphere, such that only a part (slice) of it is detected (Fig. 7.2(c)). Coincidence imaging [97] is another configuration of this experiment, where both the ionized fragment and the associated electron are detected in coincidence, providing more comprehensive information about the photodissociation dynamics of the entire system (Fig. 7.2(d)). From the information on the angular distribution of the ionized fragments and their electrons it is possible to reconstruct the symmetry and energy of the parent molecule before dissociation. Together with state-selective excitation this technique provides a powerful tool for studying the energetic structure of molecules above their dissociation limits. Two recent reviews by Asfold *et al.* [98] and Chichinin *et al.* [99] provide a detailed overview of the recent advances of the imaging studies.

Many molecules exhibit spectroscopic features in the extreme-ultraviolet (XUV) domain. Especially interesting for studying fundamental processes in photodissociation are small diatomic molecules such as H_2, N_2, O_2, CO, etc. because of the well-developed theoretical models that describe their level structure. However, most of the modern laser-based imaging systems [95, 100, 101] operate up to the UV-VUV spectral region. In order to study diatomics a multiphoton process is necessary for dissociation, ionization, or both. This limits the accessible states and may complicate the angular distribution of the fragments. Imaging setups based on synchrotron radiation sources operate in a very broad XUV range [102]. A laser-based system, however, benefits from a higher spectral density, narrower bandwidth and better polarization control. In previous studies [103–106] such a narrowband XUV laser was successfully utilized for the spectroscopy of various diatomics, providing among the most accurate results on molecules such as H_2, N_2, CO, etc. and their isotopic analogues. These studies involved mostly different Resonance Enhanced Multiphoton Ionization (REMPI) schemes and detected the total ion signal, thus losing a wealth of information in the process. This multistep excitation capability, together with the new imaging detection system, could make the XUV laser an invaluable tool for investigating diatomic and small polyatomic molecules.

In the next section some aspects of photodissociation phenomena will be discussed, in particular those that affect the experimental study with fragment imaging techniques. The anisotropy parameter β characterizing the angular distribution of dissociation fragments due to polarized sources will be introduced. Next, the experimental characteristics of the XUV setup and the new detection design will be described in detail. In the results and discussions some preliminary images will be presented. Based on them the basic effects limiting the image quality will be discussed qualitatively and quantified for our detection scheme. Also, some suggestions for further improvement of the detection

performance will be presented.

7.2 Photodissociation

Photodissociation is a process in which a molecule is broken into fragments - atoms or molecules - by the influence of light. For simplicity only dissociation of diatomic molecules, leading to atomic fragments, will be discussed here unless stated otherwise.

Generally the photodissociation process can be thought to consist of two steps. The first involves excitation of a molecule by a sufficiently energetic photon to a highly excited state above a dissociation limit. Depending on the state reached in the second step the molecule breaks apart into fragments immediately (direct dissociation) or after a small period of time (indirect dissociation). This is important for the angular distribution of the fragments and will be discussed later in this section. As a result, two or more fragments with certain internal energies (E_A, E_B) are created and the remaining energy is released as kinetic energy (E_k). All this can be written schematically as:

$$AB + h\nu \rightarrow (AB)^* \rightarrow A(E_A) + B(E_B) + E_k \tag{7.1}$$

where the molecule AB is dissociated into the fragments A and B. They fly apart with velocities governed by the conservation of momentum and energy laws which can be written as:

$$M_A\overrightarrow{V_A} + M_B\overrightarrow{V_B} = 0 \tag{7.2}$$

$$E(AB) + h\nu = E(AB^*) = D_0(AB) + E(A) + E(B) + E_k \tag{7.3}$$

where M_A, M_B, $\overrightarrow{V_A}$, $\overrightarrow{V_B}$ are the masses and the velocity vectors of the fragments A and B, respectively. The second equation, in which $D_0(AB)$ represents the dissociation energy of the AB molecule, describes the energy transfer in the system. Both laws in essence define the image and are crucial for its interpretation.

If we look at the molecule using a coordinate system attached to the center-of-mass after the separation, both fragments will fly apart with velocities inversely proportional to their mass ratio. Including all possible orientations of the molecule in space would result in two concentric spheres expanding, one belonging to fragment A, the other to fragment B. The smaller sphere is associated with the fragment of heavier mass. It should also be noted that the radii of these spheres have a time-independent ratio equal to $R_A : R_B = V_A : V_B = m_B : m_A$ (Fig. 7.3(b)). Hence, from the conservation of momentum it follows that in dissociation the Newton spheres are always created in pairs with the same ratio of radii. As VMI directly maps these spheres onto a two-dimensional detector, the same will be true for the detected images.

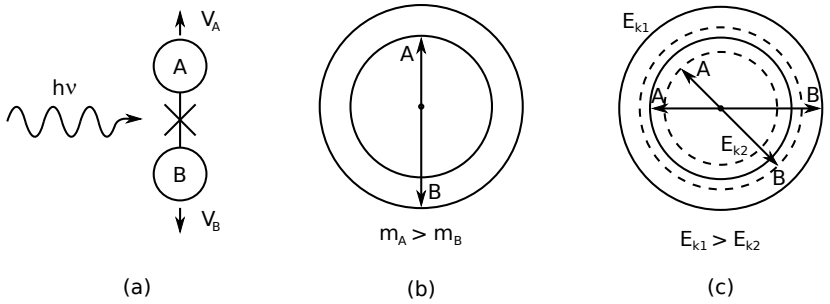

Figure 7.3: (a) Dissociation of the molecule AB into fragments A and B. (b) In the process two expanding spheres are created with radii inversely proportional to their masses. (c) Depending on the molecular structure of the parent molecule and/or the fragments different dissociation channels lead to different kinetic energies of the dissociation products. Larger internal energy of the fragment means smaller kinetic energy *i.e.* smaller rings.

Consider a situation in which the excited molecule can dissociate into two different channels, leading to fragments in different states. These fragments possess different internal energies and therefore different kinetic energies will be released. Hence, for each dissociation channel a pair of rings with the properties discussed above will be produced (Fig. 7.3(c)). From conservation of energy the smaller pair should represent the dissociation channel leading to fragments with higher total internal energy and vice versa.

In order for a detector to "register" a fragment, it needs to be ionized after it has been created by photodissociation. In the case that all the fragments are ionized, the configuration of Fig. 7.3(c) will be observed. In practice, however, different REMPI schemes are used to selectively ionize only one of the fragments. The most frequently used is the 2 + 1 REMPI scheme. It is characterized by its high photon flux and small interaction region. Very often the same laser is used both for the dissociation and ionization steps.

The detection scheme provides a means of simplifying the image. For example, N_2O dissociation at 203 nm results in an O atom in its excited $^1D_2$ state and rotationally hot ground-state N_2 in $X^1\Sigma_g^+$ $(v'' = 0 - 1, J'')$ [107]. The rotational quantum number J'' ranges from around 40 to 90. If the oxygen atom is used for detection, the image will contain more than 50 closely spaced rings related to the different (more than 50) kinetic energies the oxygen atoms will have. As the kinetic energies of the oxygen atoms differ only slightly, the rings in the image will be almost indistinguishable. If instead a suitably selective excitation scheme is used to ionize only *one* of the rotational states in the N_2 molecule, the image will contain only *one* ring as the ionized fragment possesses only *one* kinetic energy. This effect is illustrated in Fig. 7.4, where we recreate the experiment from Ref. [107].

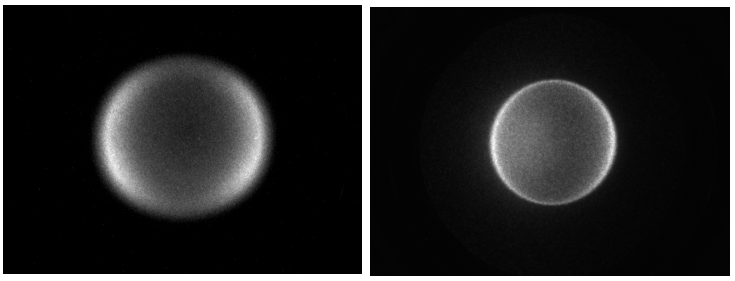

Figure 7.4: Image measured following the photodissociation of N_2O by 203 nm resulting in O atoms in their excited $^1D_2$ state and rotationally hot ground-state N_2 in $X^1\Sigma_g^+$ ($v''=0-1, J''=40-90$). (a) The oxygen atom is excited via 2 + 1 REMPI. Due to multiple decay channels leading to different internal energies of its partner the oxygen atoms possess more than 50 different velocities which partly overlap on the image, resulting in blurring. (b) On the other hand, N_2 in $X^1\Sigma_g^+$ ($v''=0, J''=74$) possesses only one velocity, and exciting it by 2 + 1 REMPI via the $a''(^1\Sigma_g^+)$ state results in a sharp one-component image. The slightly lighter background in the left part of the image is due to room-temperature background oil fragments with the same mass as N_2.

Fig. 7.4 shows that the fragment angular distribution is anisotropic. Zare and Herschbach [108] were the first to point out that the vector correlation between the dipole moment and the velocity of the fragments causes such an effect. When linearly polarized light is used for photodissociation, it excites preferentially the molecules which are oriented with their transition dipole moment parallel to its electric field vector. In the molecule-fixed frame, on the other hand, there is a strong correlation between the dipole moment vector and the internuclear axis - in the case of a diatomic molecule it can be either parallel or perpendicular to this axis (Fig. 7.5). As a result, the angular orientation of the excited molecules with respect to the laboratory-fixed frame attached to the laser electric field vector is anisotropic. The velocity of the fragments is oriented along the internuclear axis (axial recoil approximation) and thus results in an anisotropic angular distribution of the fragments with respect to the laboratory-fixed frame. In the case of direct dissociation induced by a single photon the angular distribution intensity $I(\theta)$ can be written as:

$$I(\theta) = (1 + \beta P_2(cos\theta))/4\pi \tag{7.4}$$

where θ is the angle between the electric field and the velocity of the fragment, $P_2(cos\theta)$ is the second Legendre polynomial and β is the so-called anisotropy parameter with values between -1 and 2. Within the axial recoil approximation fast dissociation of a diatomic molecule results in a sine distribution and $\beta = -1$ (Fig. 7.5(a)) or a cosine distribution and $\beta = 2$ (Fig. 7.5(b)). However, cases of breakdown of the axial recoil approximation are reported in which β

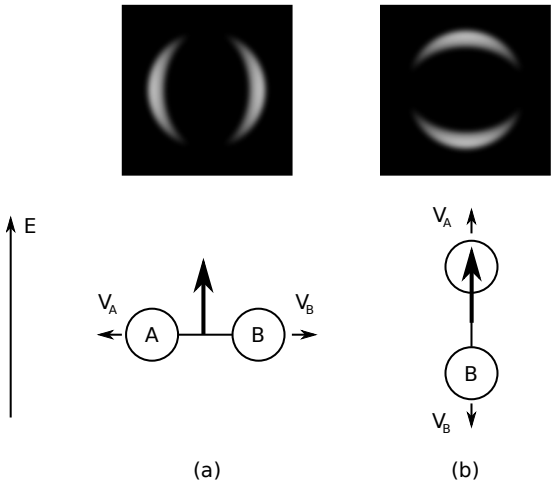

Figure 7.5: The angular distribution of the dissociation products provides important information on the properties of the parent molecule. The polarized light excites more efficiently molecules which have their dipole moment aligned with the light's electrical vector. In the first case (a) a perpendicular transition of a diatomic molecule results in fragments flying apart mainly horizontally, while in the second case (b) a parallel transition leads to dissociation products being distributed predominantly up and down.

differs from the limiting values discussed above [109]. In polyatomic molecules, where various bending modes exist, the non-axial recoil is common resulting in complicated distribution of the fragments, but β is still a characteristic parameter revealing information on the parent molecule. In the case of multiphoton excitation higher-order Legendre polynomials are necessary, together with one anisotropy parameter for each single excitation process [110].

When the parent molecule is excited to a state next to a curve crossing, another dissociation channel can be opened. Monitoring the angular distribution of the fragments and calibrating the branching ratios of both channels will provide information about the curve crossing probability and the absorption cross sections for both states involved.

The angular distribution described by equation 7.4 with β 2 or -1 results from fast dissociation, *i.e.* when the dissociation process occurs at a time scale much shorter than the classical rotation period of the parent molecule. In the case of predissociation or another kind of nonadiabatic (not direct) dissociation process in which the rotational period of the molecule is comparable to the dissociation time scale, the correlation between the directions in which the fragments separate and the transition dipole moment is significantly lowered. This can be expressed in terms of the lifetime of the state τ and the rotational frequency of the molecule ν [111]:

$$\beta_{||}(\tau) = 2(\nu^2\tau^2 + 1)/(4\nu^2\tau^2 + 1) \tag{7.5}$$

$$\beta_{\perp}(\tau) = -(\nu^2\tau^2 + 1)/(4\nu^2\tau^2 + 1) \tag{7.6}$$

For $\nu\tau >> 1$ the limiting values of $\beta_{||}$ and $\beta_{\perp}$ are 0.5 and -0.25. The case of direct dissociation where $\nu\tau << 1$ follows logically ($\beta_{||} = 2, \beta_{\perp} = -1$). Obtaining a proper value of β from the image therefore provides information on the lifetime and rotational period of the state of the parent molecule before dissociation. These two last examples show how powerful this method can be for studying molecular dynamics.

7.3 Experimental part - Description of the detection scheme

The Amsterdam XUV laser facility has been described previously [112–114]. Nevertheless, due to major changes in the detection system some experimental details are discussed again, this time with emphasis on the VMI performance.

The vacuum system consists of three differentially pumped chambers organized in an L-shaped configuration (Fig. 7.6). The tripling chamber is pumped by a diffusion pump (model VHS-10 - 6000l/s) through a liquid-nitrogen cooled trap for minimization of oil contamination. A piezo-driven valve with a 1 mm

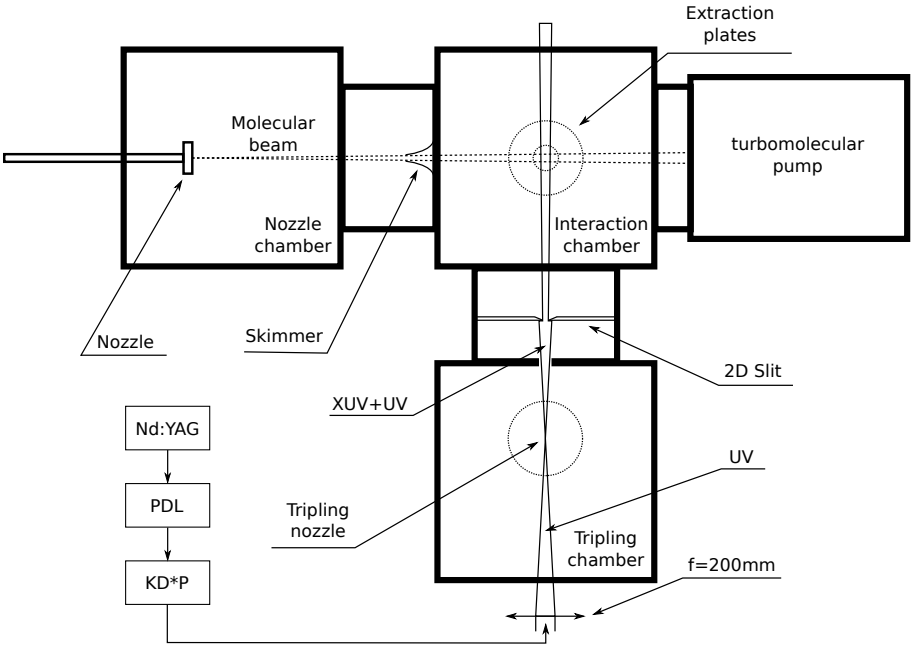

Figure 7.6: Experimental setup.

opening and operating at 10 Hz is used to create the jet of gas in which the frequency tripling takes place. Under operating conditions the pressure in the chamber is kept at about 10^{-5} mbar. An aperture of 3 mm ensures differential pumping with the interaction chamber. The last one is pumped by a turbo-molecular pump (model TMH521 - 520l/s) for oil free conditions. The pump is positioned such that the incoming molecular beam, after passing through the interaction region, is directed into the pump. The pressure during operation is maintained below 10^{-7} mbar. The third chamber contains the gas nozzle which introduces the sample molecule and is pumped by a diffusion pump (model Dif-160 - 650l/s) reaching pressures of 10^{-5} mbar under operating conditions. The gas nozzle is a General Valve (Series 9) with 0.8 mm opening which can be positioned from 0.2 mm to 9 cm away from a skimmer with a 0.5 mm orifice separating the nozzle and interaction chambers. For velocity map imaging the size of the interaction region is crucial for the quality of the images. In order to minimize it without introducing a second skimmer, the gas nozzle is positioned at the maximum distance of 9 cm. In this configuration the molecular beam is divergent with a half angle of 13.5 mrad. At a distance of 12 cm behind the skimmer the molecular beam is crossed perpendicularly by the excitation laser beam. A pulsed dye laser (Spectra Physics PDL-3), pumped by the second harmonic of a Nd:YAG laser (Spectra Physics Quanta Ray 330), produces 5 ns laser pulses in the visible spectral domain (555-660 nm) with a repetition rate of 10 Hz. These pulses are frequency upconverted to the UV spectral domain by second-harmonic generation in KD*P. A 200 mm lens focuses them into a Xe jet to generate odd harmonics (mainly third) of coherent XUV light pulses. The divergent XUV and UV overlapping pulses are spatially restricted by a two-dimensional slit situated 8.5 cm away from the focus. The slit opening is kept at about 380 μm which results in a cone of divergent laser radiation with a diameter of 1 mm at the interaction region. The molecular beam diameter determines the length in the third dimension. As a result an interaction region of ~ 1 mm $\times$ 1 mm $\times$ 2.4 mm is estimated. The dimension to which the quality of the image is most sensitive lies in the direction of the time-of-flight detection and is ~ 1 mm in our case.

Previously the detection system consisted of a time-of-flight detector optimized for mass resolution which recorded the integrated ion signal. The new VMI setup provides another degree of freedom, *i.e.* the possibility of detecting the two-dimensional distribution of the accelerated ions. In Fig. 7.7 the newly constructed time-of-flight system is shown. It is positioned perpendicularly to the plane defined by the laser and molecular beams. The extraction plates are cylindrical with an outer diameter of 70 mm and a thickness of 1 mm. The repeller plate has a 1 mm diameter hole in the center. This provides the opportunity of positioning the time-of-flight setup in different orientations with respect to the direction of the molecular beam. The second (extractor) and the third (ground) plates have openings of 30 mm. The three extraction plates

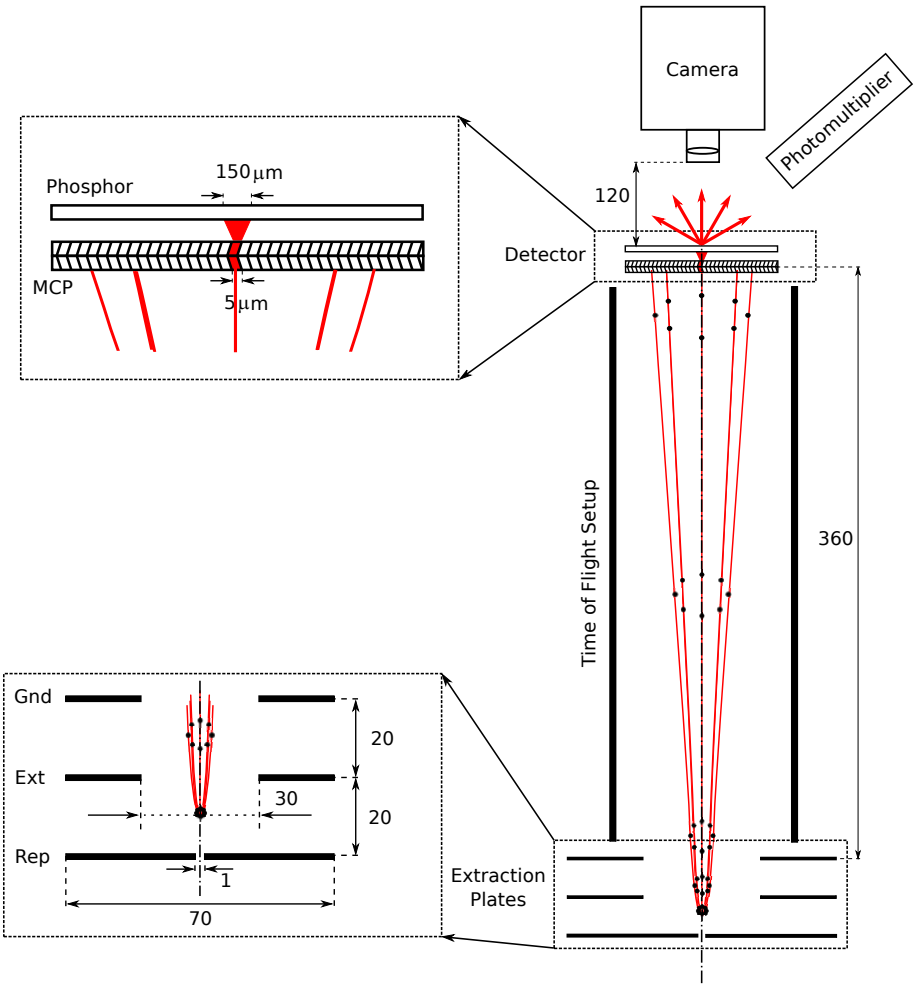

Figure 7.7: Drawing of the detection setup. The trajectories of the ions are simulated with SIMION software and rescaled appropriately to fit in the drawing.

are separated from each other by a distance of 20 mm. Under velocity map imaging conditions the potentials applied to the extractor and repeller plates should be in the ratio of about 0.7, while the third plate is grounded. The power supplies for both extraction plates are home built, based on a KS010P power supply with a maximum output voltage of 10 kV. The applied voltage can be DC or in the form of square pulses using Behlke HTS121 switches. The ionized accelerated particles are very sensitive to stray electric fields that can perturb their trajectories. To ensure minimization of this effect, a grounded tube has been inserted around the path of the particles creating unperturbed field-free flight conditions. The actual ion flight trajectories are simulated and plotted in Fig. 7.7. They are for ions with initial velocity vectors lying in the plane of the figure and spanning over the entire angle range in steps of 45 deg.

In the detection process the expanding Newton sphere is projected onto a two-dimensional micro channel plate detector (Photonis APD 3040FM 6/5/8 I 60:1 P-47 MgO). It consists of two 40 mm MCP plates organized in a Chevron configuration. Each one of them represents a stack of multiple hollow cylinders made from a dielectric material which acts as a continuous-dynode electron multiplier in which the multiplication takes place in the presence of a strong electric field. Good two-dimensional resolution is assured by the small dimensions of each of these electron multipliers with a diameter of 5 μm, a length of 300 μm (aspect ratio of 60:1) and a distance between the centers of 6 μm. They are also tilted at 8 deg with respect to the surface to ensure effective impact of the particle or photon on the dielectric surface of the channel. The electrons produced are amplified further to reach an amplification above 10^7. Magnesium oxide is deposited on the front surface in order to minimize the detection of scattered UV photons. While in most cases a negative voltage is applied to the front electrode, it was decided to actually ground it in order to keep the option open to implement electron imaging in the future. The voltage applied to the end of the MCP is provided by a 2.5 kV home built power supply restricted to 2.3 kV, which can supply either DC or pulses via a Behlke HTS41 push-pull switch. A 40 mm P-47 Phosphor screen with peak wavelength of 400 nm and decay time of 100 ns is chosen to visualize the events. While not very efficient (2.24W/mA), it has a very fast decay time so that the time-of-flight signal is least affected.

A photomultiplier tube (Philips XP1911/08) is positioned such that it can monitor the entire surface of the phosphor screen, thus collecting a spatially integrated signal. In this way the total mass-separated time-of-flight signal can be obtained as well. This option allows the system to be used for scanning spectroscopic studies as was possible before the modifications, albeit now with better signal-to-noise. Moreover, it provides the possibility, by introducing a mask on the phosphor screen, to detect only certain spatial regions. This feature can prove beneficial in cases where several phenomena result in spatially separable ion signals on the detector.

The image of the phosphor screen is recorded by a PCO.1300 camera with a resolution of 1392 x 1040. The camera was chosen for its low dark-count noise due to CCD cooling and long exposure time (up to 1 h). It can be used also in the ion counting regime, as the frame-per-second rate exceeds the repetition rate of our experiment (10 Hz). As shown in Fig. 7.7, the camera is positioned 12 cm away from the phosphor screen. At this distance the active aperture of the phosphor screen can be imaged onto the CCD chip such that it fully covers the width of the sensor. Then it is relatively easy to calibrate the area of the detector that each pixel represents. The active area of the MCP represents a circle with a diameter of 40 mm which is entirely mapped onto the sensor consisting of 1040 pixels. Hence, 1 pixel corresponds to $\sim 40 \times 40\ \mu m$.

The XUV laser radiation used as a dissociation/ionization source also photodissociates the carbon compounds of the background pump oil into fragments and ionizes them. The time-of-flight signal produced consists of distinct peaks corresponding to different masses. The signal due to hydrogen (mass 1) is relatively strong. Because of its small mass this fragment takes up almost all the kinetic energy released in the dissociation process, resulting in a broad velocity distribution which is imaged onto the detector as an almost uniform set of events.

The H signal arising from the pump oil is ideal for calibrating the response function of a single event on the detector. As a result of the electron multiplication process and the relatively large distance between the second MCP plate and the phosphor screen (1 mm), a single ion produces a relatively large intensity distribution on the detector, which needs to be taken into account. Analysis over 10 single events shows that each one of them produces a Gaussian-like intensity distribution with a FWHM of 3.7 px corresponding to 150 μm. A similar conclusion about the same type of detector has been reported by Wu [115].

7.4 Results and Discussions

The primary interest in building a VMI detection system is to study small diatomic molecules, in particular hydrogen, which exhibit interesting spectroscopic features in the XUV domain. For this reason the focus of this chapter is on the preliminary results and the detection performance using small molecules, the difficulties associated with detecting them, and possible future system modifications for improving the detection quality.

Parent ion images, *i.e.* images of direct ionization, can be used as a test of the focusing performance of the ion optics. The lack of dissociation ensures that the excess energy is converted mainly into the kinetic energy of the electrons. Ignoring the recoil effect, the ions should be imaged as a spot onto the detector. Fig. 7.8 shows parent ion images of Kr and molecular hydrogen produced with repeller and extractor voltages of 2000 V and 1520 V respectively. The

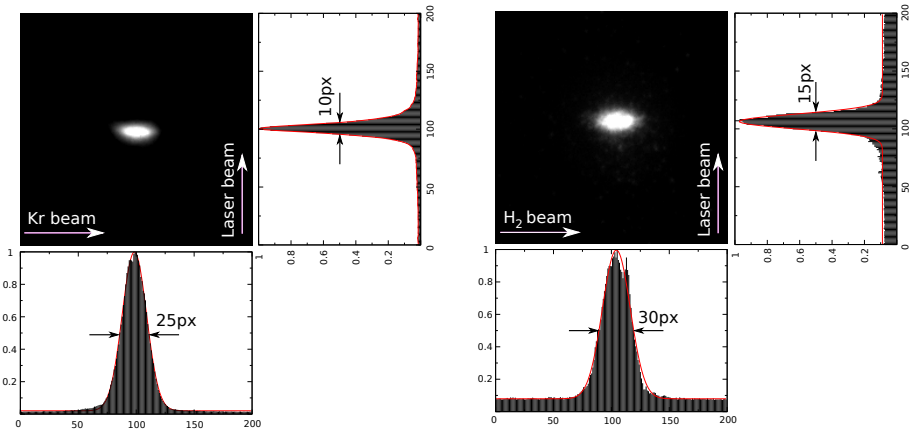

Figure 7.8: Focusing of Kr^+(left) and H_2^+(right) ions produced by 1 XUV + 1 UV REMPI via 5d $^2[1/2]_1^o$ and C $^1\Pi_u$ ($v' = 2, J' = 1$) respectively. While on the horizontal axis the focusing depends on the speed ratio of the molecular beam, on the vertical axis it represents the best imaging conditions for an interaction region of $\sim$ 2 x 2 x 1 mm. One pixel corresponds to 40 μm. Extraction voltages of the repeller and extractor are 2000 V and 1520 V, respectively. Because of their smaller mass the H_2^+ ions are more strongly affected by the electron recoil effect.

elliptical image is distinctive for a perpendicular time-of-flight configuration and can be explained with the speed distribution in the molecular beam. As VMI maps absolute velocities, particles with different initial velocities will be mapped onto different spots on the detector. Measuring the intensity spread of the events on the detector along the molecular beam direction can be used for quantifying the velocity spread, thus monitoring the expansion quality of the molecular beam. In the direction of the laser beam, however, the transverse velocity is much smaller and the focusing performance reflects the setup imaging capabilities. The intensity distribution on the detector can be fitted with a Gaussian function resulting in 10 px (400 μm) for Kr and 15 px (600 μm) for molecular hydrogen. These results are well below the performance of best modern VMI setups [95, 100–102]. The reasons will be discussed in detail and possible solutions will be suggested.

Size of the interaction region

Working with XUV radiation is not an easy task, because it is strongly absorbed in the atmosphere and by any known material. Transmission optics are not available and reflective optics with efficiency below 20 % are the only way to control the beam. Clearly, one should use the minimum number of reflective components possible.

In our system we produce XUV by non-linear frequency tripling of UV light (280 - 320 nm) in a freely expanding Xe gas jet. This third-harmonic generation process has extremely low efficiency ($\sim\ 10^{-6} - 10^{-7}$), underlining the need for a sophisticated design of the experiment. Some 30-50 mJ of coherent UV radiation is focused into the densest part of the pulsed tripling gas jet producing a few nJ of divergent XUV radiation which overlaps spatially with the remaining strong UV light. This poses the first and greatest problem to solve.

In most imaging experiments 2 + 1 REMPI schemes are used. Such a scheme requires high photon densities which are achieved by focusing the laser beam. This determines a very small interaction region defined by the overlap of the molecular beam with the waist of the focused REMPI laser beam. In our experiment, however, the divergent XUV radiation defines a relatively large interaction region. It is well known [95] that for VMI the size of the ionization source matters, especially when it is extended along the direction of the time of flight. In order to minimize it, a two-dimensional slit is used to restrict the cross section of the XUV beam to $\sim$ 1 x 1 mm. The interaction region is then reduced by about two orders of magnitude and so is the power. As a result an interaction region with dimensions of $\sim$ 2.4 x 1 x 1 mm is defined, still much larger than with most of the modern imaging setups. Further minimization of the XUV beam by narrowing the slit results in insufficient dissociation/ionization power.

A possible solution could be to introduce a concave mirror which can focus the XUV radiation to the required small volume. Photon losses due to its low reflectivity could be offset by the fact that all the XUV photons produced are now collected. A serious drawback is the strong UV radiation whose focus will overlap with the XUV focus dominating all the processes. A better approach would be to use a concave grating, yielding spatially separate XUV and UV focal points [113].

Molecular beam

As discussed briefly above, the quality of the molecular beam has important consequences for the quality of the image. On the one hand it defines the size of the interaction region, on the other its properties (velocity spread, divergence) determine the quality of the image. Pulsed molecular beams are created by opening of a nozzle for a very short time, which leads to gas expanding adiabatically into vacuum. During the process molecules in the beam undergo rotational cooling. The speed ratio of the expanding beam, *i.e.* the total translational velocity over the velocity spread, reflects the quality of the expansion. It depends on the gas backing pressure, opening time, the speed with which the valve can be closed, etc. Typical speed ratios are in the order of 10, while for more sophisticated nozzles they can reach higher values [116]. Once produced, the properties of the molecular beam degrade as a function of distance until it turns into an effusive beam. The distance at which the beam becomes effusive depends mainly on the quality of the vacuum, but also on possible physical

obstructions such as poor skimmers, etc. For VMI it is important that the interaction region is situated well before the molecular beam loses its supersonic properties.

In our experiment a General Valve nozzle is used to produce the molecular beam. To ensure a properly skimmed beam a 0.5 mm Beam Dynamics nickel skimmer with an orifice edge thickness of 10 μm is used. The pressures in the chambers are low enough to safely assume that the supersonic expansion cannot deteriorate within the length scale of our experiment. The divergence is estimated to be 13.5 mrad when the nozzle is 9 cm away from the skimmer, and can in principle be improved. For molecular hydrogen expanding at about 2500 m/s this will result in 34 m/s transverse velocity, which will increase the dimensions of the focused spot on the detector. Seeding the beam with a heavier gas (Xe or Kr) can be used for reducing the transverse velocity and will improve the quality of the beam as well. Fig. 7.8 shows that with Kr atoms propagating with a velocity of about 400 m/s, *i.e.* a transverse velocity of 5 m/s, the spot size obtained on the detector is smaller than with an H_2 beam. Certainly this is not the main effect causing the focusing difference, but it definitely contributes. Introducing a second skimmer will minimize the divergence by at least a factor of two and would further improve the expansion quality. Both effects are considered at present and will be implemented in the future.

Two-dimensional detector

As discussed in the Experimental section the detector by itself adds ~ 150 μm to the size of the focused spot. This means that, even if all ions are detected on the same spot of the detector, the camera will still register a 150 μm spot size. A way to minimize this effect is the use of event counting and centroiding routines [117]. This approach is best applicable to small signals or broad kinetic energy distributions. For each excitation event the ions are registered by the detector and produce well defined single hits. Next, a real time post-processing routine converts the Gaussian-like intensity distribution produced by each ion into a one pixel event positioned in the center of this distribution. It also sets up an intensity threshold below which everything is considered noise and can be removed. This procedure compensates for possible inhomogeneities in the efficiency of the detector, which would otherwise add up in time. As a result almost noiseless images are produced. The centroiding part on the other hand corrects for the apparatus function of the detector. Implementing the event-counting technique in our experiment is feasible, considering the small repetition rate of the excitation laser and the low ion excitation rate. The transfer rate of the camera allows for obtaining the images in real time and the post-processing computational load is negligible for a modern computer.

Ionization and electron-ion recoil

The imaging methods rely on the important assumption that the ionization process does not affect the expansion due to photodissociation fragments. The excess energy in the REMPI process is distributed between the ion and the electron. It is assumed that the electron will carry away all the excess energy as kinetic energy and the effect on the initial ion velocity will be negligible. In most cases when the excess energy is relatively small, this assumption is well justified. With high excess energy, however, this effect cannot be completely ignored. It results in observable ion recoil velocities whose magnitudes depend on excess energy. Since the magnitude of the ion recoil is independent of the preceding dissociation process, its relative importance will be larger for the smaller rings. It can result in blurring or even spurious ring splittings [110]. In the case of parent ion focusing, where no rings are produced, the REMPI recoil effect leads to a focusing spot increase. Lighter ions will be affected stronger by the electron recoil process and will give rise to a larger focused spot.

A demonstration of this effect can be observed in Fig. 7.8. Molecular hydrogen was ionized with 1+1' REMPI via $C^1\Pi_u(v' = 2, J' = 1)$, resulting in an excess energy of 13754 cm^{-1}. Since H_2 is a light molecule, the ion gets a considerable amount of this energy, or 3.82 cm^{-1} which corresponds to 218 m/s. This is a relatively large value considering that the molecular hydrogen expansion velocity is about 2500 m/s. In the other case, Kr was ionized with 1+1' REMPI via 5d $^2[1/2]^o_1$, resulting in an excess energy of 25616 cm^{-1}. This corresponds to 7 m/s, much lower than for molecular hydrogen. This is the main effect that causes the focusing differences which can be observed in Fig. 7.8.

In conclusion, small dissociation fragments with low kinetic energies are most susceptible to recoil effects due to ionization. To minimize the excess energy directly linked to the recoil strength, appropriate REMPI schemes should be employed.

Trajectory perturbations by charged particles

A large amount of positively charged ions created in a relatively small volume can perturb each others trajectories due to Coulomb forces. This results in the deformation of the normal spherical expansion of the fragments to an ellipsoidal shape directed along the dimension of highest density. The magnitude depends mainly on two factors - the ion production rate and the size of the interaction region.

In conventional 2 + 1 REMPI, where laser beams are highly focused into a very small interaction region, the trajectory distortion due to the Coulomb forces of other ions can be considerable. In order to avoid such perturbations a rule of thumb says that the ion production rate should be kept below ~ 100 ions/pulse [110]. Also, high photon densities can ionize not only the molecules studied, but also other species that might be in the focal volume (other back-

ground gases, pump oil, etc.). For the Coulomb effect all ions produced play a role. The lighter ions, however, will experience larger trajectory perturbations. One main reason for developing VMI detection is to study molecular hydrogen which dissociates into atomic fragments. Hence, a good vacuum and oil-free system are necessary conditions. Presently, our diffusion-pump-based system is being transformed into an oil-free system.

In comparison, the XUV setup features an interaction region that is at least 2 orders of magnitude larger than in the typical case of a 2 + 1 REMPI experiment. Hence, at the same production rates the ion density is then much smaller. As the Coulomb force is inversely proportional to the square of the distance between the ions, its effect on their trajectories will be smaller as well. For image acquisition we use typical ion production rates of 100-200 ions/pulse, thus the observation of image distortion due to Coulomb forces is unlikely. However, with our future plans to reduce the interaction region, which will also increase the photon density, this effect may become significant. Nevertheless, it can be easily controlled by adjusting the ionization/dissociation laser to appropriate power levels.

Doppler effect and bandwidth of the laser

The Doppler effect hardly plays a role in the quality of the image. Nevertheless, if not considered it can sometimes result in misleading observations. The XUV laser has a bandwidth of 0.3 cm^{-1} and crosses the molecular beam at 90 deg. As discussed above, the molecular beam has a divergence of 13.5 mrad corresponding to a 34 m/s transverse velocity, which can result in a frequency shift due to the Doppler effect of 0.01 cm^{-1}. This value is much lower than the laser bandwidth, so it is safe to say that the dissociation step will affect all molecules equally in terms of the Doppler effect.

The ionization step, however, produces a bigger challenge. In the case of REMPI, where the fragments are ionized via an intermediate state, only those that are resonant with the laser frequency will be affected. The dissociation fragments are flying out in all directions with velocities determined by the dissociation process. When a narrowband ionization laser is used or the fragments possess too high velocities, it can happen that only part of them are ionized due to the Doppler effect. In other words, only part of the Newton sphere is then detected. To achieve an image of the complete Newton sphere, simultaneous linear scanning over the transition should be performed during image acquisition. This technique has been used to produce the image in Fig. 7.4(b).

7.5 Conclusions and future work

A new velocity map imaging detection system has been developed in an attempt to build a system that benefits from both narrow bandwidth XUV excitation and VMI detection. While the detection part is already built and the first

images have been obtained, much more work needs to be done for improving the quality. A preliminary characterization and the first results on the focusing performace are shown. Various effects limiting the performance of the system are discussed and future improvements proposed.

While implementing such a detection system on the XUV laser in Amsterdam presents a significant challenge, the effort could prove rewarding as many small molecules possess complicated spectral structures exactly in the spectral region in which the system operates. This opens up new possibilities for a better understanding of photodissociation processes.

7.6 Acknowledgments

The author would like to acknowledge the Physical Chemistry Group at the Vrije Universiteit Amsterdam led by Prof. Dr. M. H. M. Janssen for their kind support with equipment and Dr. Wim Roeterdink and Dr. Daniel Irimia for fruitful discussions.

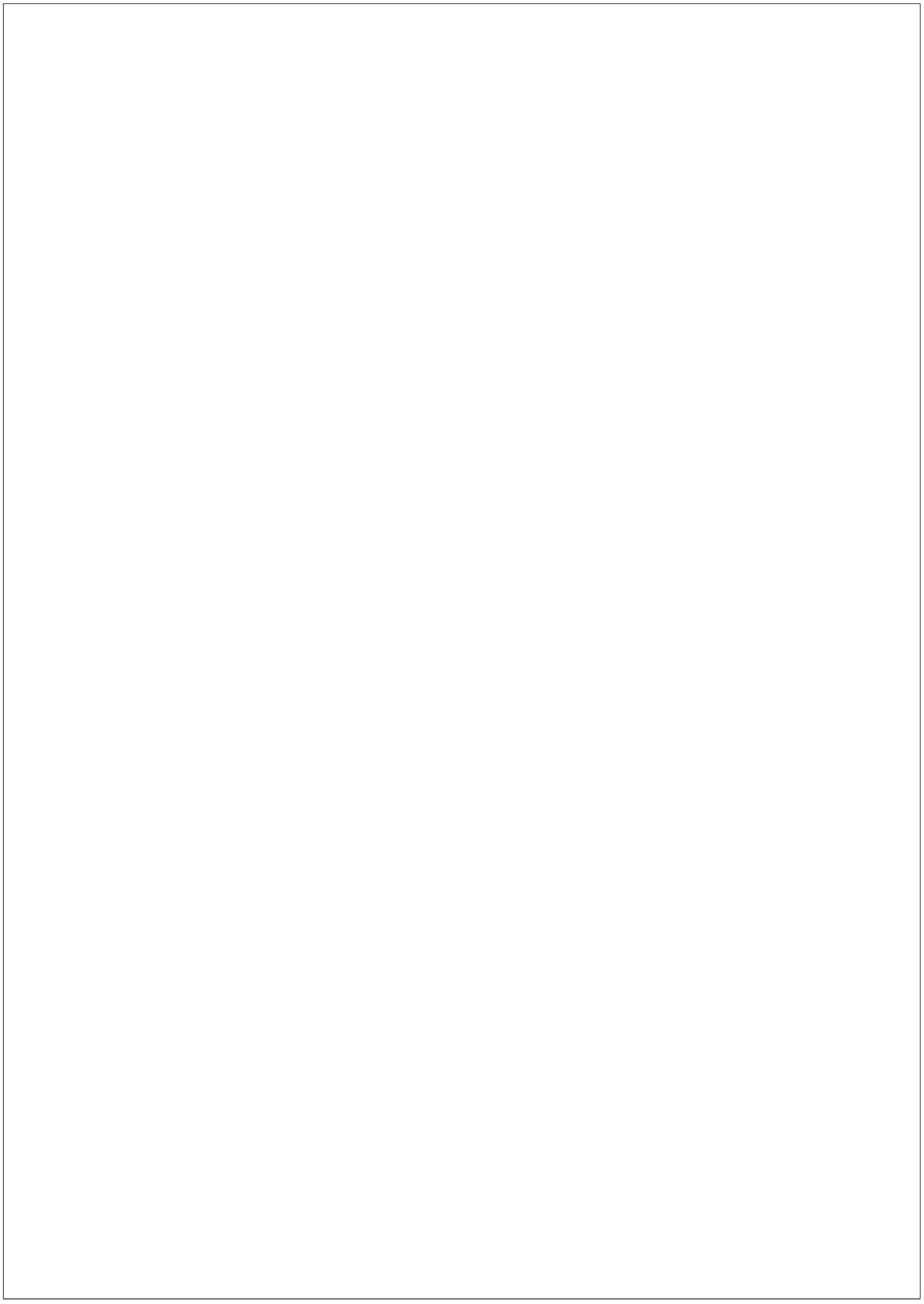

Chapter 8

Spectral assignment of dissociation resonances of *gerade* symmetry above the n=2 dissociation limit in H_2

Abstract

The resonance structure in molecular hydrogen above the n=2 dissociation limit was experimentally investigated in a 1 XUV + 1 VIS two-step laser excitation process. Spectral features exhibiting widths between one and several hundred cm^{-1} in the excitation range of $118500 - 120500$ cm^{-1} were probed by laser-ionization of the H(n=2) products produced in the dissociation process. The controlled double-resonance process combined with mass-selective detection imposes constraints on the possible allowed quantum states to be reached. Through the application of angular momentum selection rules in geometries with varying polarization properties of both laser beams, the para-ortho distinction, and the use of combination differences the predissociation resonances of *gerade* inversion symmetry in the singlet manifold of H_2 could be identified in terms of electronic symmetry and ro-vibrational quantum numbers.

8.1 Introduction

The hydrogen molecule is the simplest neutral molecule. As such, this species represents a fundamental test system for molecular theories. Despite its apparent simplicity a relatively large part of the spectral information, gathered in extensive work over many decades, is still unassigned and not fully understood.

The first observations made by Lyman [1] and Werner [121] have shown that even the lowest electric-dipole allowed transitions from the ground state lie well

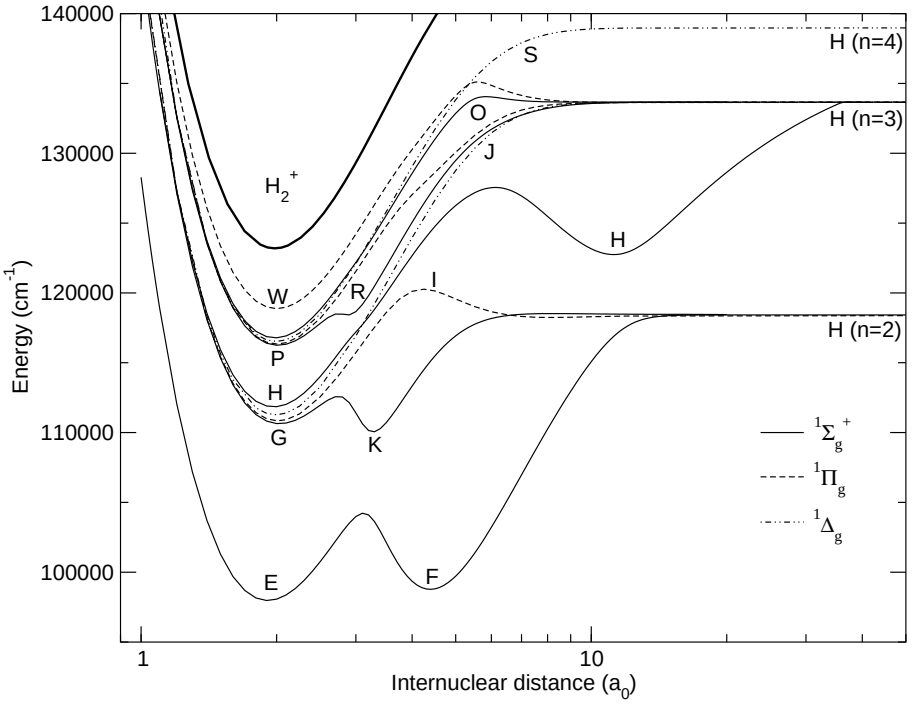

Figure 8.1: Born-Oppenheimer potential energy curves of the lowest *gerade* electronic states [118–120]

in the ultraviolet region, which provides serious experimental complications. Nevertheless, classical emission spectroscopy of a hydrogen discharge, reflecting also transitions between excited states, rendered a powerful tool for obtaining spectroscopic information about the electronic structure of the molecule. Dieke had used this technique for more than 30 years of research and produced a vast amount of experimental spectroscopic data about the hydrogen molecule and its isotopologues. Later his work was systematized and published by Crosswhite [4] and became known as the Dieke Atlas. However, the identification of the lines in these spectra proved complicated, on the one hand due to the lack of well-defined band structures, as seen in heavier molecules, and on the other, due to strong perturbations further enhanced by the small mass of the molecule. This is especially true for the singlet *gerade* manifold, where the repulsive $(2p\sigma_u)^2$ state (in diabatic picture) is responsible for a characteristic double-well potential even for the lowest excited states [122]. In the singlet *ungerade* manifold the first repulsive state lies at higher energy and therefore the lowest potential energy curves are unperturbed. Fig. 8.1 shows the lowest *gerade* potential energy curves according to the latest calculations by Wolniewicz and Dressler [118–120]. Most of the early assignment difficulties are connected

precisely with the complex interactions with this $(2p\sigma_u)^2$ repulsive state.

Throughout the years the interplay between experiment and theory has provided the most accurate description of this simple molecule. Classical emission spectroscopy is still the main source of experimental data [123–125]. On the basis of these measurements a theoretical treatment for the vibronic structure of H_2 and isotopologues has been developed by Dressler and coworkers [126,127]. Moreover, the development of XUV laser sources and their application to molecular hydrogen has produced a wealth of new information. Zare and coworkers [128, 129] were the first to observe the EF $^1\Sigma_g^+$ state by 2 + 1' Resonance Enhanced Multi-Photon Ionization (REMPI). Due to the small tuning range of their system they focused only on transitions to the lowest vibrational states ($v' = 0 - 4$). Tsukiyama *et al.* [130–132] carried out XUV-VIS double-resonance spectroscopy of molecular hydrogen probing higher lying vibrational states of EF, GK and I close to the n=2 dissociation limit. Not long after Lange-*et al.* improved the accuracies of some of them [133]. Recently, Bailly *et al.* compiled updated accurate level energies for most of the singlet-gerade states below H(n=2) [134]. On the theoretical side Yu and Dressler performed *ab initio* calculations for the lowest nine *gerade* states [135]. Their improved results were achieved by including the four singlet states involving the $4s\sigma_g$, $4d\sigma_g$, $4d\pi_g$ and $4d\delta_g$ excited molecular orbitals. The deviations from experiment were reduced to the order of a few cm^{-1} and helped eliminate wrong assignments involving the O $^1\Sigma_g^+$ state in the Dieke Atlas.

Almost all experiments and computations have focused on the region below the n=2 dissociation limit [82, 126–136]. In this energy region the lifetimes of the states are relatively long and data from the well-established emission spectroscopy can be used. However, above this dissociation limit continua play an important role, leading to predissociation of states and reduced lifetimes. It is, therefore, not surprising that emission spectroscopy is hardly possible in this energy range and different spectroscopies should be used. An added complication is that broad resonances can easily overlap, making accurate assignments difficult. As a result, the region above the n=2 dissociation limit remained largely unexplored.

Fig. 8.1 shows the possible electronic states in the energy region above n=2 that can be accessed in our experiments. The figure is limited to states of singlet gerade symmetry. All these electronic states possess rovibrational levels below and above the n=2 dissociation limit. The levels below that limit are experimentally observed [82,128–132,134] and identified in Ref. [82,135]. The levels above n=2 are the subject of the present investigation.

In an attempt to extend the assignment of the electronic states in molecular hydrogen XUV-VIS double-resonance spectroscopy is employed for an energy span of about 2000 cm^{-1} above the second dissociation limit. In this region most of the populated states predissociate rapidly into H(n=1) + H(n=2) atomic fragments, the latter of which are ionized. There exist also states which

do not predissociate and on ionization lead to the creation of molecular hydrogen ions. Therefore, monitoring both the ionized dissociation fragments and the H_2^+ ions is the best way to obtain full information about the H_2 states. Our XUV system, which combines the advantages of state-selective excitation with mass-selective detection of the ionized species proves to be a powerful tool for the assignment of unknown spectroscopic features. Through the application of the angular momentum selection rules a reliable rotational quantum number for each state can be determined. Moreover, the selection of the nuclear spin in the first excitation step further aids the assignment due to the J dependent para-ortho alternation. The proposed two-colour scheme is polarization-sensitive and allows to obtain further information by selecting the relative polarization of the two photons.

8.2 Experiment

As discussed previously, above the n=2 dissociation limit the electronic structure of molecular hydrogen cannot be studied by classical emission spectroscopy due to the interaction between bound states and various continua, leading to predissociation and reduced lifetimes. However, laser-based excitation together with mass-selective detection can be used to monitor the dissociation fragments. Fig. 8.2 illustrates the excitation scheme. When a bound state above the n=2 dissociation limit is excited through a 1 XUV + 1 VIS two-photon process, two hydrogen atoms, one in its ground state and one in the n=2 excited state, are formed. The excited atom is then ionized by a single UV photon. During an experiment the XUV photon energy is kept resonant to a selected transition to the C $^1\Pi_u$ $(v' = 2, J')$ state. The UV photon energy also remains constant. The spectrum is recorded by scanning the energy of the visible photon over a range of about 2000 cm^{-1}.

The experimental setup is shown in Fig. 8.3. A detailed explanation can be found in the previous chapter. In short, tunable XUV radiation is created by nonlinear frequency tripling. The coherent XUV pulses are produced by focusing some 30 mJ of UV, produced by doubling the output of a Pulsed Dye Laser (PDL), into a freely expanding pulsed gas jet of Xe. Together with the remnant UV from the tripling process the XUV beam crosses a skimmed beam of molecular hydrogen perpendicularly. The molecular beam is produced by a pulsed solenoid valve (General Valve Series 9), which is situated about 8 cm away from a 0.5 mm skimmer. A second laser beam, produced by a PDL delivering 7 ns laser pulses at 10 mJ in the visible spectral domain (620 – 660 nm), is introduced from the opposite side spatially coinciding with the path of the XUV and UV beams. The second PDL is synchronized to the first PDL so that the XUV, UV and VIS overlap in time in the interaction region. H_2^+ and H^+ ions are mass-separated after TOF and detected by an MCP detector. The electrons produced by the MCP excite a phosphorscreen, the fluorescence

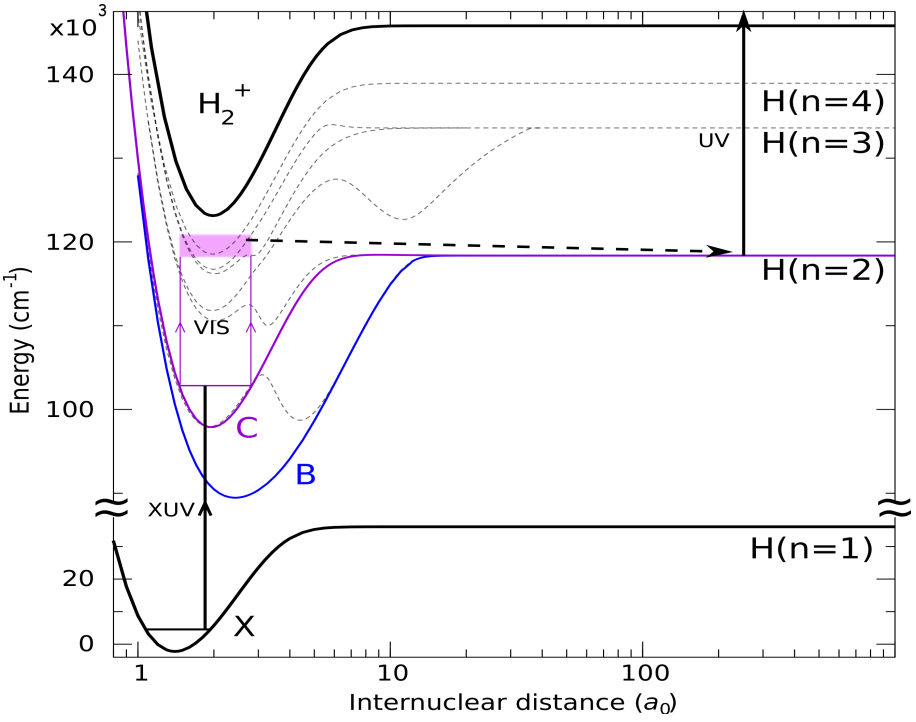

Figure 8.2: Excitation scheme. 1 XUV + 1 VIS two-photon excitation reaching the energy region just above the n=2 dissociation limit produces two hydrogen atoms, one in its ground state and one in the n=2 excited state. The excited atom is then ionized by a single UV photon. During an experiment the XUV photon energy is kept resonant to a selected transition to the C $^1\Pi_u$ $(v' = 2, J')$ state. The UV photon energy also remains constant. The spectum is recorded by scanning the energy of the visible photon over a range of about 2000 cm^{-1}.

of which is detected by a photomultiplier tube. The scanning is carried out by tuning the VIS PDL. Considering the broad linewidths observed and the sometimes poor S/N ratio, no particular effort is needed for the calibration. Line positions are determined to be accurate to within 1 cm^{-1} for all scans.

As will be discussed in detail in the next section, due to different possible competing channels, the H^+ and H_2^+ signals should be recorded simultaneously for full information on the system. Fig. 8.4 shows typical H^+ and H_2^+ mass-selected spectra produced by scanning the visible laser, while the XUV is fixed to a transition, in this case $C^1\Pi_u$ $(v' = 2, J' = 1) \leftarrow X^1\Sigma_g^+$ $(v'' = 0, J'' = 1)$. It can be seen that both traces contain spectroscopic features. The ones in the H_2^+ trace are related to states with a long lifetime, while the ones in the H^+ trace to states with shorter lifetimes. The sudden change in H_2^+ signal at 119900 cm^{-1} is a result of a frequency drift in the first PDL, which should

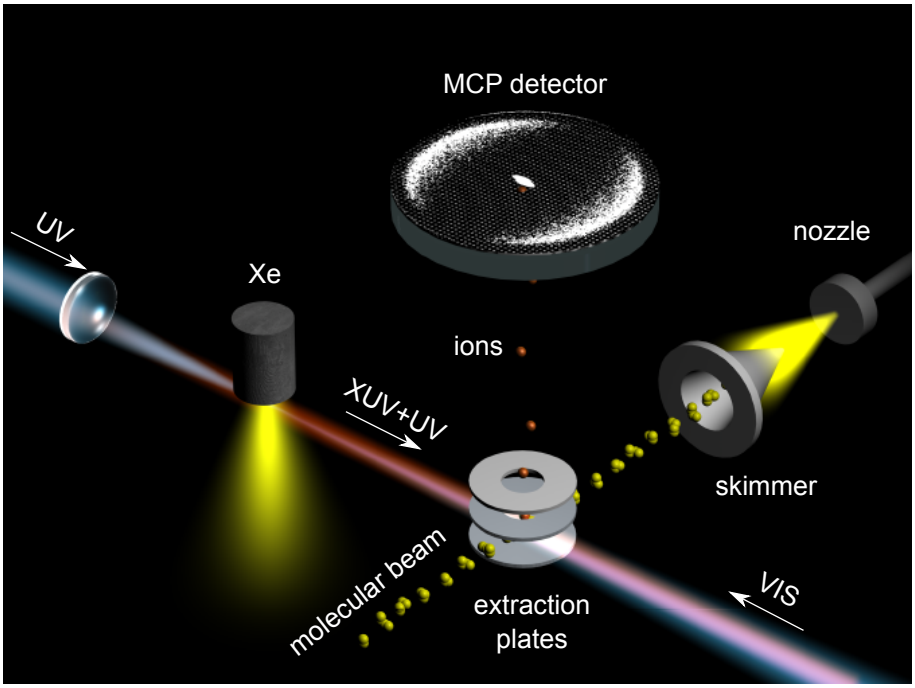

Figure 8.3: Experimental setup. Tunable XUV radiation is created by focusing the frequency-doubled output of a pulsed dye laser into a Xe gas jet by a 20 cm lens. Together with the remnant UV in the tripling process, it crosses perpendicularly a skimmed beam of molecular hydrogen. A second pulsed laser beam in the visible spectral domain is introduced from the opposite direction overlapping spatially and temporally with the XUV and UV radiation. The produced H_2^+ and H^+ ions are mass-separated after TOF and detected by an MCP detector. The electrons produced by the MCP excite a phosphorscreen, the fluorescence of which is detected by a photomultiplier tube.

be resonant to a transition during the scan. At that position the scan was interrupted and the frequency readjusted. Such artifacts can be corrected for in all dissociation traces.

Using the above procedure H_2^+ traces, as well as H^+ traces, that can only originate from dissociation, are recorded via several intermediate states. In particular, the transitions via $C - X$ $(2,0)$ R0, R1, R2, R3, Q1, Q2 and Q3 are used. It was experimentally observed that when excitation was carried out via an intermediate state $B^1\Sigma_u^+$ $(v' = 12, J')$, a strong constant signal dominated the dissociation traces. Therefore, these traces were not recorded in detail. Scheper *et al.* [137,138] have reported similar observations of strong dissociation when exciting via the $B^1\Sigma_u^+$ state.

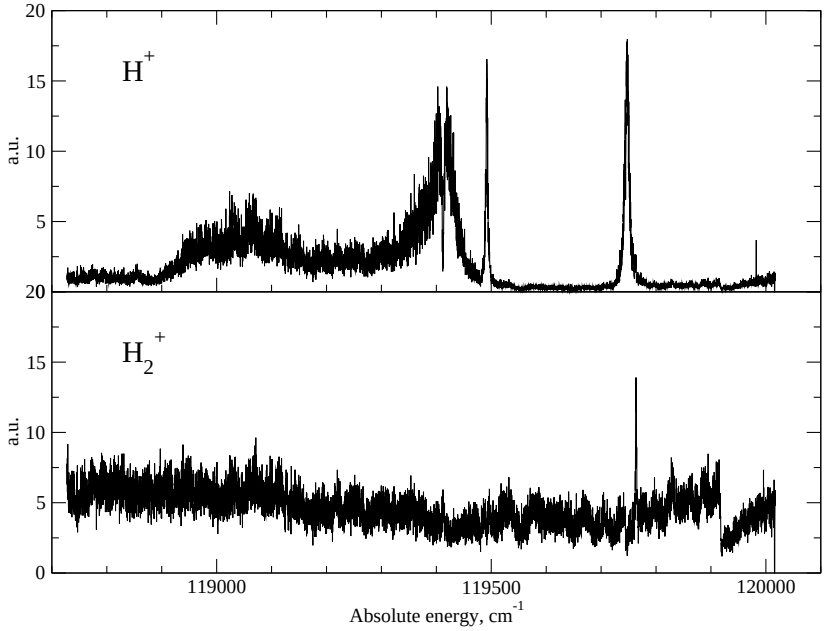

Figure 8.4: H^+ and H_2^+ traces produced by 1 XUV + 1 VIS + 1 UV. The XUV photon energy is fixed to the Q1 transition of $C - X$ $(2, 0)$. The traces are produced by only scanning the VIS photon energy. Along the horizontal axis the total excitation energy with respect to the $X^1\Sigma_g^+$ $(v'' = 0, J'' = 0)$ is given.

8.3 Results and discussions

Excitation scheme and possible channels

Most of the electronic states above the n=2 dissociation limit are strongly coupled to various continua and experience reduced lifetimes due to the ensuing strong predissociation. That is the reason for the lack of information about these stated from emission spectroscopy. To study these states it is necessary to monitor the dissociation products. Fig. 8.2 shows our experimental scheme where the dissociation fragment H(n=2) is ionized and the resulting H^+ ion mass-detected.

As discussed in the previous section, due to the specifics of the XUV production, it is difficult to separate in time the XUV, used for populating the various rotational states of $C^1\Pi_u$ $(v' = 2, J')$, and the UV, used for ionization of the H(n=2) fragments. This implies that the dissociation products are created within the 5 ns pulse width of the XUV and UV. The probing PDL, providing 7 ns VIS pulses, is temporally overlapped with the XUV and UV pulses for maximum excitation efficiency.

In an experiment that involves three different pulsed laser beams that over-

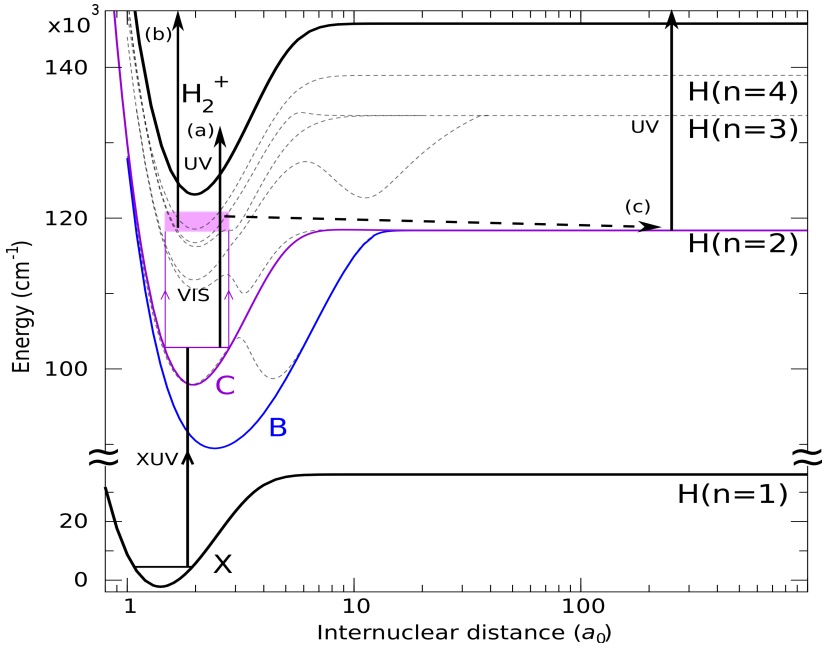

Figure 8.5: Possible channels contributing to the H^+ and H_2^+ traces. (a) 1 XUV + 1 UV REMPI ionization resulting in a constant H_2^+ signal. (b) 1 XUV + 1 VIS + 1 UV REMPI also creating H_2^+ ions. (c) 1 XUV + 1 VIS excitation followed by dissociation into H(n=1) + H(n=2) fragments. Ionization with 1 UV photon of the H(n=2) fragments gives rise to H^+ signal.

lap in time (see Fig. 8.5) several competing processes can be distinguished. The first process (a) is direct 1 XUV + 1 UV REMPI producing H_2^+ ions. Considering that the XUV and UV photon energies are related to each other (1 XUV = 3 UV) and that the former is fixed to a specific transition involving $C^1\Pi_u$ $(v' = 2, J')$, this process yields a constant H_2^+ signal. The other two processes, (b) and (c), represent the excitation of a certain state by 1 XUV + 1 VIS. Depending on the lifetime of the state, it can either dissociate into H (n=1) + H (n=2), the last one of which is ionized, or be directly ionized producing H_2^+ ions. The processes (b) and (c) are responsible for the observed spectroscopic features in the H_2^+ and H^+ traces, respectively. For example, in Fig. 8.4 the H^+ trace is a result of the (c) process, while in the H_2^+ trace the constant background is a result of process (a) and the transition at 119768 cm^{-1} is a result of process (b). There is another channel involving population of an intermediate state $C^1\Pi_u$ $(v' = 2, J')$, followed by UV + VIS two-photon excitation. However, this channel is estimated to be unimportant and in first approximation is neglected.

Channel (a) should provide a constant H_2^+ signal. However, Fig. 8.4 shows

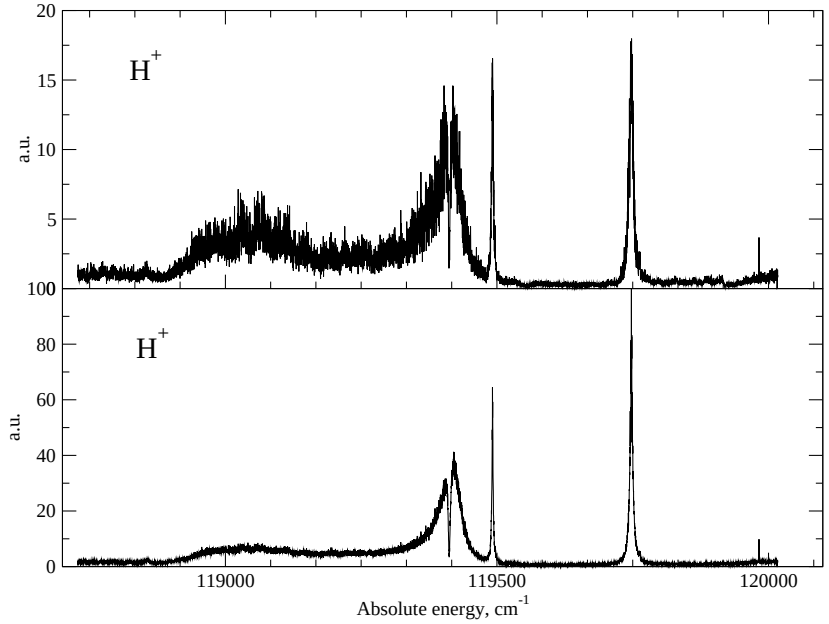

Figure 8.6: Dissociation trace produced by 1 XUV + 1 VIS excitation via $C - X$ $(2,0)$ Q1 intermediate state - before and after division by channel (a) from Fig. 8.5

a relatively noisy signal. Fluctuations in the tripling gas pressure and shot-to-shot power differences in the UV amount to strong fluctuations in the XUV production. Together with the molecular hydrogen density fluctuations, related to the general valve pulse operation, they produce a relatively poor S/N ratio. These fluctuations will play the same role in each of the possible channels. Hence, the noise observed in both channels is correlated. The signal of channel (a) can then be used as a reference to monitor these strong fluctuations. Dividing the dissociation spectra by the reference signal removes the correlated noise, resulting in a strongly improved S/N ratio. Of course, the spectroscopic features related to the (b) process should first be removed from the H_2^+ trace. They are fitted with a Gaussian profile which represents the apparatus function. Then, the entire spectrum is divided by the fitting functions of the transitions, leaving only the correlated noise present. In Fig. 8.6 the upper trace represents an experimentally observed dissociation spectrum. The lower trace shows the effect of removing the correlated noise. Note that the artifact produced by interupting the scan at 119900 cm^{-1} is also compensated for.

Channel (a) can also be looked at as a process that probes the population of the intermediate state. Its relative strength depends on the probability of

excitation into the ionization continuum with a UV photon, and the competition with channels (b) and (c), which also depopulate the intermediate state. While the (b) process also creates H_2^+ signal, the (c) process creates H^+ signal. Hence, when accessing a dissociation resonance, a drop in the H_2^+ signal is observed, due to the depopulation of the intermediate state. When very strong, this effect can perturb the lineshapes of the spectroscopic features in the dissociation channel. The division by the reference signal corrects also for the depopulation of the intermediate state.

Following this approach, all dissociation traces are improved significantly. They are presented in Fig. 8.9 and Fig. 8.10, separated into para- and ortho-H_2. The reason for this separation will be discussed in the following section. In order to be able to compare the spectroscopic features of dissociation spectra via different intermediate states, it is convenient to plot all of them on an energy scale with respect to $X^1\Sigma_g^+$ ($v''=0, J''=0$). The necessary $C(v'=2, J')$ level energy information was taken from Ref. [134].

Symmetry aspects

In molecular physics there are several types of symmetry classifications depending on the symmetry operation and the part of the Hamiltonian involved - the total (+/-) parity , rotationless (*e/f*) parity, *gerade/ungerade* (*g/u*) parity and symmetric/antisymmetric (*s/a*) parity. They all correspond to eigenvalues +1 and −1, but some are labeled with letters instead to avoid confusion. Commutation of the Hamiltonian and any symmetry operator implies that a set of simultaneous eigenfunctions of the two operators can be found. When a molecule possesses a certain symmetry, the energy levels and wavefunctions can be labeled with corresponding symmetry properties. These symmetries play a key role in formulating selection rules and in calculating transition probabilities. The constraints posed by symmetry allow the assignment of unknown energy levels.

Total (+/-) parity

The total parity is associated with the inversion symmetry operator $\hat{E}^*$ (sometimes referred to I^{SF}). It replaces the spatial coordinates of all the particles in the system (nuclei, electrons) in the laboratory-fixed frame with origin at the center of mass by their negatives:

$$\hat{E}^*\psi(X_i, Y_i, Z_i) = \psi(-X_i, -Y_i, -Z_i) = \pm\psi(X_i, Y_i, Z_i) \tag{8.1}$$

It is a symmetry operator, because all the relative distances between the particles in the system remain the same, thus the energy levels are unchanged after the inversion operation. It can be shown [139,140] that the $\hat{E}^*$ operation in the laboratory-fixed frame is equivalent to the σ_v reflection operation (reflection in a plane including the internuclear bond) in the molecule-fixed frame. This

relation is very important, because in the Born-Oppenheimer approximation, where the nuclei are considered stationary, the electronic wave function is expressed in the molecule-fixed frame. The total wavefunction, excluding nuclear spin, can be written as a product wavefunction:

$$\psi = \psi_{el}\psi_{vib}\psi_{rot} \tag{8.2}$$

where ψ_{el},ψ_{vib}, ψ_{rot} are the electronic, vibrational and rotational contributions. Then, to find out how the reflection operator will affect the total wavefunction, we first consider how the components of the wavefunctions are affected separately. For small rotational quantum numbers in molecular hydrogen Hund's case (a) applies. Hougen has shown that in this case, the result of the inversion operation for each wavefunction can be written as [141]:

$$\begin{aligned}
\sigma_v(\psi_{el}) &= \sigma_v(|n\Lambda S\Sigma\rangle) = \pm(-1)^{\Lambda}(-1)^{S-\Sigma}|-\Lambda\rangle|S,-\Sigma\rangle \\
\sigma_v(\psi_{vib}) &= \sigma_v(|\nu\rangle) = |\nu\rangle \\
\sigma_v(\psi_{rot}) &= \sigma_v(|\Omega JM\rangle) = (-1)^{J-\Omega}|-\Omega JM\rangle
\end{aligned} \tag{8.3}$$

Hence, for the total wavefunction:

$$\begin{aligned}
\sigma_v(\psi_{el}\psi_{vib}\psi_{rot}) &= \sigma_v(|n\Lambda S\Sigma\rangle|\nu\rangle|\Omega JM\rangle) = \\
&= (-1)^{J-2\Sigma+S+\sigma}|n,-\Lambda,S,-\Sigma\rangle|\nu\rangle|-\Omega JM\rangle
\end{aligned} \tag{8.4}$$

Here $\sigma = 0$ for all states except Σ^- for which $\sigma = 1$ (Fig. 8.7).

Rotationless (e/f) parity

The rotationless or (e/f) parity represents the total parity with the rotational part removed. In Eq. 8.4 the total parity shows a J dependence coming from the $(-1)^J$ term. It is convenient to separate off this J dependence and to define the rovibronic part of the wavefunction as:

$$\hat{E}^*\psi = +(-1)^J\psi \qquad \text{for } e, \tag{8.5}$$

and

$$\hat{E}^*\psi = -(-1)^J\psi \qquad \text{for } f, \tag{8.6}$$

In this way the (e/f) parity concept is linked to the electronic state and does not change with rotational quantum number. Then, all rotational energy levels of $^1\Sigma^+$ have e parity, while those with $^1\Sigma^-$ have f parity. For $^1\Pi$ and $^1\Delta$ both e and f parities occur, because of the degeneracy of the associated levels (Fig. 8.7).

Gerade/ungerade (g/u) parity

In a homonuclear diatomic another symmetry operation exists, *viz.* the inversion symmetry of the wavefunction in the molecular body-fixed frame. This

inversion operator is designated as $\hat{i}$ and implies an additional symmetry classification. This operation only affects the electronic orbital part of the wavefunction and keeps the rotational, vibrational and the electronic spin contributions unchanged. Then:

$$\hat{i}|\Lambda\rangle = +|\Lambda\rangle \qquad \text{for } g, \tag{8.7}$$

and

$$\hat{i}|\Lambda\rangle = -|\Lambda\rangle \qquad \text{for } u, \tag{8.8}$$

Note that g/u symmetry is a property of the entire rotational manifold associated with an electronic state, unlike the total parity, where a J dependent alternation is present, or the e/f parity, where both can coexist in degenerate states with $\Lambda > 0$ (Fig. 8.7).

Symmetric/antisymmetric (s/a) parity due to nuclear spin

In the case of homonuclear diatomic molecules the Pauli exclusion principle demands that the total wavefunction, including nuclear spin, is symmetric (for bosons), or antisymmetric (for fermions) with respect to interchange of the spatial coordinates of the two identical nuclei:

$$\hat{P}_{12}(\psi\psi_{nuc}) = \hat{P}_{12}(\psi)\hat{P}_{12}(\psi_{nuc}) = \pm(\psi\psi_{nuc}) \tag{8.9}$$

The operator that interchanges the nuclei is a product of two familiar operators [142], *viz.* $\hat{P}_{12} = \hat{\sigma}_v\hat{i}$. Their action on $\psi = \psi_{el}\psi_{vib}\psi_{rot}$ was already described before. Thus, for *gerade* states the total parity matches the s/a parity, for *ungerade* states the total parity is opposite to the s/a parity.

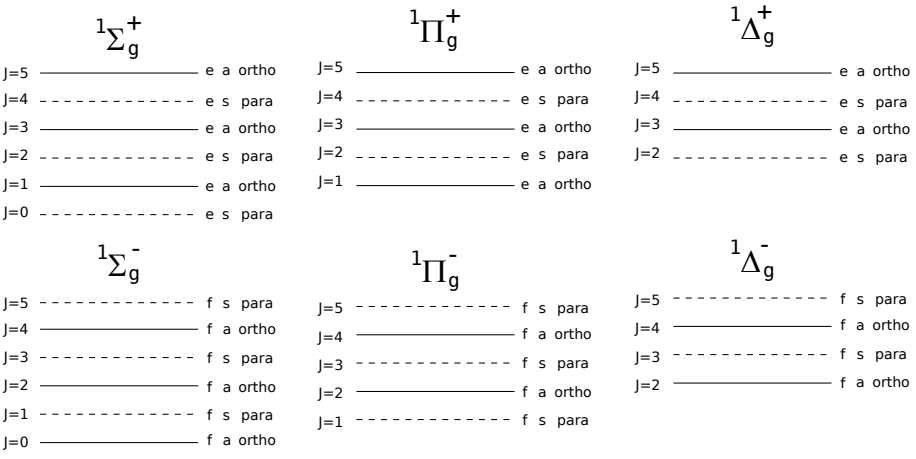

Figure 8.7: Symmetry labels for $^1\Sigma_g$, $^1\Pi_g$ and $^1\Delta_g$ electronic states in molecular hydrogen. Dashed lines represent levels with positive total parity, while solid lines represent levels with negative total parity.

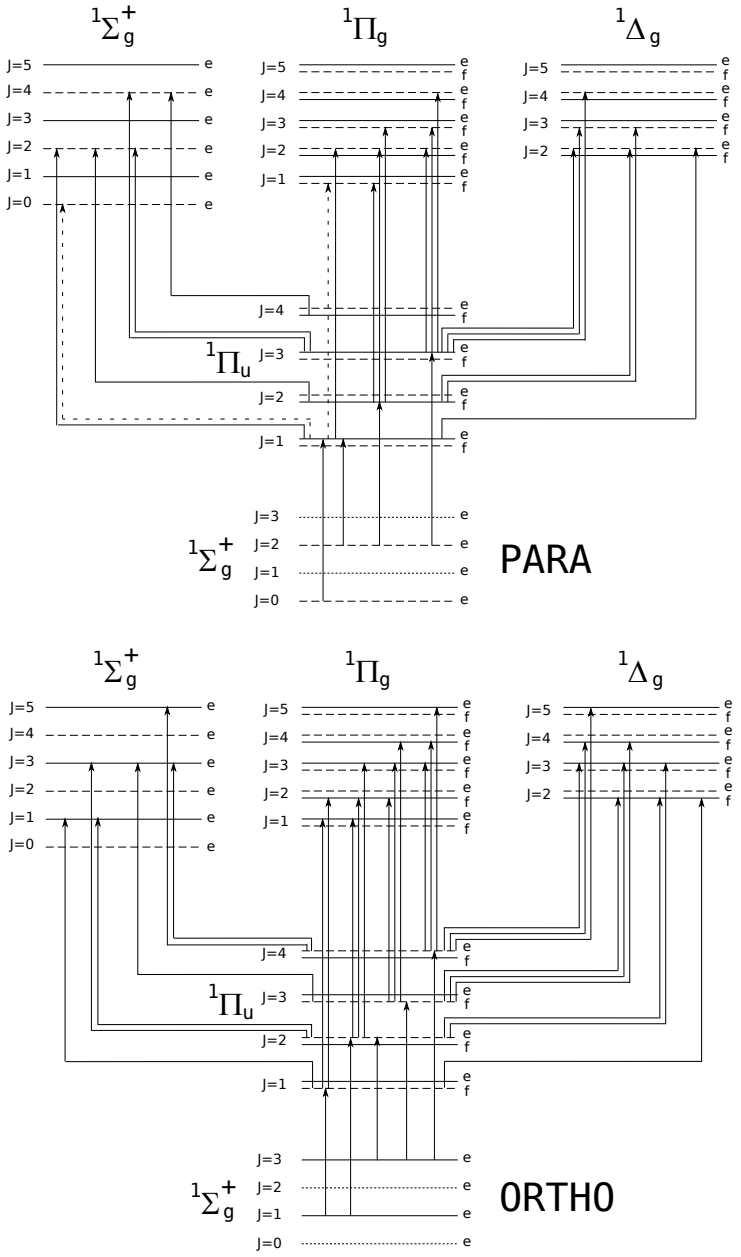

Figure 8.8: Selection rules for 1 XUV + 1 VIS double-resonance excitation. Dashed lines represent levels with positive total parity, while solid lines represent levels with negative total parity. All allowed electric-dipole transitions are indicated. The electric-dipole selection rules for the transitions depicted with dashed lines depend on the relative orientation of the polarization of the two photons.

The hydrogen molecule consists of two fermionic nuclei ($I = 1/2$), so the total wavefunction, including nuclear spin, should be antisymmetric with respect to the action of $\hat{P}_{12}$. It follows that all states with s parity can only combine with an antisymmetric nuclear wavefunction (para) and those with a parity can combine with a symmetric nuclear wavefunction (ortho). For the nuclear spin wavefunctions there are three combinations, associated with ortho-H_2, that are symmetric under exchange of the nuclear spins:

$$\begin{matrix} \alpha\alpha \\ \frac{1}{\sqrt{2}}(\alpha\beta + \beta\alpha) \\ \beta\beta \end{matrix} \tag{8.10}$$

and one combination, associated with para-H_2, that is antisymmetric:

$$\frac{1}{\sqrt{2}}(\alpha\beta - \beta\alpha) \tag{8.11}$$

where α and β denote spin-up and spin-down projections of the individual nuclear spins. All the symmetry labels for the states of interest in H_2 above the n=2 dissociation limit are shown in Fig. 8.7.

Selection rules for electric-dipole allowed transitions

The electric-dipole selection rules are determined by the requirement of a symmetric integrand for the transition moment integral

$$\langle \psi_f | \mu | \psi_i \rangle \tag{8.12}$$

Considering the total parities of the initial and final states, and the negative parity of the electric-dipole operator, the transition moment can only be nonzero for $+ \leftrightarrow -$ transitions. Using the same logic, $u \leftrightarrow g$ selection rule can be derived as a consequence of μ having u parity.

In addition, $s \leftrightarrow s$ and $a \leftrightarrow a$ or *para* $\leftrightarrow$ *para* and *ortho* $\leftrightarrow$ *ortho* selection rules are valid for electric-dipole transitions, because electronic transitions cannot simultaneously flip nuclear spins. It is, therefore, obvious that in the gas phase para- and ortho-hydrogen can be treated as completely separate species that cannot interconvert.

Fig. 8.8 shows the selection-rule diagram for 1 XUV + 1 VIS double-resonance excitation via C $^1\Pi_g(v' = 2, J')$. It is separated into para- and ortho- branches, since both species cannot mix. Note, that all e levels with even J can be accessed only in para-hydrogen and all e levels with odd J can be accessed only in ortho-hydrogen. Similar rules, are valid for the f states. This conclusion is very important, as we can easily identify the e/f parity by

just knowing the rotational quantum number J. It also tells us to look for rotational progressions, which alternate between para- and ortho-H_2 with changing J.

A great asset of 1 XUV + 1 VIS double-resonance excitation is that it allows for intermediate-state selection. Fig. 8.8 shows the different pathways to excite each final state. By comparing the dissociation spectra via different intermediate states, the rotational quantum number J can be retrieved for almost all spectroscopic features in the spectra.

The selection rules for the transitions depicted with a dashed line depend on the relative orientation of the polarization of the two photons. In the case of parallel polarization the transition $(J' = 1, m' = 0) \leftarrow (J'' = 1, m'' = 0)$ is not allowed, because the associated Clebsch-Gordon coefficient is zero. Perpendicular polarization dictates that $\Delta m = \pm 1$ and therefore the transition $(J' = 0, m' = 0) \leftarrow (J'' = 1, m'' = 0)$ is forbidden. These selection rules can be used as an extra tool for level identification.

Spectral assignment

The spectral assignment process combines J identification, symmetry considerations and extrapolation of the level structure starting from known level energies with lower vibrational quantum numbers in the bound region below the n=2 dissociation limit. The identification of rotational quantum numbers is carried out by comparing the dissociation traces associated with different intermediate states. For almost all spectroscopic features a reliable J quantum number can be derived. Only at the ends of the scans, when sometimes experimental information via all required intermediate states is missing, unique identification is difficult. Nevertheless, via extrapolations from the lower rotational states very often these gaps can be filled. The ortho-para alternation with changing J, explained in the previous section, simplifies the possibilities, while the odd/even J quantum number in the traces, associated with para- or ortho-hydrogen, provides further information on the rotationless parity of the states.

Extrapolation of the vibrational levels is carried out on the basis of the data in Ref. [135]. Since the vibrational levels are all associated with Rydberg states converging upon H_2^+ ($X\ ^2\Sigma_g^+$), the vibrational constant w_e in all states is similar and ~ 2300 cm^{-1}. When actual vibrational spacings are known, they are used. When information on vibrational anharmonicity is available, it is also included. The extrapolation process should lead to reasonable estimates of hitherto unobserved vibrational levels. In order to obtain an estimate for hitherto unobserved rotational levels, available data for lower rotational levels are simply extrapolated. Again, this procedure leads to reasonable estimates. Level perturbations sometimes complicate the issue. In such cases the width information can be helpful.

In the energy range $118500 - 120500$ cm^{-1}, there are a number of electronic

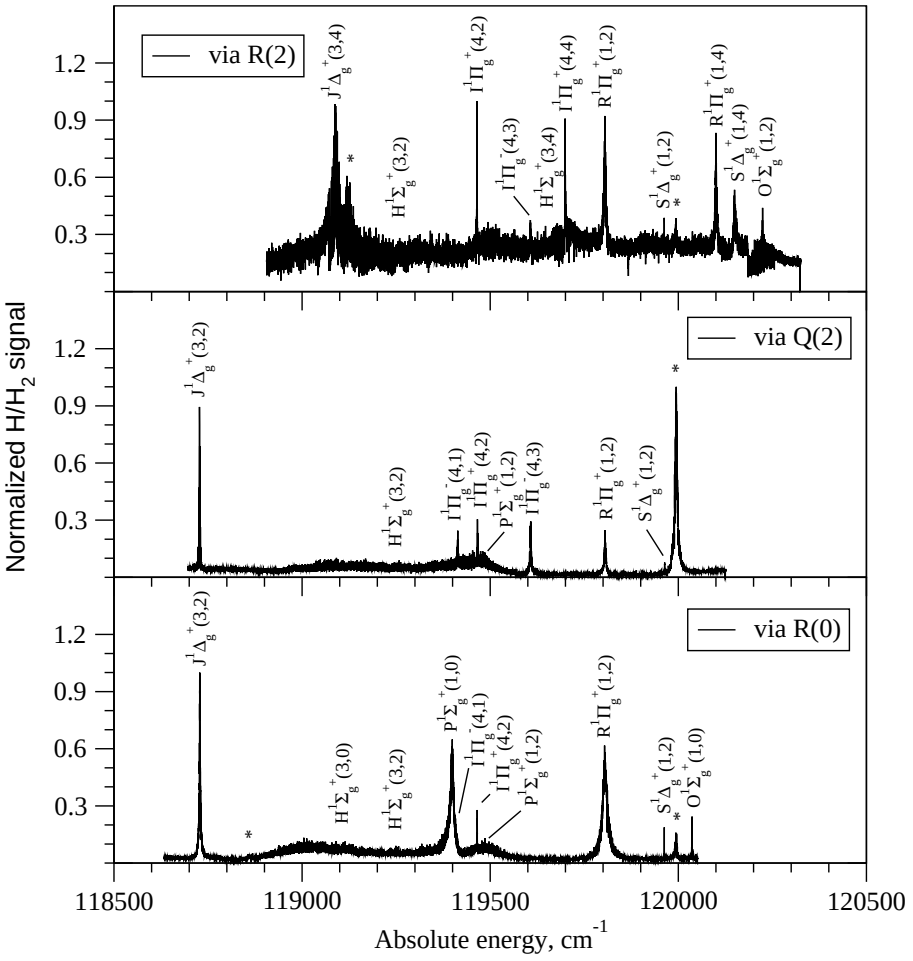

Figure 8.9: Dissociation traces of para-hydrogen produced by 1 XUV + 1 VIS + 1 UV. The horizontal axis represents the total term energy with respect to $X^1\Sigma_g^+$ $(v'' = 0, J'' = 0)$ reached by absorption of 1 XUV + 1 VIS.

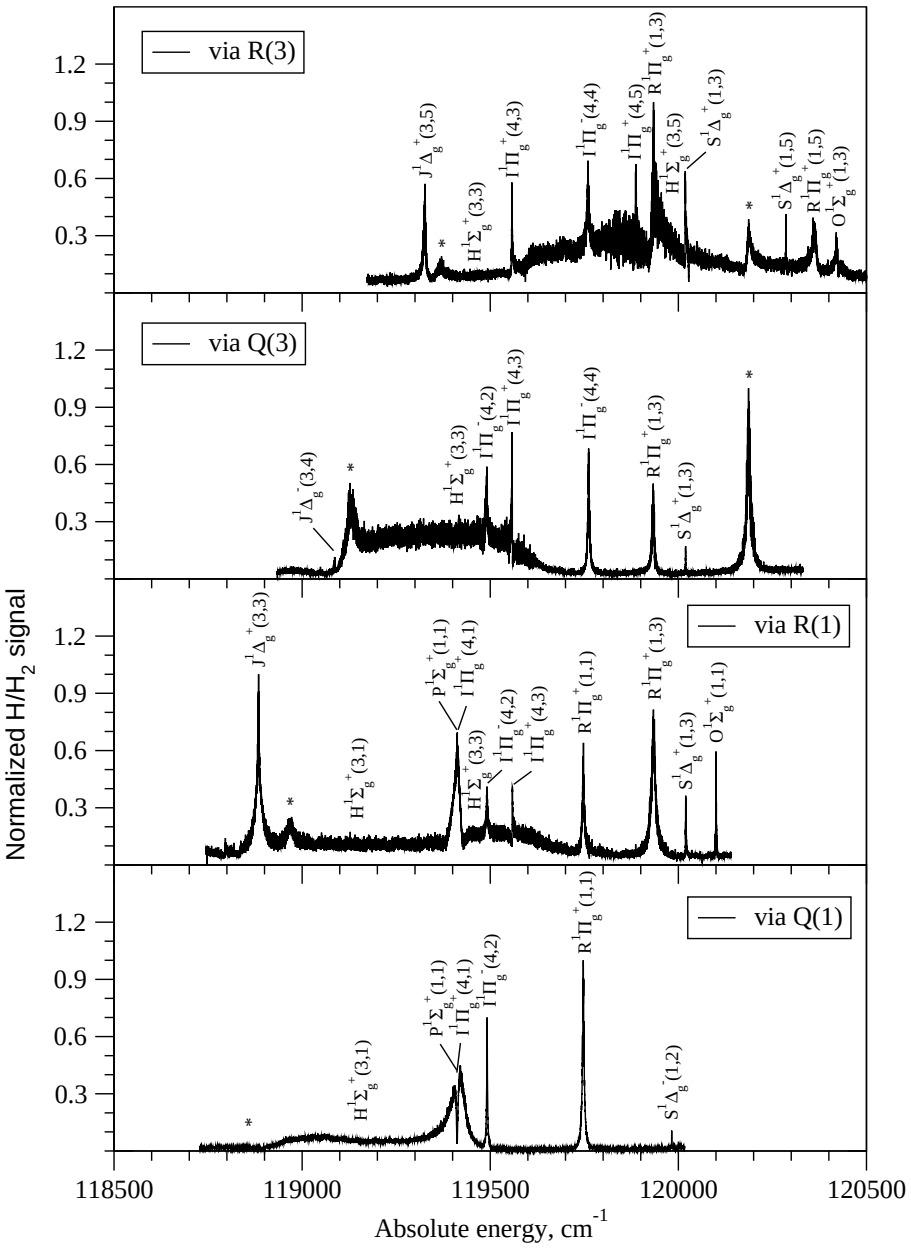

Figure 8.10: Dissociation traces of ortho-hydrogen produced by 1 XUV + 1 VIS + 1 UV. The horizontal axis represents the total term energy with respect to $X^1\Sigma_g^+$ $(v''=0, J''=0)$ reached by absorption of 1 XUV + 1 VIS.

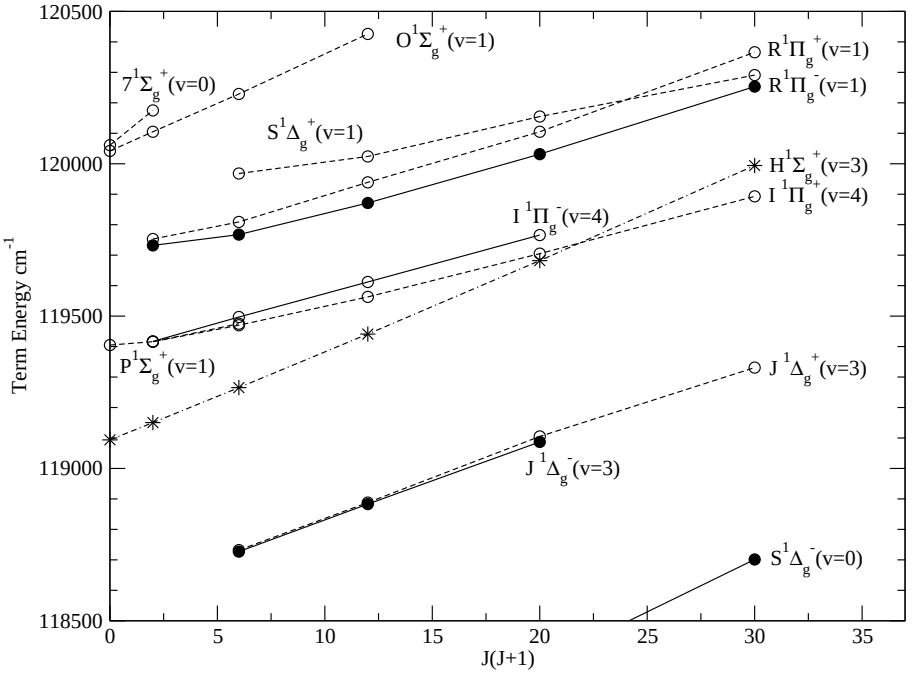

Figure 8.11: Rovibronic term values as a function of $J(J+1)$. Solid lines represent electronic states with negative rotationless parity, dashed lines - with positive parity. The data points indicated with solid circles are based on emission spectroscopy [4] and assigned in Ref. [135]. These transitions have also been observed in our H_2 traces within the estimated accuracy of 1 cm^{-1}. The open circles represent the term values extracted from the dissociation spectra. The stars depict the extrapolated rotational states of the H $^1\Sigma_g^+$ ($v' = 3$), which are too broad for a reliable term value determination.

states, which at short internuclear distances can be described as singly-excited Rydberg configurations that converge upon the H_2^+ ($X^2\Sigma_g^+$) ionic ground state. In particular, the I $^1\Pi_g$ ($3d\pi_g$) state, which at large internuclear distances correlates to the n=2 dissociation limit, H $^1\Sigma_g^+$ ($3s\sigma_g$), P $^1\Sigma_g^+$ ($4d\sigma_g$), O $^1\Sigma_g^+$ ($4s\sigma_g$), R $^1\Pi_g$ ($4d\pi_g$) and J $^1\Delta_g$ ($3d\delta_g$), which correlate to the n=3 dissociation limit, and S $^1\Delta_g$ ($4d\delta_g$), which correlates to the n=4 dissociation limit (Fig. 8.1) must be considered. Note that at larger internuclear distances interactions with repulsive states lead to very complicated potential energy curves. EF $^1\Sigma_g^+$, and GK $^1\Sigma_g^+$, both correlated to the n=2 dissociation limit, have no bound structure in the region studied and contribute only as a continuum. It should be noted, that they both have positive rotationless parity and therefore would contribute to continua with positive parity.

On the other hand the first continuum with negative parity in the *gerade* manifold, belonging to I $^1\Pi_g^-$, starts at 120300 cm^{-1} above the X $^1\Sigma_g^+$ ($v'' =$

$0, J'' = 0$) ground state. This is the energy of the top of the potential barrier, created by the avoided crossing of the Rydberg $(1s\sigma_g)(3d\pi_g)$ and the repulsive $(2p\sigma_u)(2p\pi_u)$ states (see Fig. 8.1). Below this energy there exist no continua with negative parity, which can interact with other bound electronic states with the same parity, thus opening a channel for predissociation. Therefore, it is not surprising that below 120300 cm^{-1} the electronic states with negative parity do not appear in our dissociation spectra. Instead these relatively long-lived states are observed as bound states and do appear in the H_2^+ traces; in particular the J $^1\Delta_g^-$ ($v' = 3$) and R $^1\Pi_g^-$ ($v' = 1$), which are also observed by classical emission spectroscopy [4]. The only mechanism for predissociation of bound electronic states with negative parity below this energy range involves tunneling of the bound I $^1\Pi_g^-$ state through the potential barrier. The tunneling rate increases with the effective decrease of the barrier for higher vibrational quantum numbers.

We can summarize, that the spectroscopic features related to states with negative parity are expected to be either missing in the lower energy range or to be relative narrow in the higher energy range below 120300 cm^{-1}.

Unlike the states with negative parity, the ones with positive parity interact with the existing continua of positive parity. Through this interaction they predissociate, thus creating H atoms. The reduced lifetimes in the bound states would appear in our dissociation spectra as line broadening. The characteristics of the electronic states determine the vibrational and rotational structure, as well as the lifetimes of the states. An example is H $^1\Sigma_g^+$, where strong interaction of the bound H $^1\Sigma_g^+$ ($v' = 3$) state with the repulsive $(2p\sigma_u)^2$ gives rise to enhanced predissociation and line broadening for all rotational states. Hence, similarities in linewidth can also be used as an additional tool for state identification.

The lineshapes of transitions to states with positive parity could be asymmetric to a certain extent due to their interaction with the existing continua with positive parity, leading to interference effects. Fitting such asymmetric Fano profiles in order to extract reliable parameters requires a very good S/N ratio. Especially sensitive is the asymmetry parameter q, which for a relatively symmetric lineshape can vary tremendously. For this reason reliable q parameters cannot be derived. Instead, only the linewidths of the transitions are extracted which are to be considered approximate. For the purpose of the assignment such approximate values are well suited.

Following these ideas the assignments in Table 8.1 are proposed. The linewidths of all transitions are also estimated in the table. Futher support for the assignments and discussion of the interaction processes involved are summarized state by state.

Table 8.1: Rovibronic term energy levels of the *gerade* states in the 118500 - 120500 cm^{-1} energy range and estimated linewidths. The accuracy of the term energy levels is 1 cm^{-1}, except for the H state, where the extrapolated values are presented

State	Position	FWHM	State	Position	FWHM
H $^1\Sigma_g^+$ $(v'=3)$			P $^1\Sigma_g^+$ $(v'=1)$		
$J'=0$	119094[1]	>100	$J'=0$	119405	10.5
$J'=1$	119150[1]	>100	$J'=1$	119416*	15
$J'=2$	119265[1]	>100	$J'=2$	119475	50
$J'=3$	119441[1]	>100			
$J'=4$	119682[1]	>100			
$J'=5$	119994[1]	>100			
O $^1\Sigma_g^+$ $(v'=1)$			S $^1\Delta_g^+$ $(v'=1)$		
$J'=0$	120042	1.2	$J'=2$	119968	0.3
$J'=1$	120105	2.2	$J'=3$	120024	1.3
$J'=2$	120229	1.0	$J'=4$	120155	6.6
$J'=3$	120426	8	$J'=5$	120291	0.8
J $^1\Delta_g^+$ $(v'=3)$			J $^1\Delta_g^-$ $(v'=3)$		
$J'=2$	118732	2.5	$J'=2$		
$J'=3$	118888	14.5	$J'=3$	118888	<0.3[e]
$J'=4$	119105	20	$J'=4$	119092	<0.3[e]
$J'=5$	119331	5.6			
I $^1\Pi_g^+$ $(v'=4)$			I $^1\Pi_g^-$ $(v'=4)$		
$J'=1$	119416*		$J'=1$	119417	1.8
$J'=2$	119470	0.8	$J'=2$	119497	2.7
$J'=3$	119563	1.5	$J'=3$	119612	3.6
$J'=4$	119705	1.2	$J'=4$	119766	5.8
$J'=5$	119893	1.9			
R $^1\Pi_g^+$ $(v'=1)$			R $^1\Pi_g^-$ $(v'=1)$		
$J'=1$	119753	5.8	$J'=1$		
$J'=2$	119809	5.8	$J'=2$	119768	<0.3[e]
$J'=3$	119939	13	$J'=3$	119872	<0.3[e]
$J'=4$	120105	4.1	$J'=4$	120032	<0.3[e]
$J'=5$	120366	11			

[1] Values based on extrapolation of the lower vibrational states

* These two levels coincide and are strongly mixed

[e] These levels are observed in the H_2^+ signal with linewidths determined by the instrument bandwidth. They are observed also in emission spectra in Ref. [4]

The H $^1\Sigma_g^+$ $(v'=3)$ state

The H $^1\Sigma_g^+$ electronic state has three vibrational levels below the n=2 dissociation limit. Extrapolation of the vibrational ladder shows that H $^1\Sigma_g^+(v'=3, J'=0)$ belonging to the fourth vibrational level is supposed to appear somewhere around 119100 cm^{-1}. However, the closest feature identified as a $J'=0$ state is at 119405 cm^{-1}, about 300 cm^{-1} above the predicted energy. Instead, at the predicted position there is a very broad feature spanning several hundred wavenumbers. Indeed, looking back in the potential energy diagram on Fig. 8.1 we can see that the perturbations of H $^1\Sigma_g^+$ due to the repulsive $(2p\sigma_u)^2$ state occur very close to the region where we expect the next vibrational level. Such interactions would result in enhanced predissociation rates leading to very broad lines. From the dissociation traces it is evident that such broad features appear also for the other rotational levels of H $^1\Sigma_g^+$ $(v'=3)$, following the ortho-para alternation. In Table 8.1 the presented values for H $^1\Sigma_g^+$ $(v'=3)$ are based on extrapolation of the lower vibrational states, as determination of a reliable line positions only from the spectra is difficult. The uncertainties for these values are much larger than 1 cm^{-1}. Another argument supporting the assignment of these broad features as belonging to the H $^1\Sigma_g^+$ $(v'=3)$ vibrational state, is the strongly asymmetric lineshapes of transitions belonging to other electronic states that happen to have the same rotational quantum number as the broad transitions. This can be seen in Fig. 8.9 and Fig. 8.10.

The P $^1\Sigma_g^+$ $(v'=1)$ state

This is one of the most complicated cases. The difficulty is related to the obvious perturbation of the adiabatic potential energy curve due to the avoided crossing with the repulsive $(2p\sigma_u)^2$ state. This will result in irregularities in the behaviour of the rovibronic states, which is hard to predict without advanced theoretical calculations including state-mixing. Nonetheless, an indication that a vibrational spacing smaller than usual should be expected can be extracted from the broader potential well of P $^1\Sigma_g^+$ above the perturbation. Considering that the P $^1\Sigma_g^+$ $(v'=0)$ state starts at 117454 cm^{-1} [135] and that a vibrational constant of about 2300 cm^{-1} is common for similar states, we should expect to find a $J'=0$ state below 119750 cm^{-1}. No other Σ states are expected in this region and indeed a $J'=0$ state is identified at 119405 cm^{-1} (see Fig. 8.9 - via R(0)).

For further verification this region is remeasured with perpendicular relative orientation of the polarizations of both exciting photons. Due to the polarization selection rules all $J'=0$ lines will be missing in this case. The comparison of both cases is given in Fig. 8.12. This is another independent verification that the feature at 119405 cm^{-1} is a $J'=0$ state, which we assign to be P $^1\Sigma_g^+$ $(v'=1, J'=0)$. The linewidth of this state is relatively large which indicates that the other rotational states belonging to P $^1\Sigma_g^+$ $(v'=1)$

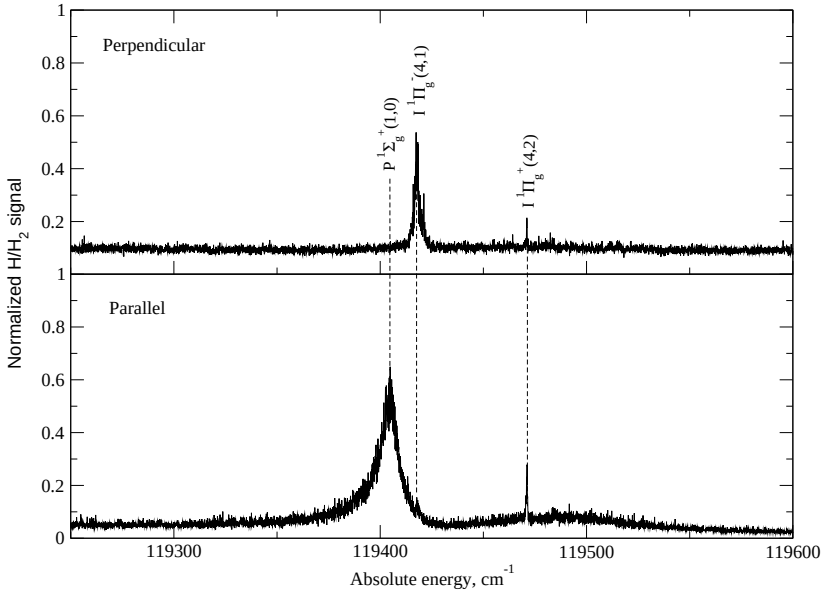

Figure 8.12: Dissociation spectra obtained by 1 XUV + 1 VIS two-photon excitation via the intermediate C $^1\Pi_u^+$ ($v' = 2, J' = 1$) state. In the upper trace the relative orientation of the polarizations of both excitation laser beams is perpendicular, while in the lower it is parallel. Polarization selection rules can also be used for J identification.

will also feature large linewidths.

Another rotational progression featuring narrow linewidths is clearly distinguished in the same energy region. A combination of vibrational extrapolation and comparison with I $^1\Pi_g^-$ ($v' = 4$) states shows that it belongs to the I $^1\Pi_g^+$ ($v' = 4$) state. The levels belonging to the P $^1\Sigma_g^+$ ($v' = 1$) and I $^1\Pi_g^+$ ($v' = 4$) electronic states can be disentangled based on their linewidths. Particularly interesting is the energy region, where the $J' = 1$ rotational levels belonging to both electronic states overlap. The resulting complex spectroscopic feature, shown in Fig. 8.10 indicates a strong level interaction. Therefore, in Table 8.1 only one value is presented for both transitions. The rotational progression of the P $^1\Sigma_g^+$ ($v' = 1$) state shows an unusually small rotational constant and strong rotationally dependent broadening, which leads to the disappearance of the states above $J' = 2$.

The O $^1\Sigma_g^+$ ($v' = 1$) state

An extrapolation process similar to the one adopted before in the assignment of P $^1\Sigma_g^+(v' = 1)$ shows that the second vibrational level of the O $^1\Sigma_g^+$ electronic state should appear around 120000 cm^{-1}. Approximately at this energy we

expect also the next $^1\Sigma_g^+$ state associated with one of the $(5l\sigma_g)$ Rydberg configurations (it is the 7 $^1\Sigma_g^+$ state). Indeed, two rotational progressions starting from $J' = 0$ were observed in this energy range (Fig. 8.11). Both of them feature similar linewidths and therefore the linewidth argument cannot be used to disentangle both states. However, the rotational progressions show different rotational constants. The first progression exhibits a small rotational constant, which is derived from four observed rotational levels ($J' = 0-3$). The second exhibits a higher rotational constant derived from only two observed rotational levels ($J' = 0, 1$). The latter ones are not included in Fig. 8.9 and Fig. 8.10, because they were observed during additional measurements performed at higher excitation energy.

Extrapolation of the rotational constant using the O $^1\Sigma_g^+$ ($v' = 0$) state is in reasonable agreement with the small value derived from the first progression. Another argument for assigning the first progression as belonging to O $^1\Sigma_g^+$ ($v' = 1$) is that it belongs to a higher vibrational state, which in principle should result in a smaller rotational constant. Certainly perturbations due to interactions with other states can affect the location of the rotational levels. However, due to insufficient experimental data in this region and the lack of theoretical calculations, the above assignment is somewhat tentative.

The I $^1\Pi_g$ ($v' = 4$) state

The states belonging to I $^1\Pi_g^-$ ($v' = 4$) are easy to identify. As discussed above, the states with odd J in the para- and the states with even J in the ortho-H_2 traces belong to electronic states with negative parity. Below the first continuum with negative parity emerging at around 120300 cm^{-1}, the only rotational progression with this pattern that can be found in the dissociation spectra belongs to I $^1\Pi_g^-$ ($v' = 4$). The other states with negative parity do not predissociate and are observed only in the H_2^+ spectra. The mechanism through which I $^1\Pi_g^-$ ($v' = 4$) predissociates involves tunneling through the potential barrier. For higher J states the effective barrier is smaller, leading to enhanced tunneling rates. Indeed, this effect can be observed in the increase of the linewidths for states with higher rotational quantum numbers (Fig. 8.13).

The assignment of the e states is described in the section concerning the P $^1\Sigma_g^+$ ($v' = 1$) state.

The R $^1\Pi_g$ ($v' = 4$) state

Similar to the I $^1\Pi_g$ ($v' = 4$) state, the long-lived emitting f states in R $^1\Pi_g$ ($v' = 4$) can be used to assign the e states. The states belonging to R $^1\Pi_g^-$ ($v' = 4$) are tabulated in Ref. [135] and were observed in our spectra detecting H_2^+. Finding a matching $^1\Pi_g^+$ rotational progression in this energy range is more complicated, because of the states nearby. Fortunately, the R $^1\Pi_g^+$ and S $^1\Delta_g^+$ progressions can be disentangled according to their linewidths. The one with

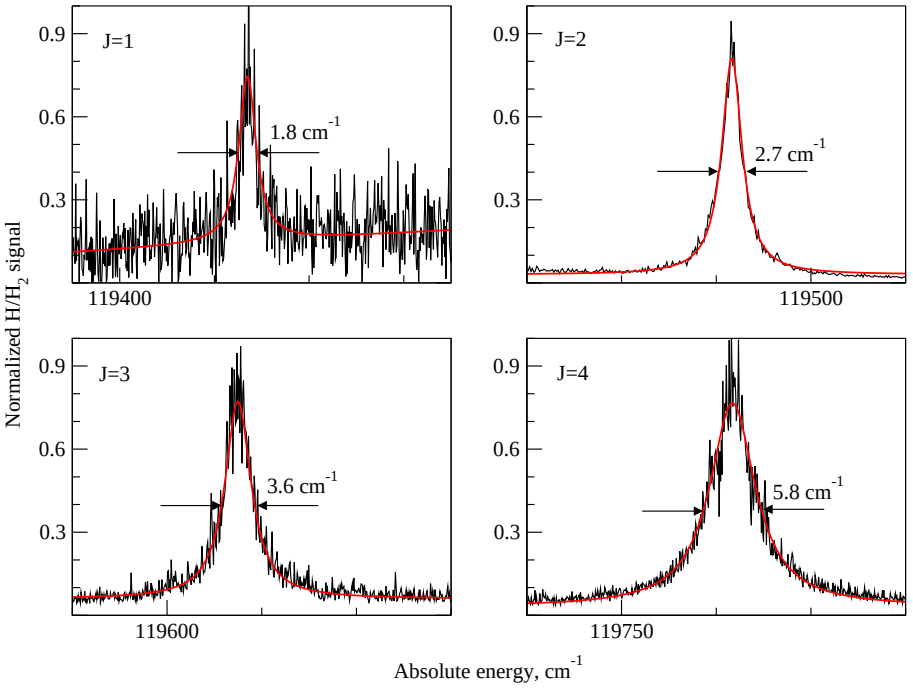

Figure 8.13: Rotational states belonging to I $^1\Pi_g^-$ $(v' = 4)$. The mechanism causing their predissociation involves tunneling through the potential barrier (see Fig. 8.1). For higher J states the effective barrier is smaller, leading to enhanced tunneling rates, which can be observed as increasing linewidths.

the narrow linewidth starts from $J' = 2$ and, therefore, belongs to a Δ state. The broader one, starting from $J' = 1$, then belongs to R $^1\Pi_g^+$ $(v' = 4)$. An avoided crossing between the two progressions at $J' = 4$ can be observed. This results in line broadening in the progression consisting of narrow lines and in line narrowing in the progression consisting of broad lines.

The J $^1\Delta_g$ $(v = 3)$ state

Identifying this state is analogous to the procedure used with R $^1\Pi_g$ $(v' = 4)$. Knowing the f states from the emission spectra [135] it is evident which are the e states as the Λ-doubling is small in Δ states, because it is a second-order effect.

The S $^1\Delta_g$ $(v' = 1)$ state

The f states belonging to the S $^1\Delta_g$ $(v' = 1)$ state are already close to the onset of the first negative continuum, providing a mechanism for predissociation. Since these levels are not reported as emitting lines in Ref. [135] they

might exist as predissociating states. Actually, we may have observed the S $^1\Delta_g^-$ ($v' = 1, J' = 2$) state as an extremely narrow line at 119987 cm^{-1} in the dissociation trace via C $^1\Pi_u$ ($v' = 2$) Q1. However, the presence of this line has not been confirmed in any other dissociation trace. The reasoning behind this tentative assignment is that there are two states with rotational quantum number $J' = 2$ in the dissociation traces associated with para-hydrogen, one of which belongings to S $^1\Delta_g^+$ ($v' = 1$). Since the Λ-doubling is small in Δ states, the S $^1\Delta_g^-$ ($v' = 1, J' = 2$) state should appear as a narrow line approximately at the same energy in the spectra associated with ortho-hydrogen. The observed feature at 119987 cm^{-1} matches this description and cannot be explained as belonging to other known states in this energy range.

The narrow progression discussed in the section on R $^1\Pi_g$ ($v' = 4$) is assigned as belonging to S $^1\Delta_g^+$ ($v' = 1$). However, this assignment is not very firm, because of the unusually low rotational constant. Another very strong $J' = 2$ line at 119999 cm^{-1} indicates the beginning of a new progression, which seems to have a rotational constant similar to that of S $^1\Pi_g$ ($v' = 0$), but there is not sufficient information for a definite conclusion.

Unassigned lines

There exist a few lines without assignment marked with asterisks in Fig. 8.9 and Fig. 8.10. Some of them have very low intensities and may be spurious. There are no unassigned electronic states below 119500 cm^{-1} that could explain any of these states. The transition marked on the dissociation trace via R(1) is not reproducible, which indicates that it can be an artifact. We speculate that these features relate to higher lying dissociative resonances probed via multiphoton excitation from the intermediate C $^1\Pi_u$ ($v' = 2$) state.

More interesting are the lines at 119999 cm^{-1} with identified $J' = 2$ rotational quantum number, and at 120192 cm^{-1} with possibilities $J' = 3$ or $J' = 4$. These observed and unassigned lines might be the start of a rotational progression associated with a Δ state or even belong to S $^1\Delta_g^+$ ($v' = 1$). At this energy the electronic states associated with the ($5l\Lambda_g$) Rydberg configurations are expected to appear. The present experimental information is insufficient for any firm conclusion.

8.4 Conclusions

The resonance structure in the singlet-gerade manifold of the hydrogen molecule was experimentally observed with 1 XUV + 1 UV two-photon excitation and by monitoring the H(n=2) dissociation fragments. Spectral features with linewidths from one to several hundred cm^{-1} are recorded in the energy range of $118500 - 120500$ cm^{-1}. The state-selective excitation process imposes restrictions on the selection rules, which together with the para-ortho selection in the first excitation step can be exploited as a tool for identification of the

rotational quantum numbers and the parity of the states. Combining J identification, symmetry considerations and extrapolation of the level structure starting from known level energies in the bound region below the n=2 dissociation limit, most of the broad dissociative resonances in the energy region can be assigned.

8.5 Acknowledgment

The author gratefully acknowledges Dr. E. Reinhold for helpful discussions.

XUV spectroscopie van hoogaangeslagen toestanden in H_2, HD and D_2

De ontdekking van waterstof als element en als molecuul bestaand uit twee atomen, is verbonden met de namen van de wetenschappelijke pioniers Cavendish, Lavoisier, Gay-Lussac en Avogadro. In de negentiende eeuw werd waterstof bestudeerd met spectroscopen. Naast de lijnen van atomaire waterstof in het zichtbare spectrum, later bekend als de Balmerreeks, werden in een vroeg stadium al enkele andere lijnen gezien. Deze lijnen werden benoemd als het tweede spectrum van waterstof. De eerste spectroscopische waarnemingen die spectraallijnen onomstotelijk toekenden aan moleculaire waterstof werden meer dan een eeuw geleden gedaan door Lyman [1]. Deze ontdekking kon alleen worden gedaan door de ontwikkeling van spectroscopische technieken voor het vacuümultraviolet. In onze studies aan het spectrum van waterstof zijn we nog steeds afhankelijk van deze technieken. In verschillende spectroscopische studies maken we gebruik van het smalbandige en afstembare Amsterdams eXtreem UltraViolet (XUV) laser systeem. Deze opstelling kan worden gebruikt in hoge resolutie, scannende spectroscopie studies, maar van het gepulste karakter van de laser kan ook gebruik worden gemaakt in dubbelresonantiestudies aan het waterstofmolecuul en zijn isotopen. Door het gebruik van meerdere overlappende laserpulsen kan de aangeslagen toestandsstructuur van het molecuul worden waargenomen, zelfs voor gekwantiseerde toestanden die niet toegankelijk zijn vanuit de grondtoestand (om verschillende redenen: dipool-verboden overgangen, slechte golffunctieoverlap). De combinatie van lasers met time-of-flight massascheiding en snelheidsafbeeldingstechnieken, waarvan de implementatie ook in dit proefschrift wordt besproken, maken meer gedetailleerde metingen mogelijk, specifiek die van de dissociatiedynamica van enkele hoogaangeslagen toestanden van het molecuul. Naast lasers is ook gebruik gemaakt van een nieuw en uniek instrument, de vacuümultraviolet Fouriertransform-spectrometer, aan het Soleil synchrotron.

De motivatie voor ons onderzoek komt uit verschillende invalshoeken, van astrofysica via de molecuulfysica tot aan de fundamentele natuurkunde. Mole-

culaire waterstof is veruit het meest voorkomende molecuul in het heelal. Desalniettemin werd H_2 lange tijd niet waargenomen in het interstellaire medium, omdat zijn dipooltoegestane absorptiespectrum in het vacuümultraviolet ligt, waarvoor de aardse atmosfeer niet transparant is. Er was een door een raket gedragen spectrometer nodig voor de eerste observatie. De waarneming van moleculaire waterstof in zwakke objecten met een hoge roodverschuiving via op aarde gesitueerde telescopen gaf een nieuwe impuls aan het onderzoeksveld en was de aanleiding voor het bestuderen van het H_2 spectrum met de hoogst mogelijke resolutie. Doel is de zoektocht naar de variatie van de fundamentele dimensieloze natuurconstante μ (de proton-elektron massaverhouding) op kosmologische tijdschaal [2]. Ook de spectra van HD worden meegenomen in deze studies [3].

Naast de motivatie vanuit astronomische en fundamenteel natuurkundige hoek, heeft het bestuderen van de kwantumstructuur van de kleinste neutrale moleculaire entiteit een intrinsieke waarde. Ondanks een eeuw spectroscopisch onderzoek zijn vele aspecten van de moleculaire toestandsstructuur van H_2 nog steeds niet begrepen. Dit wordt geïllustreerd door het feit dat de meerderheid van de waargenomen spectrale lijnen van moleculaire waterstof in de *Dieke Atlas* [4] niet is toegekend. Daarnaast blijft de variëteit van dissociatieve toestanden en specifiek die van singlet *gerade* symmetrie, wat betreft toewijzingen een onontgonnen terrein. Onze studie naar deze dissociatieve toestanden net boven de n=2 dissociatielimiet is een poging om deze situatie te verbeteren.

Zelfs als een onderwerp meer dan een eeuw is bestudeerd zijn er nog verrassingen mogelijk. Een van deze verrassingen is onze ontdekking en identificatie van een in frequentie opgeloste Rydbergreeks in het zware H^+H^- Rydbergsysteem. De waarneming van de zware Rydbergreeks in H^+H^- legt een nieuw onderzoeksveld open, omdat zulke kwantumtoestanden in elk molecuul zouden moeten bestaan.

Overzicht

Dit proefschrift beschrijft experimenteel onderzoek aan moleculaire waterstof en zijn isotopen.

In hoofdstuk 2 wordt HD voorgesteld als testsysteem in de zoektocht naar een mogelijke variatie van de proton-elektron massaverhouding. De spectroscopische signatuur van deze op een na meest aanwezige waterstofisotoop is reeds in verschillende quasarspectra met hoge roodverschuiving waargenomen [3]. Op dit moment is de waarneming in de volgende quasarsystemen gerapporteerd: Q1232+082, Q0528-250, FJ0812+320, J2123-050, J1237+064 en Q1439+113. Laboratorium waarnemingen van de meest prominente HD lijnen met een relatieve nauwkeurigheid van 5×10^{-8} zijn gedaan met behulp van het smalbandige en verstembare XUV lasersysteem. Daarnaast zijn gevoeligheidscoëfficienten als functie van van de proton-elektron massaverhouding bepaald met

behulp van *ab initio* kwantumchemische berekeningen. Deze resultaten zijn voldoende nauwkeurig zodat ze kunnen worden meegenomen in een volledige statistische analyse samen met de data van H_2. Een belangrijke eigenschap van HD is de aanwezigheid van een neutron in de kern. Strategieën om mogelijke effecten voorbij de eerste orde baryon/lepton massaverhouding af te leiden worden behandeld.

Hoofdstuk 3 breidt het overzicht van de HD lijnen uit waarmee in hoofdstuk 2 werd begonnen. Voor het eerst werd de nieuwe Fourier transformatie spectrometer, een permanent eindstation van de DESIRS bundellijn aan het SOLEIL synchrotron, gebruikt om met golflengten in het XUV spectroscopie te bedrijven aan HD. De HD spectraallijnen in de Lyman- en Werner-banden werden in een vensterloze configuratie gemeten in het bereik van 87-112 nm. De golflengtes van 268 lijnen in de $B^1\Sigma_u^+\,(v'=0-30) \leftarrow X^1\Sigma_g^+\,(v''=0)$ Lyman systeem en 141 lijnen in de $C^1\Pi_u(v'=0-10) \leftarrow X^1\Sigma_g^+(v''=0)$ Werner systeem konden worden bepaald met een nauwkeurigheid van 0.04 cm^{-1} (1σ) hetgeen overeenkomt met $\Delta\lambda/\lambda \sim 4\times10^{-7}$. De resultaten van het vorige hoofdstuk werden gebruikt om de interne kalibratie van deze unieke opstelling te beproeven en te verbeteren.

In hoofdstuk 4 wordt een lacune in het overzicht van H_2 opgevuld. Vanwege vroegere problemen met het genereren van de juiste golflengten met de smalbandige extreemultraviolet laser, ontbrak de $B^1\Sigma_u^+ - X^1\Sigma_g^+$ (6,0) Lymanband uit het H_2 spectrum nog in het overzicht van laboratoriummetingen. Deze overgangen werden toegankelijk gemaakt door het gebruik van een exotisch kleurstof mengsel, hetwelk het verstembare bereik van het XUV laser systeem vergrootte, door het lastige 615-620 nm golflengtegebied af te dekken. Dit mengsel werd tevens gebruikt voor het kalibreren van de $(^4S^o)$ 3d $^3D_J^o \leftarrow {}^3P_J$ overgangen in atomaire zuurstof [5].

Hoofdstuk 5 beschrijft de kalibratie van 39 lijnen in de $B^1\Sigma_u^+$ - $X^1\Sigma_g^+(v',0)$ Lymanbanden voor $v'=9-11$, en in de $C^1\Pi_u$ - $X^1\Sigma_g^+(0,0)$ Wernerband van het D_2 molecuul. Deze werden, gebruikmakend van een smalbandige verstembare extreem ultraviolet laser, gemeten met een relatieve nauwkeurigheid van $\Delta\lambda/\lambda = 6\times10^{-8}$. Deze resultaten zijn relevant voor toekomstig gebruik in de kalibratie van spectra met een hoge lijndichtheid van de HD en D_2 isotopen.

Hoofdstuk 6 beschrijft de eerste waarneming van Rydbergtoestanden in het bijzondere H^+H^- systeem. Dit systeem is interessant omdat het door de grote internucleaire afstand beschouwd kan worden als een systeem bestaand uit twee puntvormige geladen deeltjes gebonden door de Coulomb potentiaal. Deze beschrijving is formeel gelijk aan het goed bekende Bohratoom en zou daarom de zelfde karakteristieke lijnstructuur moeten bezitten, zij het geschaald met de gereduceerde massa van het systeem. Ongelukkigerwijs voorkomen de Frank-Condon beperkingen het direct bereiken van deze toestanden. Desalniettemin zijn spectroscopische signaturen van deze zware Rydbergtoestanden, voorspeld door de Rydbergvergelijking voor dit zware Rydbergatoom, wel degelijk waar-

genomen. Dit opmerkelijke resultaat is bereikt, dankzij de complexe interactie van brede moleculaire Rydbergtoestanden op kleine internucleaire afstanden met de zware Rydbergtoestanden op grotere internucleaire afstanden, welke resulteert in de populatie van H^+H^- niveaus. Een van de mogelijke vervalkanalen van deze ionenpaar toestanden heeft betrekking op autoionisatie en creatie van H_2^+ ionen, welke we detecteren als een serie brede resonanties voldoend aan de zware Rydbergvergelijking.

Hoofdstuk 7 bericht over de ontwikkeling van een zogenaamde VMI detector, waarmee snelheden van dissociatiefragmenten kunnen worden afgebeeld. Deze detector is toegevoegd aan de bestaande XUV-laser opstelling. De prestaties en enkele voorlopige resultaten worden besproken, alhoewel het systeem nog in ontwikkeling is. Tot nu toe laten de beste focusseringsresultaten een ruimtelijk oplossend vermogen van 400 μm zien, hetgeen aangeeft dat het systeem zijn optimale prestaties nog niet heeft bereikt. Dit komt door enkele inherente beperkingen in de huidige opstelling. Het produceren van XUV licht met behulp van niet-lineaire optische technieken in een gasbundel genereert divergente XUV straling, welke zorgt voor een relatief groot interactiegebied. Dit is een cruciale tekortkoming voor het behalen van goede prestaties met een VMI systeem. Andere beperkingen worden in detail beschreven en er worden mogelijkheden tot verbetering voorgesteld. De combinatie van een XUV laser systeem, met smalbandige toestandsselectieve excitatie, en VMI detectie van geïoniseerde fragmenten zou geweldige mogelijkheden creëren in het bestuderen van de dissociatieve dynamica van kleine moleculen met spectroscopische details in het XUV bereik.

In hoofdstuk 8 wordt de *gerade* elektronische structuur van moleculair waterstof boven de n=2 dissociatielimiet bestudeerd met behulp van tweestapsexcitatie door XUV en zichtbaar licht (1 + 1). Spectrale eigenschappen in het golflengtegebied van 118500–120500 cm^{-1} laten lijnbreedtes ziet tussen één en enkele honderden cm^{-1}, door het meten van laser-ionisatie van H(n=2) brokstukken ontstaan in het dissociatieproces. Het goed gecontroleerde tweestapsexcitatieproces, gecombineerd met massaselectieve detectie, legt beperkingen op aan de mogelijk te bereiken kwantumtoestanden. Door het toepassen van impulsmomentselectieregels en gebruikmakend van het onderscheid tussen para- en ortho-waterstof, konden de predissociatie resonanties van de *gerade* inversiesymmetrie van H_2 worden geïdentificeerd in termen van elektronisch symmetrie en rotatievibrationele kwantumgetallen. Op deze manier kunnen de meeste van de brede dissociatieve resonanties in het golflengtebereik worden toegekend.

Bibliography

[1] T. Lyman, *The spectrum of hydrogen in the region of extremely short wave-lengths*, Astrophysical Journal. **23**, 181 (1906).

[2] R. I. Thompson, *Determination of electron to proton inertial mass ratio via molecular transitions*, Astrophysical Letters & Communications **16**, 3 (1975).

[3] D. A. Varshalovich, A. V. Ivanchik, P. Petitjean, R. Srianand, and C. Ledoux, *HD molecular lines in an absorption system at redshift z=2.3377*, Astronomy Letters **27**, 683 (2001).

[4] H. M. Crosswhite, *The hydrogen molecule wavelength tables of Gerhard Heinrich Dieke* (Wiley-Interscience, 1972).

[5] T. I. Ivanov, E. J. Salumbides, M. O. Vieitez, P. C. Cacciani, C. A. de Lange, and W. Ubachs, *Extreme-ultraviolet laser metrology of O I transitions*, Monthly Notices of the Royal Astronomical Society **389**, L4 (2008).

[6] M. T. Murphy, J. K. Webb, and V. V. Flambaum, *Further evidence for a variable fine-structure constant from Keck/HIRES QSO absorption spectra*, Monthly Notices of the Royal Astronomical Society **345**, 609 (2003).

[7] E. Reinhold, R. Buning, U. Hollenstein, A. Ivanchik, P. Petitjean, and W. Ubachs, *Indication of a cosmological variation of the proton-electron mass ratio based on laboratory measurement and reanalysis of H_2 spectra*, Physical Review Letters **96**, 151101 (2006).

[8] W. Ubachs, R. Buning, K. S. E. Eikema, and E. Reinhold, *On a possible variation of the proton-to-electron mass ratio: H_2 spectra in the line of sight of high-redshift quasars and in the laboratory*, Journal of Molecular Spectroscopy **241**, 155 (2007).

[9] A. Ivanchik et al., *A new constraint on the time dependence of the proton-to-electron mass ratio - Analysis of the Q 0347-383 and Q 0405-443 spectra*, Astronomy & Astrophysics **440**, 45 (2005).

[10] V. V. Flambaum and M. G. Kozlov, *Limit on the cosmological variation of m_p/m_e from the inversion spectrum of ammonia*, Physical Review Letters **98**, 240801 (2007).

[11] J. Barrow, *The constants of nature* (Vintage Books, New York, 2002).

[12] J. D. Barrow, H. B. Sandvik, and J. Magueijo, *Behavior of varying-alpha cosmologies*, Physical Review D **65**, 063504 (2002).

[13] I. Dabrowski and G. Herzberg, *The absorption and emission spectra of HD in the vacuum ultraviolet*, Canadian Journal of Physics **54**, 525 (1976).

[14] V. V. Meshkov, A. V. Stolyarov, A. V. Ivanchik, and D. A. Varshalovich, *Ab initio nonadiabatic calculation of the sensitivity coefficients for the $X\,^1\Sigma_g^+ \rightarrow B^1\Sigma_u^+$; $C^1\Pi_u$ lines of H_2 to the proton-to-electron mass ratio*, JETP Letters **83**, 303 (2006).

[15] W. Ubachs and E. Reinhold, *Highly accurate H_2 Lyman and Werner band laboratory measurements and an improved constraint on a cosmological variation of the proton-to-electron mass ratio*, Physical Review Letters **92**, 101302 (2004).

[16] U. Hollenstein, E. Reinhold, C. A. de Lange, and W. Ubachs, *High-resolution VUV-laser spectroscopic study of the $B^1\Sigma_u^+(v' = 0-2) \leftarrow X^1\Sigma_g^+(v'' = 0)$ Lyman bands in H_2 and HD*, Journal of Physics B **39**, L195 (2006).

[17] T. G. P. Pielage, A. de Lange, F. Brandi, and W. Ubachs, *Bound energy levels at the n=2 dissociation threshold in HD*, Chemical Physics Letters **366**, 583 (2002).

[18] P. Hinnen, S. Werners, S. Stolte, W. Hogervorst, and W. Ubachs, *XUV-Laser spectroscopy of HD at 92-98 nm*, Physical Review A **52**, 4425 (1995).

[19] L. Ulivi, P. de Natale, and M. Inguscio, *Pure rotational spectrum of hydrogen deuteride by far-infrared Fourier transform spectroscopy*, Astrophysical Journal **378**, L29 (1991).

[20] M. Roudjane, F. Launay, and W.-U. L. Tchang-Brillet, *High resolution vacuum ultraviolet emission spectrum of D_2 from 78 to 103 nm: The $D\,^1\Pi_u \rightarrow X\,^1\Sigma_g^+$ and $D'\,^1\Pi_u^- \rightarrow X\,^1\Sigma_g^+$ band systems*, Journal of Chemical Physics **125**, 214305 (2006).

[21] G. Staszewska and L. Wolniewicz, *Adiabatic energies of excited $^1\Sigma_u$ states of the hydrogen molecule*, Journal of Molecular Spectroscopy **212**, 208 (2002).

[22] L. Wolniewicz and G. Staszewska, *Excited* $^1\Pi_u$ *states and the* $^1\Pi_u \rightarrow X^1\Sigma_g^+$ *transition moments of the hydrogen molecule*, Journal of Molecular Spectroscopy **220**, 45 (2003).

[23] L. Wolniewicz and K. Dressler, *The* $B\,^1\Sigma_u^+$, $B'\,^1\Sigma_u^+$, $C\,^1\Pi_u$, *and* $D\,^1\Pi_u$ *states of the* H_2 *molecule. Matrix elements of angular and radial nonadiabatic coupling and improved* ab initio *potential energy curves*, Journal of Chemical Physics **88**, 3861 (1988).

[24] P. Senn, P. Quadrelli, and K. Dressler, *The* $B\,^1\Sigma_u^+$, $B'\,^1\Sigma_u^+$,$C\,^1\Pi_u$, *and* $D\,^1\Pi_u$ *states of hydrogen. Ab initio calculation of rovibronic coupling in* H_2, *HD, and* D_2, Journal of Chemical Physics **89**, 7401 (1988).

[25] L. Wolniewicz, *Relativistic energies of the ground state of the hydrogen molecule*, Journal of Chemical Physics **99**, 1851 (1993).

[26] L. Wolniewicz, *Nonadiabatic energies of the ground state of the hydrogen molecule*, Journal of Chemical Physics **103**, 1792 (1995).

[27] C. Schwartz and R. J. L. Roy, *Nonadiabatic eigenvalues and adiabatic matrix elements for all isotopes of diatomic hydrogen*, Journal of Molecular Spectroscopy **121**, 420 (1987).

[28] A. de Lange, E. Reinhold, and W. Ubachs, *Phenomena of g-u symmetry-breakdown in HD*, International Reviews In Physical Chemistry **21**, 257 (2002).

[29] J. D. Alemar-Rivera and A. L. Ford, *Nonadiabatic effects in the B, C and E, F states of HD*, Journal of Molecular Spectroscopy **67**, 336 (1977).

[30] P. J. Mohr and B. N. Taylor, *CODATA recommended values of the fundamental physical constants: 2002*, Reviews of Modern Physics **77**, 1 (2005).

[31] T. Dent, *Composition-dependent long range forces from varying* m_p/m_e, Journal of Cosmology and Astroparticle Physics **01**, 013 (2007).

[32] G. Carruthers, *Rocket observation of interstellar molecular hydrogen*, Astrophysical Journal **161**, L81 (1970).

[33] M. Aaronson, B. J.H., and M. C.F., *A search for molecular hydrogen in quasar absorption spectra*, Astrophysical Journal **191**, L53 (1974).

[34] R. Carlson, *Molecular hydrogen absorption features in the spectrum of quasi-stellar object 4C 05.34*, Astrophysical Journal **190**, L99 (1974).

[35] P. Noterdaeme, P. Petitjean, C. Ledoux, R. Srianand, and A. Ivanchik, *HD molecules at high redshift*, Astronomy & Astrophysics **491**, 397 (2008).

[36] A. L. Malec et al., *Keck telescope constraint on cosmological variation of the proton-to-electron mass ratio*, Monthly Notices of the Royal Astronomical Society **403**, 1541 (2010).

[37] T. I. Ivanov, M. Roudjane, M. O. Vieitez, C. A. de lange, W. U. L. Tchang-Brillet, and W. Ubachs, *HD as a probe for detecting mass variation on a cosmological time scale*, Physical Review Letters **100**, 093007 (2008).

[38] G. M. Greetham, U. Hollenstein, R. Seiler, W. Ubachs, and F. Merkt, *High-resolution VUV photoionization spectroscopy of HD between the* $X\ ^2\Sigma_g^+\ \nu^+ = 0$ *and* $\nu^+ = 1$ *thresholds*, Physical Chemistry Chemical Physics **5**, 2528 (2003).

[39] J. A. King, J. K. Webb, M. T. Murphy, and R. F. Carswell, *Stringent null constraint on cosmological evolution of the proton-to-electron mass ratio*, Physical Review Letters **101**, 251304 (2008).

[40] *http://www.synchrotron-soleil.fr/portal/page/portal/Recherche/LignesLumiere/DESIRS.*

[41] A. Thorne, *Fourier transform spectrometry in the vacuum ultraviolet: applications and progress*, Physica Scripta **T65**, 31 (1996).

[42] N. de Oliveira, D. Joyeux, D. Phalippou, J. C. Rodier, F. Polack, M. Vervloet, and L. Nahon, *A Fourier transform spectrometer without a beam splitter for the vacuum ultraviolet range: From the optical design to the first UV spectrum.*, Review of Scientific Instruments **80**, 043101 (2009).

[43] N. de Oliveira, M. Roudjane, D. Joyeux, D. Phalippou, J. C. Rodier, and L. Nahon, *High resolution broadband Fourier transform absorption spectroscopy in the VUV range*, Nature Photonics (submitted july 2010).

[44] N. D. Oliveira, D. Joyeux, D. Phalippou, J. C. Rodier, L. Nahon, F. Polack, and M. Vervloët, *A high precision scanning control system for a VUV Fourier transform spectrometer*, AIP Conference Proceedings **879**, 447 (2007).

[45] O. Marcouille et al., *Design, construction and magnetic measurements of the HU640 (OPHELIE2) undulator dedicated to the DESIRS VUV beamline at SOLEIL*, AIP Conference Proceedings **879**, 311 (2007).

[46] B. Mercier, M. Compin, C. Prevost, G. Bellec, R. Thissen, O. Dutuit, and L. Nahon, *Experimental and theoretical study of a differentially pumped absorption gas cell used as a low energy-pass filter in the vacuum ultraviolet photon energy range*, Journal of Vacuum Science & Technology A **18**, 2533 (2000).

[47] M. Sommavilla, U. Hollenstein, G. M. Greetham, and F. Merkt, *High-resolution laser absorption spectroscopy in the extreme ultraviolet*, Journal of Physics B **35**, 3901 (2002).

[48] S. Davis, M. Abrams, and J. Brault, *Fourier transform spectrometry* (Academic Press, 2001).

[49] P. J. Mohr, B. N. Taylor, and D. B. Newell, *CODATA recommended values of the fundamental physical constants: 2006*, Reviews of Modern Physics **80**, 633 (2008).

[50] H. Abgrall and E. Roueff, *Theoretical calculations of excited rovibrational levels of HD. Term values and transition probabilities of VUV electronic bands*, Astronomy & Astrophysics **445**, 361 (2006).

[51] H. L. Bethlem, M. Kajita, B. Sartakov, G. Meijer, and W. Ubachs, *Prospects for precision measurements on ammonia molecules in a fountain*, European Physical Journal - Special Topics **163**, 55 (2008).

[52] H. L. Bethlem and W. Ubachs, *Testing the time-invariance of fundamental constants using microwave spectroscopy on cold diatomic radicals*, Faraday Discussions **142**, 25 (2009).

[53] J. K. Webb, V. V. Flambaum, C. W. Churchill, M. J. Drinkwater, and J. D. Barrow, *Search for time variation of the fine structure constant*, Physical Review Letters **82**, 884 (1999).

[54] X. Calmet and H. Fritzsch, *The cosmological evolution of the nucleon mass and the electroweak coupling constants*, European Physical Journal C **24**, 639 (2002).

[55] D. A. Varshalovich and S. A. Levshakov, *On a time-dependence of physical constants*, JETP Letters **58**, 237 (1993).

[56] J. Philip, J. P. Sprengers, T. Pielage, C. A. de Lange, W. Ubachs, and E. Reinhold, *Highly accurate transition frequencies in the H_2 Lyman and Werner absorption bands*, Canadian Journal of Chemistry **82**, 713 (2004).

[57] K. S. E. Eikema, W. Ubachs, W. Vassen, and W. Hogervorst, *Lamb shift measurement in the* $1\ ^1S$ *ground state of helium*, Physical Review A **55**, 1866 (1997).

[58] W. Ubachs, K. S. E. Eikema, W. Hogervorst, and P. C. Cacciani, *Narrow-band tunable extreme-ultraviolet laser source for lifetime measurements and precision spectroscopy*, Journal of the Optical Society of America B **14**, 2469 (1997).

[59] H. Abgrall, E. Roueff, F. Launay, J. Y. Roncin, and J. L. Subtil, *Table of the Lyman band system of molecular hydrogen*, Astronomy & Astrophysics Supplement Series **101**, 273 (1993).

[60] H. Abgrall, E. Roueff, F. Launay, J. Y. Roncin, and J. L. Subtil, *The Lyman and Werner band systems of molecular hydrogen*, Journal of Molecular Spectroscopy **157**, 512 (1993).

[61] D. E. Jennings, A. Weber, and J. W. Brault, *FTS-Raman Flame Spectroscopy of High-j Lines In H_2 and D_2*, Journal of Molecular Spectroscopy **126**, 19 (1987).

[62] E. E. Eyler, A. Yiannopoulou, S. Gangopadhyay, and N. Melikechi, *Chirp-free nanosecond laser amplifier for precision spectroscopy*, Optics Letters **22**, 49 (1997).

[63] H. Bredohl and G. Herzberg, *Lyman and Werner bands of deuterium*, Canadian Journal of Physics **51**, 867 (1973).

[64] I. Dabrowski and G. Herzberg, *The Absorption Spectrum of D_2 from 1100 to 840 Å*, Canadian Journal of Physics **52**, 1110 (1974).

[65] S. Takezawa and Y. Tanaka, *Absorption-spectrum of D_2 in vacuum-UV region, Rydberg bands, $np\sigma\,^1\Sigma_u^+ \leftarrow X\,^1\Sigma_g^+$ and $np\pi\,^1\Pi_u \leftarrow X\,^1\Sigma_g^+$ with n=4-6, and the ionization energy*, Journal of Molecular Spectroscopy **54**, 379 (1975).

[66] M. Larzilliere, F. Launay, and J. Y. Roncin, *High-resolution emission spectra of H_2 and D_2 near 80 nm*, Journal de Physique IV **41**, 1431 (1980).

[67] P. C. Hinnen, W. Hogervorst, S. Stolte, and W. Ubachs, *Sub-doppler Laser Spectroscopy of H_2 and D_2 in the range 91-98 nm*, Canadian Journal of Physics **72**, 1032 (1994).

[68] J. Y. Roncin and F. Launay, *Atlas of the vacuum-ultraviolet emission-spectrum of molecular hydrogen*, Journal of Physical and Chemical Reference Data pp. U1–& (1994).

[69] M. Roudjane, W.-U. L. Tchang-Brillet, and F. Launay, *High resolution vacuum ultraviolet emission spectrum of D_2: The $B'\,^1\Sigma_u^+ \rightarrow X\,^1\Sigma_g^+$ band system*, Journal of Chemical Physics **127**, 054307 (2007).

[70] S. C. Xu, R. van Dierendonck, W. Hogervorst, and W. Ubachs, *A dense grid of reference iodine lines for optical frequency calibration in the range 595-655 nm*, Journal of Molecular Spectroscopy **201**, 256 (2000).

[71] T. I. Ivanov, M. O. Vieitez, C. A. de Lange, and W. Ubachs, *Frequency calibration of $B\,^1\Sigma_u^+$ - $X\,^1\Sigma_g^+$ (6,0) Lyman transitions in H_2 for comparison with quasar data*, Journal of Physics B **41**, 035702 (2008).

[72] D. E. Jennings, A. Weber, and J. W. Brault, *Raman-spectroscopy of gases with a Fourier-transform spectrometer - the spectrum of D_2*, Applied Optics **25**, 284 (1986).

[73] N. Bohr, *On the constitution of atoms and molecules*, Philosophical Magazine **26**, 1 (1913).

[74] T. F. Gallagher, *Rydberg Atoms* (Cambridge University Press, Cambridge, UK, 1994).

[75] F. E. Maas et al., *A measurement of the 1S-2S transition frequency in muonium*, Physics Letters A **187**, 247 (1994).

[76] M. S. Fee, S. Chu, A. P. Mills, R. J. Chichester, D. M. Zuckermann, E. D. Shaw, and K. Danzmann, *Measurement of the positronium $1\,^3S_1$ – $2\,^3S_1$ interval by continuous-wave two-photon excitation*, Physical Review A **48**, 192 (1993).

[77] W. A. Chupka, P. M. Dehmer, and W. T. Jivery, *High resolution photoionization study of ion-pair formation in H_2, HD, and D_2*, Journal of Chemical Physics **63**, 3929 (1975).

[78] R. C. Shiell, X. K. Hu, Q. C. J. Hu, and J. W. Hepburn, *Threshold ion-pair production spectroscopy (TIPPS) of H_2 and D_2*, Faraday Discussions **115**, 331 (2000).

[79] E. Reinhold and W. Ubachs, *Observation of coherent wave packets in a heavy Rydberg system*, Physical Review Letters **88**, 013001 (2001).

[80] A. ten Wolde, L. D. Noordam, A. Lagendijk, and H. B. van Linden van den Heuvell, *Observation of radially localized atomic electron wave packets*, Physical Review Letters **61**, 2099 (1988).

[81] J. A. Yeazell, M. Mallalieu, J. Parker, and C. R. Stroud, *Classical periodic motion of atomic-electron wave packets*, Physical Review A **40**, 5040 (1989).

[82] E. Reinhold, A. de Lange, W. Hogervorst, and W. Ubachs, *Observation of the $I'\,^1\Pi_g$ outer well state in H_2 and D_2*, Journal of Chemical Physics **109**, 9772 (1998).

[83] P. C. Hinnen, W. Hogervorst, S. Stolte, and W. Ubachs, *Sub-Doppler laser spectroscopy of H_2 and D_2 in the range 91-98 nm*, Canadian Journal of Physics **72**, 1032 (1994).

[84] E. Reinhold and W. Ubachs, *Heavy Rydberg states*, Molecular Physics **103**, 1329 (2005).

[85] C. Jungen, U. Even, and M. S. Child, *Quantum defect theory of the dynamics of molecular Rydberg states*, Advances in Chemical Physics **101**, 701 (1997).

[86] A. Osterwalder, A. Wüst, F. Merkt, and C. Jungen, *High-resolution millimeter wave spectroscopy and multichannel quantum defect theory of the hyperfine structure in high Rydberg states of molecular hydrogen H_2*, Journal of Chemical Physics **121**, 11810 (2004).

[87] S. H. Pan and F. H. Mies, *Rydberg-like properties of rotational vibrational levels and dissociation continuum associated with alkali-halide charge-transfer states*, Journal of Chemical Physics **89**, 3096 (1988).

[88] E. Reinhold, W. Hogervorst, and W. Ubachs, *Observation of a highly excited long-lived valence state in H_2*, Physical Review Letters **78**, 2543 (1997).

[89] A. de Lange, W. Hogervorst, W. Ubachs, and L. Wolniewicz, *Double-well states of ungerade symmetry in H_2; first observation and ab initio calculation*, Physical Review Letters **86**, 2988 (2001).

[90] T. Detmer, P. Schmelcher, and L. S. Cederbaum, Ab initio *calculations with a nonspherical Gaussian basis set: Excited states of the hydrogen molecule*, Journal of Chemical Physics **109**, 9694 (1998).

[91] J. C. J. Koelemeij, A. de Lange, and W. Ubachs, *Search for outer-well states above the ionization potential in H_2*, Chemical Physics **287**, 349 (2003).

[92] C. Jungen and M. Raoult, *Spectroscopy in the ionisation continuum. Vibrational preionisation in H_2 calculated by multichannel quantum-defect theory*, Faraday Discussions of the Chemical Society **71**, 253 (1981).

[93] L. Venturelli et al., *Protonium production in ATHENA*, Nuclear Instruments and Methods in Physics Research Section B **261**, 40 (2007).

[94] D. W. Chandler and P. L. Houston, *Two-dimensional imaging of state-selected photodissociation products detected by multiphoton ionization*, Journal of Chemical Physics **87**, 1445 (1987).

[95] A. Eppink and D. Parker, *Velocity map imaging of ions and electrons using electroscatic lenses: Application in photoelectron and photofragment ion imaging of molecular oxygen*, Review of Scientific Instruments **68**, 3477 (1997).

[96] C. R. Gebhardt, T. P. Rakitzis, P. C. Samartzis, V. Ladopoulos, and T. N. Kitsopoulos, *Slice imaging: A new approach to ion imaging and velocity mapping*, Review of Scientific Instruments **72**, 3848 (2001).

[97] J. A. Davies, J. E. LeClaire, R. E. Continetti, and C. C. Hayden, *Femtosecond time-resolved photoelectron-photoion coincidence imaging studies of dissociation dynamics*, Journal of Chemical Physics **111**, 1 (1999).

[98] M. N. R. Ashfold et al., *Imaging the dynamics of gas phase reactions*, Physical Chemistry Chemical Physics **8**, 26 (2006).

[99] A. I. Chichinin, K. H. Gericke, S. Kauczok, and C. Maul, *Imaging chemical reactions-3D velocity mapping*, International Reviews In Physical Chemistry **28**, 607 (2009).

[100] M. L. Lipciuc, A. J. van den Brom, L. Dinu, and M. H. M. Janssen, *Slice imaging of photodissociation of spatially oriented molecules*, Review of Scientific Instruments **76**, 123103 (2005).

[101] V. Papadakis and T. N. Kitsopoulos, *Slice imaging and velocity mapping using a single field*, Review of Scientific Instruments **77**, 083101 (2006).

[102] G. A. Garcia, H. Soldi-Lose, and L. Nahon, *A versatile electron-ion coincidence spectrometer for photoelectron momentum imaging and threshold spectroscopy on mass selected ions using synchrotron radiation*, Review of Scientific Instruments **80**, 023102 (2009).

[103] T. I. Ivanov et al., *Fourier-transform spectroscopy of HD in the vacuum ultraviolet at* $\lambda = 87 - 112$ *nm*, Molecular Physics **108**, 771 (2010).

[104] M. Roudjane, T. I. Ivanov, M. O. Vieitez, C. A. de Lange, W. U. L. Tchang-Brillet, and W. Ubachs, *Extreme ultraviolet laser calibration of* D_2 *Lyman and Werner transitions*, Molecular Physics **106**, 1193 (2008).

[105] E. J. Salumbides, D. Bailly, A. Khramov, A. L. Wolf, K. S. E. Eikema, M. Vervloet, and W. Ubachs, *Improved laboratory values of the* H_2 *Lyman and Werner lines for constraining time variation of the proton-to-electron mass ratio*, Physical Review Letters **101**, 223001 (2008).

[106] J. P. Sprengers, W. Ubachs, K. G. H. Baldwin, B. R. Lewis, and W. U. L. Tchang-Brillet, *Extreme ultraviolet laser excitation of isotopic molecular nitrogen: The dipole-allowed spectrum of* $^{15}N_2$ *and* $^{14}N^{15}N$, Journal of Chemical Physics **119**, 3160 (2003).

[107] D. W. Neyer, A. J. R. Heck, and D. W. Chandler, *Photodissociation of* N_2O*: J-dependent anisotropy revealed in* N_2 *photofragment images*, Journal of Chemical Physics **110**, 3411 (1999).

[108] R. Zare and D. Hershbach, Proceedings IEEE **51**, 173 (1963).

[109] E. Wrede, E. R. Wouters, M. Beckert, R. N. Dixon, and M. N. R. Ashfold, *Quasiclassical and quantum mechanical modeling of the breakdown of the axial recoil approximation observed in the near threshold photolysis of IBr and Br_2*, Journal of Chemical Physics **116**, 6064 (2002).

[110] B. J. Whitaker, *Imaging in molecular dynamics* (Cambridge University Press, 2003).

[111] C. Jonah, *Effect of rotation and thermal velocity on anisotropy In photodissociation spectroscopy*, Journal of Chemical Physics **55**, 1915 (1971).

[112] P. Levelt, *A coherent XUV-source for high resolution spectroscopy: application to diatomic molecules*, Ph.D. thesis, Vrije Universiteit Amsterdam (1992).

[113] P. C. Hinnen, *XUV-laser spectroscopy of H_2 and the mystery of the diffuse interstellar bands*, Ph.D. thesis, Vrije Universiteit Amsterdam (1997).

[114] K. Eikema, *QED and the ground state of helium: precision extreme ultraviolet laser spectroscopy*, Ph.D. thesis, Vrije Universiteit Amsterdam (1996).

[115] S.-M. Wu, *Imaging the photodissociation dynamics of OCS, SH and O_2: a guide to experimental design and atomic polarization*, Ph.D. thesis, Radboud University (2007).

[116] D. Irimia, R. Kortekaas, and M. H. M. Janssen, *In situ characterization of a cold and short pulsed molecular beam by femtosecond ion imaging*, Physical Chemistry Chemical Physics **11**, 3958 (2009).

[117] B. Y. Chang, R. C. Hoetzlein, J. A. Mueller, J. D. Geiser, and P. L. Houston, *Improved two-dimensional product imaging: The real-time ion-counting method*, Review of Scientific Instruments **69**, 1665 (1998).

[118] L. Wolniewicz and K. Dressler, *Adiabatic potential curves and nonadiabatic coupling functions for the first five excited $^1\Sigma_g^+$ states of the hydrogen molecule*, Journal of Chemical Physics **100**, 444 (1994).

[119] L. Wolniewicz, *Adiabatic potentials of the lowest $^1\Pi_g$ and $^{1,3}\Delta_g$ states of the hydrogen molecule*, Journal of Molecular Spectroscopy **169**, 329 (1995).

[120] L. Wolniewicz, *Lowest $^{1,3}\Delta_g$ states of the hydrogen molecule, II*, Journal of Molecular Spectroscopy **174**, 132 (1995).

[121] S. Werner, *Hydrogen bands in the ultra-violet Lyman region*, Proceedings of the Royal Society of London Series A **113**, 107 (1926).

[122] E. R. Davidson, *First excited $^1\Sigma_g^+$ state of the hydrogen molecule*, Journal of Chemical Physics **35**, 1189 (1961).

[123] P. Senn, P. Quadrelli, K. Dressler, and G. Herzberg, *Spectroscopic identification of the lowest rotation-vibration levels of the $(2p\sigma)^2$ $F\,^1\Sigma_g^+$ state of the H_2 molecule*, Journal of Chemical Physics **83**, 962 (1985).

[124] P. Senn and K. Dressler, *Spectroscopic identification of rovibronic levels lying above the potential barrier of the EF $^1\Sigma_g^+$ double-minimum state of the H_2 molecule*, Journal of Chemical Physics **87**, 6908 (1987).

[125] C. Jungen, I. Dabrowski, G. Herzberg, and M. Vervloet, *High orbital angular momentum states in H_2 and D_2. III. Singlet-triplet splittings, energy levels, and ionization potentials*, Journal of Chemical Physics **93**, 2289 (1990).

[126] L. Wolniewicz and K. Dressler, *EF and GK $^1\Sigma_g^+$ states of hydrogen - Adiabatic calculation of vibronic states in H_2, HD, and D_2*, Journal of Molecular Spectroscopy **67**, 416 (1977).

[127] P. Quadrelli, K. Dressler, and L. Wolniewicz, *Nonadiabatic coupling between the EF + GK + H $^1\Sigma_g^+$, I $^1\Pi_g$, and J $^1\Delta_g$ states of the hydrogen molecule. Calculation of rovibronic structures in H_2, HD, and D_2*, Journal of Chemical Physics **92**, 7461 (1990).

[128] E. E. Marinero, C. T. Rettner, and R. N. Zare, *Quantum-state-specific detection of molecular hydrogen by three-photon ionization*, Physical Review Letters **48**, 1323 (1982).

[129] E. E. Marinero, R. Vadusev, and R. N. Zare, *The E,F $^1\Sigma_g^+$ double-minimum state of hydrogen: Two-photon excitation of inner and outer wells*, Journal of Chemical Physics **78**, 692 (1983).

[130] K. Tsukiyama, J. Ishii, and T. Kasuya, *Fluorescence lifetimes of EF $^1\Sigma_g^+$, GK $^1\Sigma_g^+$, H $^1\Sigma_g^+$, I $^1\Pi_g$, and J $^1\Pi_g$ states of H_2 studied by extreme ultraviolet visible double-resonance excitation*, Journal of Chemical Physics **97**, 875 (1992).

[131] K. Tsukiyama, S. Shimizu, and T. Kasuya, *Identification of the EF $^1\Sigma_g^+$ ($v' = 31$ and 32) states of H_2 by XUV-VIS double-resonance spectroscopy*, Journal of Molecular Spectroscopy **155**, 352 (1992).

[132] J. Ishii, K. Ttukiyama, and K. Uehara, *Identification of excited gerade states of molecular hydrogen with extreme ultraviolet-visible double-resonance excitation technique*, Laser Chemistry **14**, 31 (1994).

[133] A. de Lange, E. Reinhold, and W. Ubachs, *Spectroscopy on some g symmetry states in H_2 and determination of the ionization potential*, Physical Review A **65**, 064501 (2002).

[134] D. Bailly, E. J. Salumbides, M. Vervloet, and W. Ubachs, *Accurate level energies in the EF* $^1\Sigma_g^+$*, GK* $^1\Sigma_g^+$*, H* $^1\Sigma_g^+$*, B* $^1\Sigma_u^+$*, C* $^1\Pi_u$*, B'* $^1\Sigma_u^+$*, D* $^1\Pi_u$*, I* $^1\Pi_g$*, J* $^1\Delta_g$ *states of* H_2, Molecular Physics **108**, 827 (2010).

[135] S. Yu and K. Dressler, *Calculation of rovibronic structures in the lowest nine excited* $^1\Sigma_g^+ + {}^1\Pi_g + {}^1\Delta_g$ *- states of* H_2*,* D_2*, and* T_2, Journal of Chemical Physics **101**, 7692 (1994).

[136] L. Wolniewicz, *Relativistic corrections to the energies of the EF, GK, and* $H\bar{H}$ $^1\Sigma_g$ *states of the hydrogen molecule*, Journal of Chemical Physics **109**, 2254 (1998).

[137] C. R. Scheper, C. A. de Lange, A. de Lange, E. Reinhold, and W. Ubachs, *Dissociation of* H_2 *in the energy region at the H(n=1)+H(n=3) dissociation threshold after (1+1') resonance-enhanced two-photon ionization via the B* $^1\Sigma_u^+$ *state*, Chemical Physics Letters **312**, 131 (1999).

[138] C. R. Scheper, W. J. Buma, C. A. de Lange, and W. J. van der Zande, *Photoionization and photodissociation dynamics of* H_2 *after (3+1) resonance-enhanced multiphoton ionization via the B* $^1\Sigma_u^+$ *state*, Journal of Chemical Physics **109**, 8319 (1998).

[139] J. T. Hougen, *Classification of rotational energy levels for symmetric-top molecules*, Journal of Chemical Physics **37**, 1433 (1962).

[140] J. T. Hougen, *Classification of rotational energy levels. II*, Journal of Chemical Physics **39**, 358 (1963).

[141] J. T. Hougen, *Calculation of rotational energy levels and rotational line intensities In diatomic molecules*, National Bureau of Standards Monographs pp. 1–& (1970).

[142] P. F. Bernath, *Spectra of atoms and molecules* (Oxford University Press, 1995).

Acknowledgments

Now my thesis is at its end I would like to seize the opportunity to thank all the people, which helped and supported me throughout my period as a PhD student.

First of all I am very grateful to my promotors Wim Ubachs and Kees de Lange who have given me the opportunity to join the ALF group and have guided me with care and patience throughout my PhD. I admire both of you for your relaxed, but pragmatic attitude towards science, turning stressful moments into pleasant periods of time. Your prompt and lightning fast paper reviews made it possible to set a record in the group for fastest prepared and accepted article. Wim, you have given me both the freedom and gentle guidance I needed to perform the experiments. I admire your ability to always find time to drop in the lab once a day despite your dense agenda. Your valuable comments and useful ideas were always appreciated. Kees, you were always easily approachable with any scientific questions giving remarkably clear and detailed answers. I appreciate your encouragement and indispensible support in writing drafts and improving my Slavic English. I consider myself most fortunated to have had such nice promotors.

Elmar Reinhold, my first teacher in the lab who gave me a deep introduction to the XUV system. Actually, many of the results presented in this thesis are a consequence of your initial measurements. I really appreciate your willingness to share your detailed knowledge on the hydrogen molecule and quantum mechanics in general.

I enjoyed my time at the VU a lot and the people "to blame" are all my collegues from the Atomic, Molecular and Laser Physics Group. Thank you guys for maintaining such a creative, yet enjoyable athmosphere, with people around always willing to help, advise or just show the most hilarious videos on YouTube. My sincere gratitude to the people that were closer to my side of the lab. Ofelia, who came almost at the same time I joined the group and brought this bright south american spirit in the gloomy lab. Apart from the numerous papers, evidence for a strong and productive collaboration, working with you was also extremely enjoyable. It was real fun to exchange musical masterpieces (like the lion king song, musica boluda and others) in the morning, and then enjoy each others whistling during the whole day. I believe we made a good

team and also hope to keep in touch for years to come. Edcel, always open for brainstorming in all kinds of topics, not only scientific. Dude, it is always fun having you around exhanging important and unimportant information and competing to see who can reach the highest level on Baloon Tower Defense. I wish you good luck with the challenging plans you have in Cebu. Sandro, the other dude who together with Edcel have drawn me to the "dark side" of Gentoo. I can say I feel now that the dark side is much stronger! Lineke can emerge at any time from somewhere with that familiar "Did I tell you this funny story?", after which the fun is guaranteed. Gareth, my successor on the XUV experiment is the most healthy eating Liverpool fan that I happen to know, always open for all kinds of stupid pranks. In the end I will try to rephrase a famous quote... All these people really tied the Lab together.

Kjeld, thank you for giving me the opportunity to start this interesting project, which I am looking forward to lead to a successful end.

Every experimentalist knows the feeling of missing that one piece needed to complete an experiment, the struggle and frustration trying to find or make it. My gratitude to Jacques, our technician who always comes up with fast and remarkably simple solutions to our problems in the lab. His effort to maintain this well organized lab and standartirize the available equipment is crucial for the smooth experimental work.

Thanks to the other members of the group who brought their bright spirit at the coffee breaks and maintained the nice working atmosphere in the Laser center: Adrian, Alex, Ali, Amandine, Anne Lisa, Arjan, Arno, Christoph, Daniel I, Daniel J, Daniel N, Dmitry, Dominik, Dong Feng, Erik-Jan, Itan, Jeroen, Joe, John, Jonas, Marina, Martijn, Paul, Rick, Rob, Roel R., Roel Z., Ruth, Ruud, Stephan, Tjeerd (thanks for the tranlation of my summary in Dutch), Tom, Valdas, Wim R., Wim V and more. Working with you was extemely enjoyable.

I am greatful to our secretary Marja Herronen who is always very helpful at solving all kinds of bureaucracy issues.

During my PhD I was involved in several collaboration projects with French groups. I would like to thank the crew of the DESIRS beamline of SOLEIL synchrotron facility and the people from Observatoire de Paris-Meudon - Nelson de Oliveira, Mourad Roudjane, Denis Joyeux, Michel Vervloet, Lydia Tchang-Brillet, Laurent Nahon and the others. Thank you for your kind hospitality and for the productive and pleasant time I enjoyed on french soil.

Life is not only work. I am very lucky that few of my best friends from university time are still close. Special thanks to my bulgarian friends - Dimitar, Vania, Alis, Radi, Denitza, Milena who make the time outside of work relaxing and real fun. Living abroad would be much more difficult without you guys.

I will always be greatful to my first Physics teacher Theodosii Theodosiev, who showed me the exciting side of science. Your teachings, not only in science have had a great influence on my life. On behalf of all your students i would

like to thank you for your efforts and dedication you have put into educating us.

And at last but not least I would like to thank my family for their love and support. Special thanks to my significant other Beata who had the patience to endure the acomplishment of this thesis, but who was extremely supportive and encouraging. Now that this thesis is complete I will make up for the time I spent away from you, whilst writing my thesis.

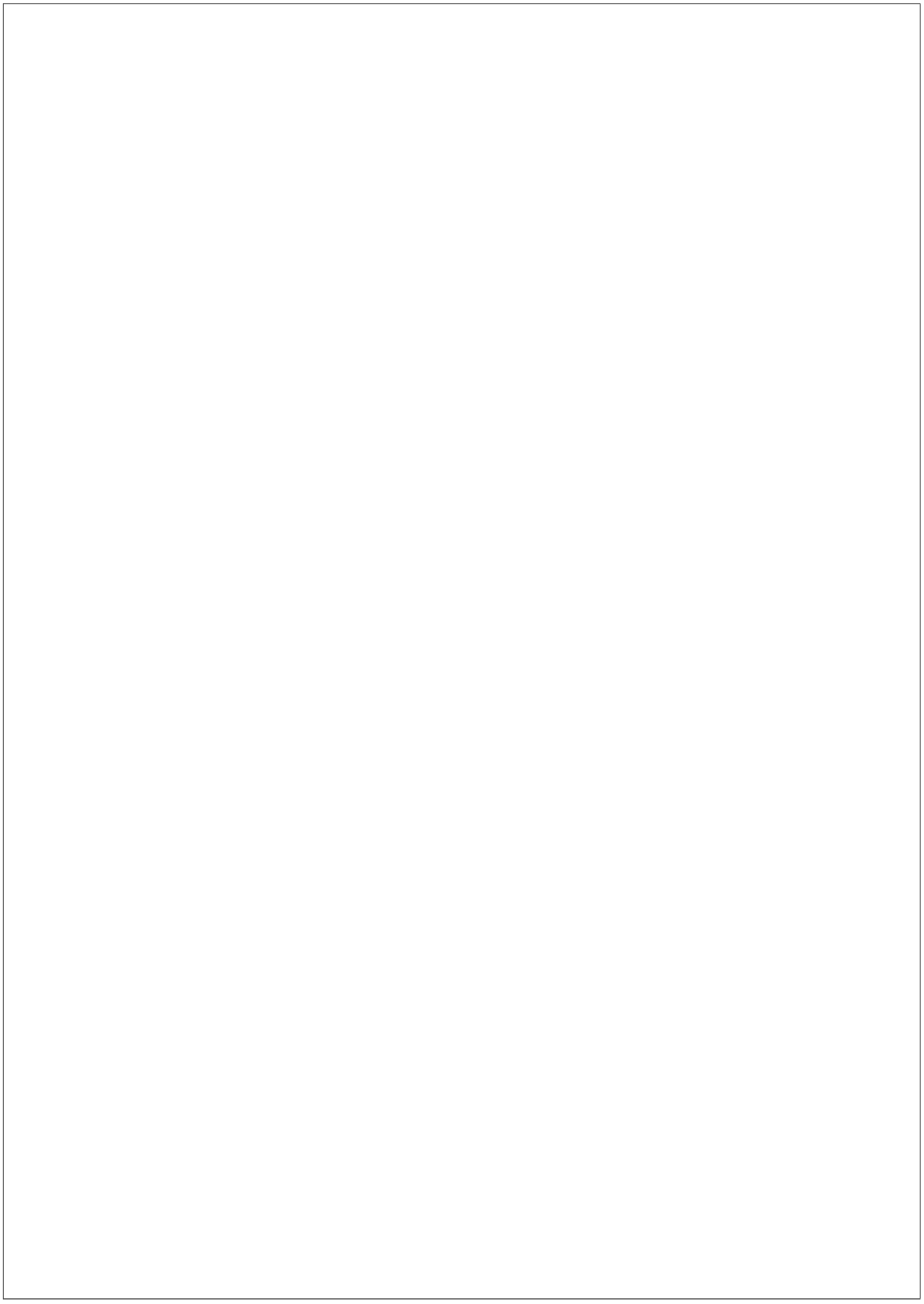

List of publication

Included in this thesis:

T.I. Ivanov, M. Roudjane, M.O. Vieitez, C.A. de Lange, W.U.L. Tchang-Brillet and W. Ubachs, *HD as a Probe for Detecting Mass Variation on a Cosmological Time Scale* Phys. Rev. Lett. 100, 093007 (2008) (Chapter 2)

T.I. Ivanov, G.D. Dickenson, M. Roudjane, N. de Oliveira, D. Joyeux, L. Nahon, W.U.L. Tchang-Brillet, W. Ubachs, *Fourier-transform spectroscopy of HD in the vacuum ultraviolet at lambda = 87-112 nm* Mol. Phys. 108, 771-786 (2010) (Chapter 3)

T.I. Ivanov, M.O. Vieitez, C.A. de Lange and W. Ubachs, *Frequency calibration of* $B\,^1\Sigma_u^+ - X\,^1\Sigma_g^+$ *(6,0) Lyman lines in* H_2 *for comparison with quasar data*, J. Phys. B 41, 035702 (2007) (Chapter 4)

M. Roudjane, T.I. Ivanov, M.O. Vieitez, C.A. de Lange, W.U.L. Tchang-Brillet and W. Ubachs, *Extreme ultraviolet laser calibration of* D_2 *Lyman and Werner transitions* Mol. Phys. 106, 1193-1197 (2008) (Chapter 5)

M. O. Vieitez, T. I. Ivanov, E. Reinhold, C. A. de Lange and W. Ubachs, *Observation of a Rydberg series in a heavy Bohr atom*, Phys. Rev. Lett. 101, 163001 (2008) (Chapter 6).

Additional publications:

M.O. Vieitez, T.I. Ivanov, J.P. Sprengers, C.A. de Lange, W. Ubachs, B.R. Lewis and G. Stark, *Quantum-interference effects in the* $o\,^1\Pi_u(v=1) - b\,^1\Pi_u(v=9)$ *Rydberg-valence complex of molecular nitrogen*, Mol. Phys. 105, 1543-1557 (2007)

M.O. Vieitez, T.I. Ivanov, W. Ubachs, B.R. Lewis and C.A. de Lange, *On the complexity of the absorption spectrum of molecular nitrogen*, J. Molecular Liquids 141, 110-117 (2008)

M.O. Vieitez, T.I. Ivanov, C.A. de Lange, W. Ubachs, A.N. Heays, B.R. Lewis and G. Stark, *Interactions of the* $3p\pi_u c\,^1\Pi_u(v=2)$ *Rydberg-complex member in isotopic* N_2, Mol. Phys. 105, 1543-1557 (2008)

T.I. Ivanov, E.J. Salumbides, M.O. Vieitez, P.C. Cacciani, C.A. de Lange and W. Ubachs, *Extreme ultraviolet laser metrology of O I transitions* Monthly Notices Roy. Astron. Society Letters 389, L4-L7 (2008).

M.O. Vieitez, T.I. Ivanov, E.Reinhold, C.A. de Lange, W. Ubachs, *Spectroscopic observation and characterization of H+H- heavy Rydberg states* J. Phys. Chem. A 113, 13237-13245 (2009)

G. Dickenson, T. Ivanov, M. Roudjane, N. de Oliveira, D. Joyeux, L. Nahon, L. Tchang-Brillet, M. Glass-Maujean, I. Haas, A. Ehresmann, W. Ubachs *Synchrotron VUV radiation studies of the* $D^1\Pi_u$ *state of* H_2 J. Chem. Phys. 133, 144317 (2010)